DYNAMIC MODELING OF METHANOL SYNTHESIS FROM ELECTROLYTIC HYDROGEN AND CAPTURED CARBON DIOXIDE

ABSTRACT

Dynamic modelling of methanol synthesis from electrolytic hydrogen and captured carbon dioxide

Power-to-methanol, in which methanol can be produced from captured CO_2 and electrolytic H_2, can be seen as a promising solution for CO_2 emission reduction leading to diminish global warming. However, the fluctuation in the amount of H_2 generated from renewable electricity via water electrolysis leads (1) to expensive, high-pressure storage requirement, which is not suitable for long-term storage and industrial scaling up, and (2) to a variable methanol production integrating with power and H_2 generation. Therefore, building a dynamic model for methanol production plays a crucial role to understand the dynamic characteristics of the process at various feed stream disturbances, consequently resulting in the development of a robust control structure for methanol synthesis.

This thesis is a part of the Business Finland funded HYGCELL project. The results in this thesis are compared to other Power-to-hydrogen-to-products processes in dynamic environment to figure out the most feasible value chain and its development potential. In this thesis, a dynamic model of crude methanol synthesis through CO_2 hydrogenation was built

to assess the stability of control structures and the efficiencies of the process during feed stream disturbances. To be specific, a dynamic model in Aspen plus dynamics was built based on a steady-state model in Aspen plus (corresponding to ~25,000 tons MeOH/year) with the input data from publications. The investigation in terms of energy efficiency and dynamic characteristics during load changes was carried out.

The results pointed out that the flow rate of the outputs (crude methanol and purging gases) and heat duties of the heat exchangers, can follow up and agree with the changes in H_2 feed rate. During loading changes, components composition at the reactor inlet fluctuates insignificantly, and the energy efficiency slightly drops from ~88.5 % to 86.75 % with the ramping rate of 50 %/ hour. The minimum loading based on Aspen plus dynamics is 18.8 % of the maximum capacity. However, for feasible operation of heat exchanger (reactor preheater), the process should be operated at over 24.6 % loading levels. The highest ramping rate that the model can handle is 50 % changes (decrease and increase) per 0.117 hours. A part of real-time electrolytic H_2 data based on solar electricity in the range between 91 kmol/h (~31.1 % loading) and 292.5 kmol/h (full-load mode) within three hours was implemented and the validity of the model still remained in continuously fluctuating of H_2 feeding condition.

ACKNOWLEDGEMENTS

Viet Hung Nguyen

December 2022

Lappeenranta, Finland.

Table of contents

Abstract

Acknowledgements

Table of contents

Appendices

Appendix 1. Equipment sizing

Appendix 2. Matlab code

Appendix 3. Streams tables

ABBREVIATIONS

AEL	Alkaline electrolysis
C1	One carbon
CAES	Pressed-air energy storage
CHP	Combined heat and power
COP21	The 21st session of the Conference of the Parties
CRD	Crude methanol
CSP	Concentrating solar power
DME	Dimethyl ether
DSM	Demand-side management
E85	Fuel of gasoline with 85% ethanol
EESs	Energy storage systems
EU28	European countries with 28 members
FBR	Fixed-bed reactor
FCR	Reflux flow control
FFVs	Flexible fuel vehicles
FT	Fischer-Tropsch
GEM	Fuel mixture of gasoline, ethanol, and methanol
GHG	Greenhouse gases
GHSV	Gas hourly space velocity
IEA	International energy agency
IRENA	International Renewable Energy Agency
KPIs	Key performance indicators
LC	Load change
LCOMeOH	Levelized cost of methanol
M5/85/100	Fuel of gasoline with 5%/ 85%/ 100 % methanol
MeOH	Methanol
MPC	Model predictive controller
MTBE	Methyl tert-butyl ether
MTG/ MTO	Methanol to olefins/ Methanol to gasoline
NREL	National Renewable Energy Laboratory
OP	Controller output

P2M	Power-to-methanol
PEM	Polymer electrolyte membrane electrolysis
PFR	Plug flow reactor
PHS	Pumped hydro storage
PID	Proportional-integral-derivative
PtG	Power-to-gas
PtL	Power-to-liquid
PtX	Power-to-X
PV	Measured variable/ Process variable
R	Ramping rate
RADFRAC	Multi-stage separation model
R/F	Reflux/feed ratio
RES	Renewable energy sources
RFB	Redox Flow Battery
SDG	Sustainable development goals
SEMS	Superconducting Magnetic Energy Storage
SN	Stoichiometry number
SNG	Synthesis natural gas
SOEC	Solid oxide electrolysis
SP	Set point
SRC	Steam raising converter
SRK	Soave-Redlich-Kwong
SSM	Supply-side management
STY	Space-time yield
ZSM-5	Zeolite catalyst

SYMBOLS

a	Maximum amplitude of measured variable signal	%
d	Height of relay (percentage of controller output scale)	%
D_g	Diameter based on maximum vapor velocity	m
D_l	Diameter based on volumetric flow rate of liquid	m
$e(t)$	Function of error over time	-
E_{steam}	Power of released heat from methanol synthesis reactor	MJ h^{-1}
f_L^{RE}	Renewable penetration	-
f_r	Recycle ratio	-
h_{max}	Maximum liquid level	%
h_{min}	Minimum liquid level	%
K_C	Controller gain	-
K_{CU}	Ultimate gain of controller	-
LHV_i	Lower heating value of gases	MJ h^{-1}
$\dot{m}$	Mass flow rate of streams	kg h^{-1}
η	Energy efficiency	%
ϕ_{min}	Minimum loading of methanol synthesis reactor	%
$\bar{p}$	Steady-state value	-
p_{CO}	Partial pressure of CO	bar
p_{CO2}	Partial pressure of CO_2	bar
p_{H2}	Partial pressure of H_2	bar
p_{H2O}	Partial pressure of water	bar
p_{MeOH}	Partial pressure of methanol	bar
ppm	Part per million	ppm
$p(t)$	Output of controller	-
ρ_V	Vapor density	kg m^{-3}
P	Gain parameter	%/%
Pi	Power input for compressors	MJ h^{-1}
P_U	Ultimate period	%/%
Q_{max}	Maximum flow rate through control valve	m^3 min^{-1}
r_{CO}	Reaction rate of water gas-shift reaction	kmol kgcat^{-1} s^{-1}
r_{MeOH}	Reaction rate of CO_2 hydrogenation	kmol kgcat^{-1} s^{-1}

t	Time-on-stream	h
τ_D	Derivative time	min
τ_I	Integral time	min
V	Volume of tank	m^3
V_g	Volumetric flow rate of vapor	$m^3\,h^{-1}$
V_l	Volumetric flow rate of liquid	$m^3\,h^{-1}$
V_R	Volume of catalyst bed	m^3
$\dot{V}_{fg}$	Volumetric flow of feed stream to reactor	$m^3\,h^{-1}$
$\dot{V}_{fg,in}$	Volumetric flow in standard conditions	$m^3\,h^{-1}$
V_{max}	Maximum vapor velocity	$m^3\,s^{-1}$
$\dot{V}_{rg}$	Volumetric flow of recycled stream to reactor	$m^3\,h^{-1}$

LITERATURE PART

1 Introduction

The emission of carbon dioxide (CO_2) and greenhouse gases (GHG) is considered as the main reason behind global warming. As shown in Figure 1, it is obvious that the concentration of CO_2 in atmosphere has exponentially increased since the first years of the industrial revolution and reached over 400 ppm [1]. This has raised a serious concern in recent decades and led to the application of the Paris COP21 agreement in terms of CO_2 emissions reduction with the objectives: the threshold of global temperature increase below 2 °C, preferably 1.5 °C, compared to the pre-industrial period and achieve the peak of GHG emissions as soon as possible [2].
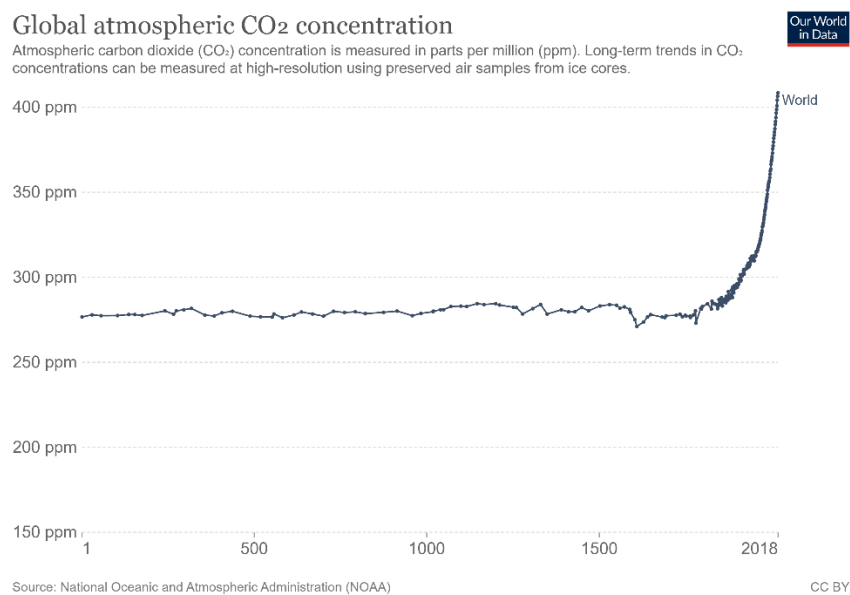
Figure 1. The global average concentration of CO_2 in the atmosphere [1].

According to the data from Figure 2, electricity and heat production is the main sector for CO_2 emissions corresponding to over 14,000 tons of CO_2 emitted in 2019 [3], and the increase of global population as well as the fast technological development raise an alarm for the increasing electricity demand. It is expected that global electricity consumption

would be doubled from 25,000 TWh in the next 30 years [4]. In fact, there have been lots of efforts made in electricity production to limit its negative effect on the environment; among many methods, electricity generation from renewable energy sources (RES) including waterpower, wind energy, solar power, biomass, and geothermal energy, has been widely applied and showed positive results, promising the possibility for the replacement of fossil fuel-based electricity. It is forecasted that electricity from RES would account for over 65 % of the electricity generation by 2040 and the share could reach 100% technically and economically in EU and USA by 2050 [5].
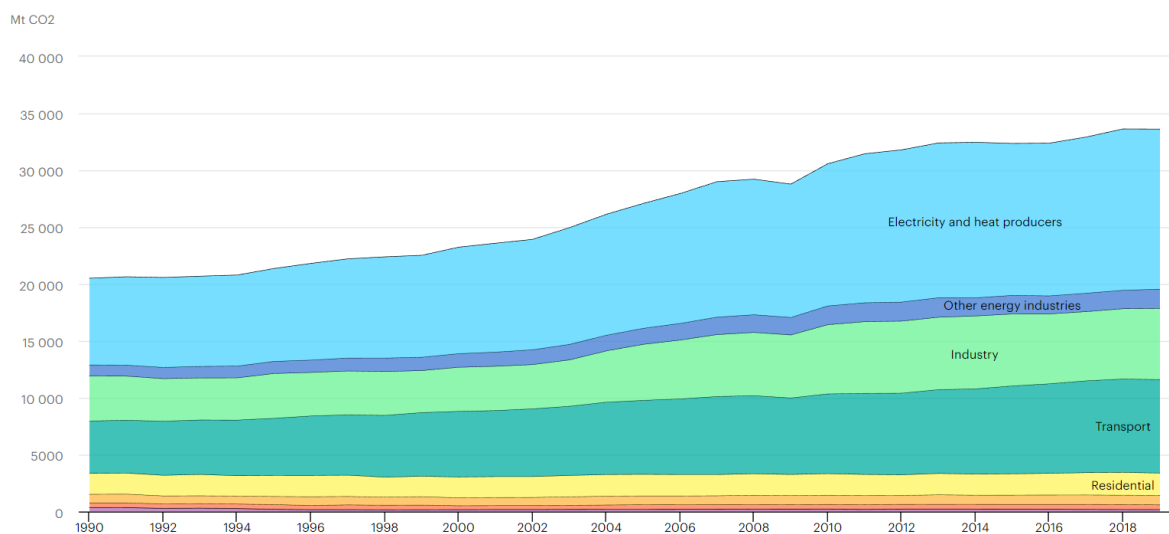
Figure 2. CO_2 emissions by different sectors, world 1990-2019 [3].

However, the fluctuation of these energy sources, which can cause the temporary excess or inadequacy of electricity leading to the instability of the grid, is one of the obstacles preventing the wide penetration of RES-based electricity. This is the driver in finding and developing energy storage technologies to balance the supply and demand in the electricity network. According to European Union (EU28) [6], around 30 % of electricity from RES could be balanced by the network; this value is up to 80 % when short-term energy storage such as thermal storage, smart charging, and vehicle-to-grid are applied. The further penetration increase requires long-term energy storage including the chemical synthesis from excess electricity to valuable fuels, which is defined as Power-to-X (PtX) [7].

1.1 Potential and challenges for Power-to-X

The first PtX concept was published by Koji Hashimoto to produce methane in 1994 [8]; since then, this concept has caught more attention from researchers, and many concepts with various X have been suggested and developed such as fuels, chemical platforms, heat, or power. In a typical PtX system, surplus electricity is applied to the water electrolysis process for H_2 generation, subsequently, this electrolytic H_2 is combined with the CO_2 directly captured from the air or from exhaust gas systems to produce valuable fuels (except in the case of ammonia, in which N_2 is used instead of CO_2) [5,9]. In fact, H_2 is a potential energy carrier and can be seen as a long-term energy storage approach due to its versatility, and transportable characteristic. Most importantly, H_2 has the highest gravimetric energy density but the lowest volumetric energy density compared to other fuels [5,9]. H_2 can be used as a fuel for a plant, in which H_2 will react to O_2 from ambient air in a fuel cell of the heater to generate electricity and heat [10]; or H_2 can be further converted into synthetic fuels such as methane, methanol, dimethyl ether, urea, and formic acid, etc [7,11].

Besides the many advantages above, most PtX concepts have a high green premium, which means that the production cost of "X" via PtX processes is still higher than that of the conventional processes from fossil fuels [12]. This comes from the fact that most PtX plants are on small scale, meanwhile conventional plants were already scaled up and operated on industrial scale, which can increase the economic advantages from the scale as well as decrease product pricing [13]. Moreover, most PtX models require high capital costs and large electricity demand; therefore, the lower price and the availability of excess renewable electricity, the higher chance of scaling up and commercialization of PtX models.

In fact, this thesis is part of the HYGCEL project funded by Business Finland with the aim to figure out the optimal power-to-X concept for Finland starting from electrolytic H_2. Among many potential candidates, power-to-methanol was chosen to be assessed in this thesis.

1.2 Methanol – an important chemical platform

Among many PtX concepts, Power-to-methanol (P2M) is a crucial route due to the importance of methanol in the fuel industry and chemical industry. To be specific, methanol is a flexible fuel and can be used in combustion engines mixed with gasoline in suitable ratios due to its high octane number (even higher than that of gasoline). In addition, methanol has lower toxicity compared to fossil fuels and less damage to the environment with the infinite miscibility in water as well as highly biodegradable [14,15].

However, additional safety measures for methanol usage and storage need to be carefully considered due to its toxicity (direct digestion and inhalation can cause serious damage to the human body) and specified properties such as easy flammability – the flash point below 23 ℃, relative high vapor pressure – 3 bar at 50 ℃, low boiling point – 65 ℃ at 1 bar, explosion limit – the lower limit at 6 vol% of MeOH and the upper limit at 36 vol% of MeOH in ambient conditions [16].

In terms of fuel application, according to Europe fuel quality standards, maximum of 3 % methanol can be blended in gasoline since 2009 [17]. In China, methanol can be mixed with gasoline in various blends ranging from 5 % (M5) to 100 % (M100) of methanol and flexible fuel vehicles (FFVs) can run on high-concentration methanol blends such as M85 or M100 [17,18]. In several markets, the mixture between gasoline, ethanol, and methanol (GEM) is also considered. Turner et al. [19] pointed out that GEM blends such as 29.5 % gasoline, 42.5 % ethanol, 28 % methanol or 37 % gasoline, 21 % ethanol, 42 % methanol, have somehow as similar performance as that of E85 (85 % ethanol and 15 % gasoline).

Besides applications in the fuel sector, methanol is seen as a C1 building block in the chemical industry. The various applications of methanol in this sector are clearly illustrated in Figure 3.
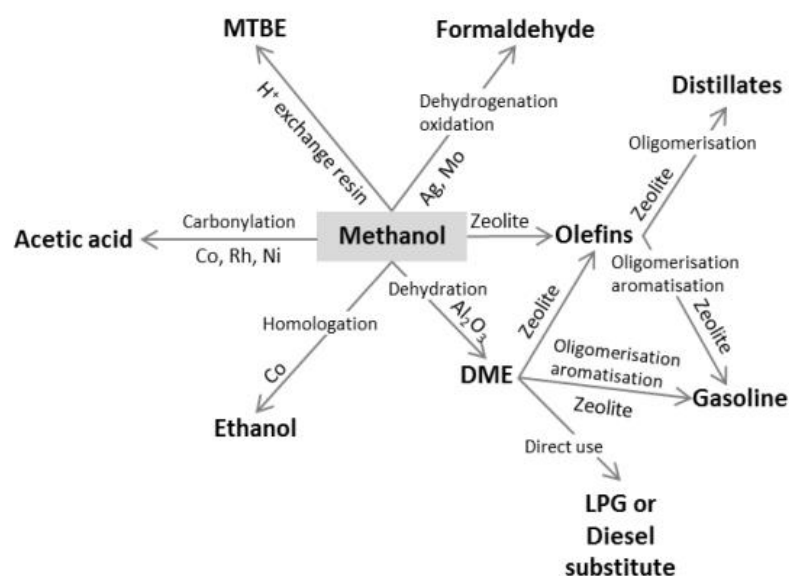
Figure 3. Several key derivatives from methanol [20].

Around one-fifth of methanol is supplied for formaldehyde production, followed by approximately 10 % for methyl tert-butyl ether (MTBE) [21]. This ether used to play a crucial role as a fuel additive with favourable characteristics in terms of octane number booster [22]. Methanol can also replace conventional petrochemical feedstock and processes to produce gasoline and olefins via the MTG and MTO routes, respectively [22].

Gasoline including paraffins, olefins, and aromatics with an acceptable amount of benzene can be synthesized via the MTG process. To be specific, an equilibrium mixture of dimethyl ether, methanol, and water is generated by the methanol dehydration process. Subsequently, the equilibrium mixture is transformed into light olefins before converting to gasoline with the presence of a zeolite catalyst such as ZSM-5 [23,24]. However, the non-selective generation of hydrocarbons coupled with the catalyst's deactivation is the main challenge of the MTG process [23]. MTO technology is a "shorter" process based on the MTG process. To be specific, instead of going via the full mechanism in the MTG model, MTO would finish at the formation of light olefins by catalyst and reaction conditions modifications [25,26]. Both processes have been commercialized at a large scale in China [23,25].

Aside from the use of methanol as a feedstock for other products, it is widely used as a solvent in organic industries or co-solvent in any fuel composition [27]. Additionally, since there is a growing trend of application of syngas from renewable sources, methanol is widely

applied for syngas cleaning during its operation. To be specific, the cleaning process is known as the "Rectisol process", in which refrigerated methanol is used as a physical solvent in an absorption tower to remove impurities of syngas such as H_2S [28].

2 Renewable power

As mentioned in the previous chapter, the increase in GHG emissions, consequently leading to global climate change and energy security has raised increasing attention to renewable energy sources (RES). According to IEA and OurWorldinData's data [29,30], electricity generation mainly comes from coal and natural gas, however, the percentage of these sources would decrease corresponding to the rapid increase of renewable electricity. In the last decade, the world net electricity share from renewables raised from 21 % to around 28 %, and in the next 30 years, electricity generated from RES would rise by nearly 10 % per decade, which is faster than the increase from any kind of other sources [29]. An increase by 16000 TWh (Terawatt hour) of renewable-based electricity by 2050 would be expected from around 6900 TWh in 2020 [29-31].

Table 1 illustrates the quantity of electricity generation from different RES in 2020 and 2050. In 2020, electricity from hydropower has the largest share with over 50 % of the quantity of RES-based electricity; meanwhile, the share of wind and solar energy is ~25 % and ~12 %, respectively [29,30]. However, in the next 30 years, electricity from solar and wind would dominate the share with over 70 %, in which solar energy is expected to be the largest source of electricity generation at ~40 %. To make the estimate come true, the design and development of long-term energy storage with scale-flexible and operation-flexible characteristics are required for the wide distribution of intermittent wind and solar power.

Table 1. World net electricity generation from RES [29-31].

Renewable energy sources	Electricity generation in 2020		Estimated electricity generation in 2050	
	Quantity (TWh)	Percentage (%)	Quantity (TWh)	Percentage (%)
Hydroelectric	4030	57.7	5210	23.6
Wind	1740	24.9	5530	29.1
Solar	830	11.9	6390	43.2
Geothermal	90	1.3	240	1.2
Other	290	4.2	560	2.9
Total	6980	100	17930	100

Based on OurWorldinData's data [30], generated electricity in Finland comes from fossil fuels (coal, oil, and gas), nuclear power, and renewable energies (hydropower, wind energy, solar energy, and other renewable energies mainly including bioenergy). As shown in Figure 4, there is a decrease in fossil fuels-based electricity from 50 % in 2003 to nearly 15 % in 2021; meanwhile, an upward trend is witnessed in the case of renewable electricity and this value reached over 50 % in 2021. The share of nuclear electricity is in the vicinity of 30 % over the past two decades.
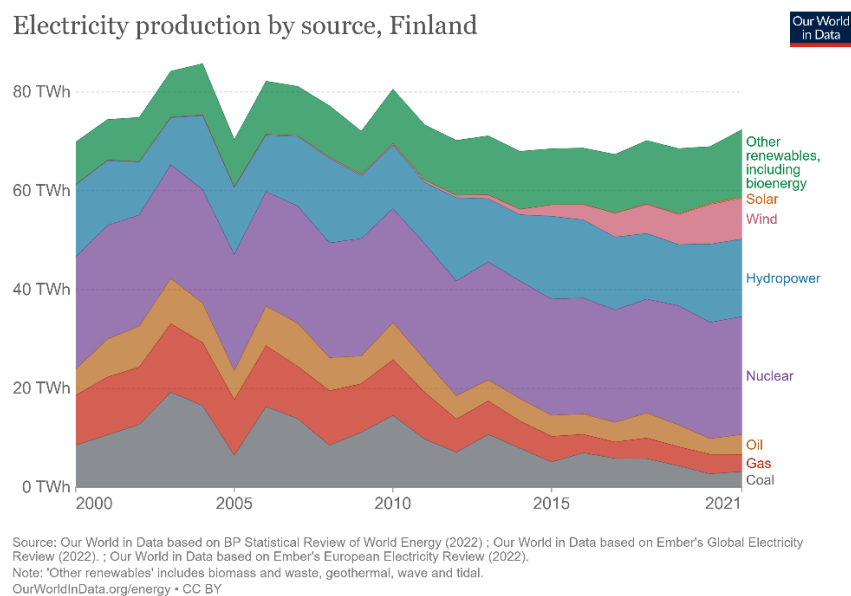

Figure 4. Generated electricity from different sources in Finland 2000 – 2021 [30].

More details about generated electricity from different type of renewable energies in Finland is shown in Table 2. The main share of RES electricity comes from hydropower and bio

energies (over 90 % from solid biomass [32]) (around 50 % and 49 % respectively in 2003); however, the percentage of these sources has steadily dropped over the past 2 decades, as mainly replaced by wind power. There is a surge in generated wind electricity from below 0.5 TWh in the 2000s to over 8 TWh (21.71 %) in 2021; meanwhile, the share of electricity from solar power is still below 0.5 TWh (< 1%).

Table 2. Finland's net electricity generation from RES [30].

| Renewable energy sources | Electricity generation in year | | | | | |
| | 2003 | | 2010 | | 2021 | |
	Quantity (TWh)	Percentage (%)	Quantity (TWh)	Percentage (%)	Quantity (TWh)	Percentage (%)
Hydroelectric	9.55	50.42	12.87	53.29	15.71	41.51
Wind	0.09	0.48	0.29	1.2	8.22	21.71
Solar	<0.01	<0.05	<0.01	<0.041	0.31	0.82
Others (incl. biomass)	9.29	49.05	10.98	45.47	13.61	35.96
Total	18.94	100	24.15	100	37.85	100

Considering the growing importance of electricity from solar and wind power in near future, the next content in this chapter would discuss electricity generation from these two sources. It can be said that the intermittent characteristics of wind and solar sources are a serious obstacle to their high penetration of them into the electrical grid [33,34]. In the case of wind energy, it is obvious that the power is highly intermittent and non-dispatchable, which means that its output fluctuates relying on many parameters such as wind speed, air density, turbine characteristics, etc. This is also the case for solar energy, in which the intermittency comes from the variability of the season, shining time, cloudy and rainfall conditions, and other factors.

2.1 Solar power

Today, the technologies transforming solar power into other energy forms, especially electricity, have caught lots of attention. Table 3 illustrates a brief classification of several typical solar technologies [35,36].

Table 3. Classification of solar technologies [35,36].

Passive type	Active type	
Solar energy is collected, stored, and used as a heating source	Solar thermal Solar energy is collected and concentrated and further converted into electricity via specific equipment	Photovoltaic The semiconductor material is used to directly convert solar energy to electricity

In this thesis, only active type solar technologies, whose main objective are electricity generation, would be discussed. According to OurWorldinData [37], Chile has the highest share of electricity from solar ~13 % followed by Spain ~10 % and Italy ~9 % compared to around 4 % of the world in 2021. In terms of quantity of annual electricity generation, in 2021, the world produced around 1000 TWh, in which China is the biggest producer with one-third generated electricity, USA and India produced 163 TWh and 68 TWh respectively [38]. Based on the data of the International Renewable Energy Agency (IRENA), almost all solar-based electricity comes from photovoltaic technology; to be specific, over 800 TWh was generated in 2020 compared to only ~13 TWh of concentrated solar power [39].

According to National Renewable Energy Laboratory (NREL) [40], the global quantity of concentrating solar power (CSP)-based electricity is around 9162 MW in 2021. Spain, USA, Morocco, and China dominate the share with 2304 MW, 1740 MW, 1330 MW, and 1034 MW, respectively. The largest CSP plant in the world is Noor Complex Solar Power Plant in Morocco located in the Sahara Desert. This project can produce 580 MW and adequately supplies over 1 million people at maximum capacity.

According to OurWorldinData, in 2021, the solar PV cumulative capacity on global scale reached over 800 000 MW, of which one-third comes from China and USA has a 10 % share [41]. The world's largest solar PV power plant is Gonghe with a 2200 MW capacity located in a 5000 hectares area [42]. In Finland, the Kivikko photovoltaic plant located in Helsinki and the Suvilahti photovoltaic plant are the largest solar plants. The capacity of the Kivikko plant is as over twice that of Suvilahti and reaches over 800 MW [43]. Atria Nurmo's factory owns the largest solar park in Finland with peak power that can reach to 6 MW and this solar park can produce 5600 MWh annually which is equal to around 10 % of all generated solar energy in Finland based on data in 2018 [44]. Soon, a new solar park in Imatra would be

built with more than 100 000 solar panels, which can provide nearly 40 MW output under favourable conditions; meanwhile, in Lapua, EPV energy company started to build one of the biggest solar power plants in Finland – Heinineva solar power plant covering 170 hectares by about 200 000 solar panels and the maximum output of the plant is 100 MW [45].

The intermittency of solar-based electricity is dependent on the shining period, which means that the longer the shining time, the more generated electricity. Figure 5 (left side) illustrates the fluctuation of forecasted electricity from solar power (MWh) in Finland from 01/08/2022 to 07/08/2022; meanwhile, the trend of forecasted yearly solar electricity in 2021 in Finland is shown in Figure 5 (right side) [46]. It is obvious that solar power follows day-night pattern and the high-capacity period of solar plants in Finland is summertime from May to September.
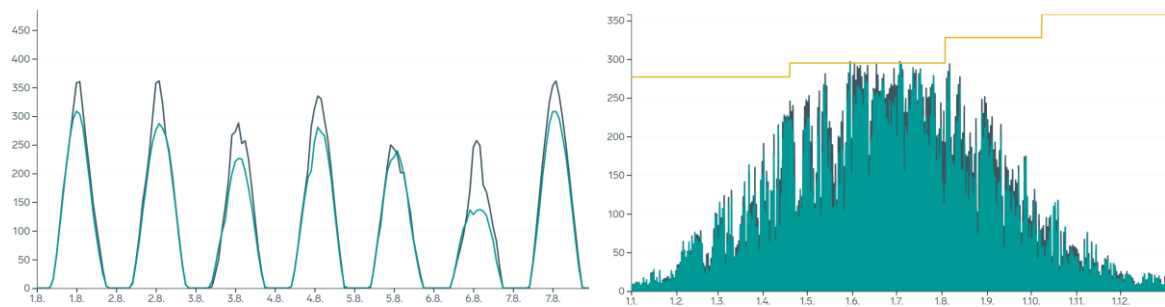
Figure 5. Solar electricity in Finland 01-07/08/2022 (left side); solar electricity in Finland in 2021 (right side) [46]. The light green line represents the day ahead solar power forecast, the dark green line represents the continuously updated solar power forecast, and the yellow line represents the total production capacity used in the solar power forecast.

2.2 Wind power

Similar to solar power, wind energy is a non-dispatchable and highly intermittent source, which has been used for thousands of years and has been applied as an electricity generation since the beginning 20th century. There are several typical features for this intermittency [36,47].

- The speed of wind varies due to the difference in day period, from season to season and it cannot follow a practical demand.

- At some periods, there is surplus electricity that should be stored; however, more effort needs to be put to find and develop suitability to satisfy technological and economic aspects.

- Wind farms are normally installed far away from consumers leading to high capital costs for the electricity grid.

Even if electricity from wind only accounts for over 5 % on global scale in 2020 [30], the rapid growth of this energy soon leads to a large share of wind-based electricity globally. To be specific, the annual electricity generation from wind increased from ~30 TWh to ~1800 TWh in the last 20 years with the majority of share from China (614 TWh), USA (379 TWh), Germany (115 TWh) in 2021 [48]. In some European countries, due to the stringent laws related to CO_2 emission reduction and advanced technologies, wind-based electricity registers a high share, including Denmark over half of the electricity was generated from wind in 2020, and the share in Ireland was over 30 %, followed by UK, Spain, Germany with the share in the vicinity of 20 % and the value of Finland at around 11 % [48]. Wind energy is typically classified into two types namely onshore wind farms, in which wind turbines are installed on land, and offshore wind farms, contrary to the former, in which large turbines are installed in bodies of water. In fact, generated electricity from wind mainly comes from onshore wind ~1.5 million GWh compared to 0.1 million GWh of offshore wind [49]. The world's largest offshore wind farm is Hornsea 1 located on the east coast of the UK in the North Sea with 174 turbines and 1.2 GW of capacity; meanwhile, the Gansu wind farm in China is the biggest onshore farm with 7000 turbines and it can generate up to 20 GW, sufficient for 1 million homes [50].

Until the first half of 2022, cumulative wind electricity capacity in Finland reaches over 4000 MW corresponding to 1112 wind turbine generators with a gradual increase in terms of turbine size (average capacity ~5 MW in 2022) [51]. The 41 wind turbines of Piiparinmäki wind farm located between Pyhäntä and Kajaani is the largest operating wind farm in Finland with a rated output of approximately 211 MW and the annual capacity of up to 700 GWh, producing 1 % of Finland's electricity which is enough to provide electricity for 36,000 households [52,53]. Until mid-2022, the total capacity of installed wind farms in Finland is 784 MW compared to 671 MW in 2021 and 302.1 MW in 2020 [52]. There are six operating wind farms with output above 100 MW, namely Paskoonharju (117.6 MW, 2022), Metsälamminkangas (132 MW, 2022), Sarvisuo (151.2 MW, 2021), Piiparinmäki (211.4

MW, 2021), Välikangas (100.8 MW, 2021) and Kristiinankaupunki (117 MW, 2017) [52]. According to Finnish Wind Power Association (FWPA) [54], if all wind plants were operational on time, the installed capacity would reach nearly 1500 MW corresponding to 251 wind turbines in 2023. Construction of the largest wind farm in Finland is now carried out in Lestijärvi and the total capacity of this farm would be 455.4 MW, which means that it can produce over 1.3 TWh/year of electricity corresponding to 2 % of the total generated electricity of Finland in 2020 [53,54].

Unlike the intermittency of solar-based electricity mainly following day–night pattern, generated electricity from wind power fluctuates due to many factors such as weather conditions, local surfaces, obstacles, day and night periods or seasonal weather changes. As shown in Figure 6 (left side), forecasted and real-time wind-based electricity (MW) in Finland from 01/08/2022 to 07/08/2022 is highly disordered trends; meanwhile, the generated electricity in the country in 2021 in Figure 6 (right side) has somehow as similar trend as the trends in Figure 6 (left side), in which higher capacity of electricity production is seen from March to May and from October to December [55].

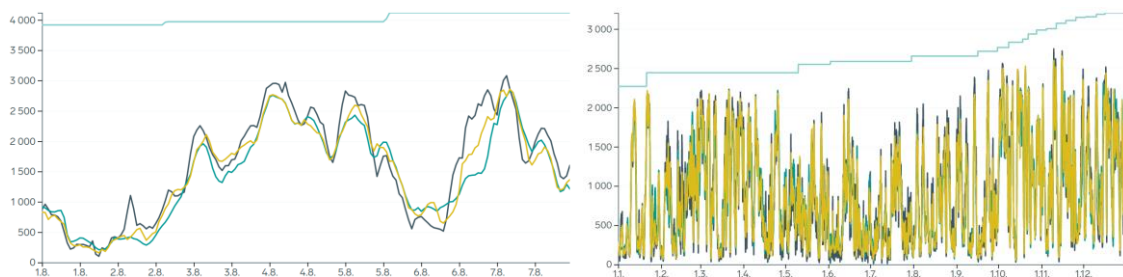Figure 6. Wind electricity (MW) in Finland 01-07/08/2022 (left side); wind electricity (MW) in Finland in 2021 (right side) [55]. The dark green line represents real-time wind power generation, the medium green line represents day ahead wind power forecast, the light green line represents total wind production capacity used in the wind power forecast and the yellow line represents continuously updated wind power forecast.

2.3. Main solutions for renewable energy power intermittency elimination

The previous sections showed the potential and the need for the development of solar and wind energy. However, the heavy reliance on climatic conditions causes a serious issue for high penetration of these energy forms into the electricity grid. Therefore, wind and solar energy forecasting play a crucial role to predict the intermittency of these sources [56,57]. Forecasting data can give end-users a general estimation of the generated electricity quantity from RES leading to a more stable and economic grid. There are several methods with reliable results that can be applied to the estimation, namely physics-based models, statistical methods, deep learning-based algorithms, and hybrid methods [57]. However, forecasting is more and more difficult due to climate change leading to unpredicted weather conditions. This asks for a more efficient and sustainable approach.

More effort should be put into technological aspects to overcome the issue. In this sense, there are two types of solutions: those not related to energy storage, and energy storage. In the former solutions, there are further two sub-solutions namely supply-side management (SSM) and demand-side management (DSM) [57]. In SSM solutions, the aggregation of fluctuating output of RES-based plants can reduce the fluctuation of final output [58,59]. In the case of DSM, the more efficient processes with advanced units are applied to reduce the load, and load pattern modification and consumer encouragement are also used to decrease the utilization during rush hours [57].

However, SSM and DSM still cannot completely solve the issue because RES intermittency can occur on a long-time scale and at fast short-time fluctuations. Therefore, balancing the demand and production is hardly possible. The application of electricity energy storage systems (EESs) is a promising approach due to the ability to store and release excess electricity efficiently. Table 4 will show the five common types of energy form in which RES-based electricity is stored [57,60,61].

Table 4. RES-based electricity storage technologies [56,59,60].

Energy Storage				
Mechanical	Electrochemical	Chemical	Electromagnetic	Thermal
Flywheel	RFB	PtG:	Supercapacitor	Low-temp
PHS	Lead-acid	H_2	SEMS	High-temp
CAES	NiCd	SNG		
	ZnBr	PtL:		
	NaS	MeOH		
	Li-ion	Formic acid		
		NH_3		

In which: PHS – pumped hydro storage, CAES - pressed-air energy storage, RFB - Redox Flow Battery, PtG – Power-to-gas, SNG – synthesis natural gas, PtL – power-to-liquid, SEMS - Superconducting Magnetic Energy Storage.

3 P2X processes

In this thesis, RES-based electricity storage in chemicals, or in other words power-to-X (PtX), is the main technology discussed throughout the report. The main reason is that unlike short-term storage technologies such as batteries, capacitors, PHS, and CAES, PtX is an effectively and sustainably long-term storage approach due to its high storage capacity, high volumetric density, no geographical dependence, and decentralized application [62]. It can be said that the PtX system acts as a "buffer" between the electricity grid from RES and the load of end-users via the chemical storage mediums. To be specific, the surplus electricity would be applied to produce the mediums, typically H_2 via water electrolysis. In case there is a shortage of electricity, H_2 or its derivatives, e.g., CH_4 or MeOH, can be used as feedstock in CHP to regenerate electricity for the grid. This cycle satisfies the simultaneous requirements of shaving the peak of RES-based electricity and regenerating electricity in case of overdemand [62,63].

In addition, CO_2 can be used as a feedstock in CO_2 hydrogenation in several PtX technologies such as methanol synthesis reactions, Sabatier reaction, or Fischer-Tropsch process [64]. These technologies do not only sustainably store electricity from RES, but also reduce CO_2 emissions and further produce more valuable chemical platforms. However, there are still challenges to successful application of PtX in practice, related to the new type of raw materials, unpredicted cost due to the intermittence, and especially the requirement for flexible operation [65]. Besides operation at normal capacity in a steady state, PtX processes need to have a flexible range of operating conditions, or to be combined with buffering storages (e.g., H_2) because of the change in availability of electricity. Therefore, a deep assessment in an advanced control structure for dynamic response is a need to fully understand and operate system efficiently. This is also the aim of this thesis and would be discussed in more detail in the applied part.

Nowadays, H_2 is the most common "X" among the many PtX technologies for the transformation of renewable electricity into chemicals for storage. The reason is that H_2 is a crucial and versatile compound with a high lower heating value ~119 MJ kg^{-1}, which is over twice as high as that of other basic fuels such as methane ~50 MJ kg^{-1}, gasoline ~44 MJ kg^{-1}, diesel ~42 MJ kg^{-1} [11,64]. The important role of H_2 in PtX technologies is clearly shown in Figure 7 [62].
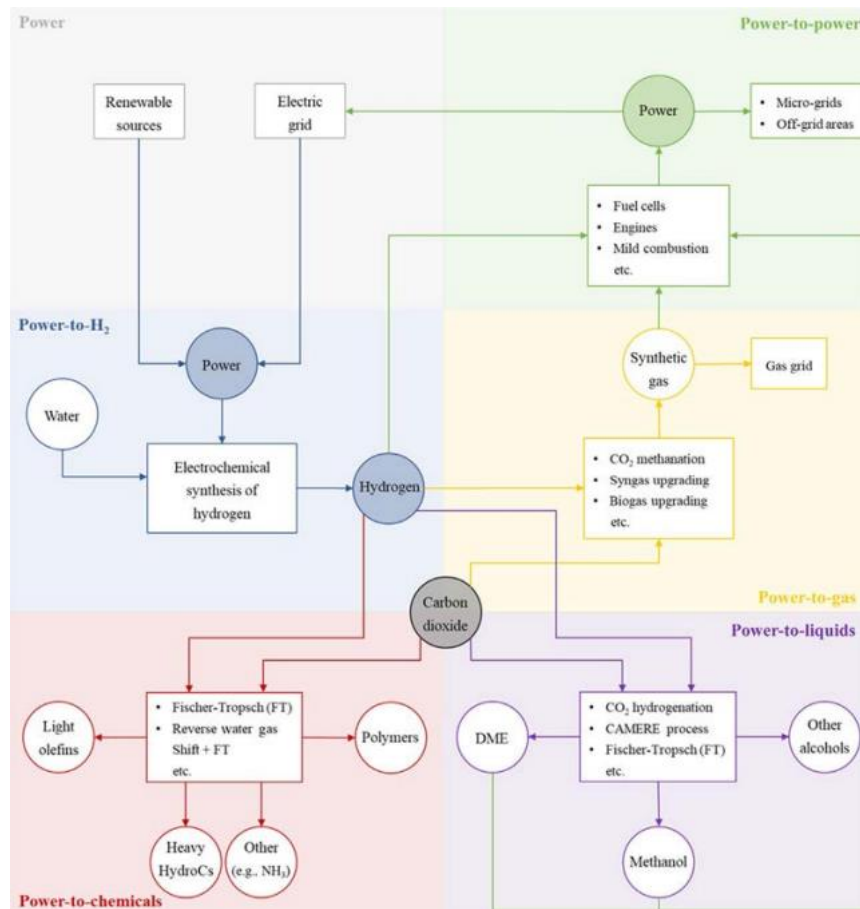
Figure 7. Several possible PtX routes with H_2 and CO_2 [62].

It is obvious that hydrogen from water electrolysis undoubtedly plays an essential role in the chain Power-to-H_2-to-gas-to-power, in which H_2 itself or its derivatives such as syngas or methane can be converted to electricity following end-users demand. However, the versatile applications from H_2 extend the pure objective of electricity energy storage (EESs) out of Power-to-gas (PtG) concept including other products such as liquid fuels and green chemicals. Along these novel routes, the integration of carbon source (CO_2) and N_2 (for ammonia production) is another promising aspect leading to more sustainable industries in terms of environmental aspects.

H_2 production technologies are mostly based on fossil fuels due to the certainty and cost-effectiveness of existing technologies [62,64]. However, stricter emission controls and reduced cost of electricity generation from RES have resulted in a renewed interest in water electrolysis [11,62,64]. There are several categories of electrolysis such as alkaline electrolysis (AEL), polymer electrolyte membrane electrolysis (PEM), solid oxide

electrolysis (SOEC) [62,64,66-68], microbial electrolysis, and biomass electro-reforming [64]. However, this chapter only discusses the first three types which have been already commercialized (AEL and PEM) or in the prototype stage (SOEC). The simple diagram of technologies of water electrolysis and the comparison between these technologies for hydrogen production are illustrated in Figure 8.

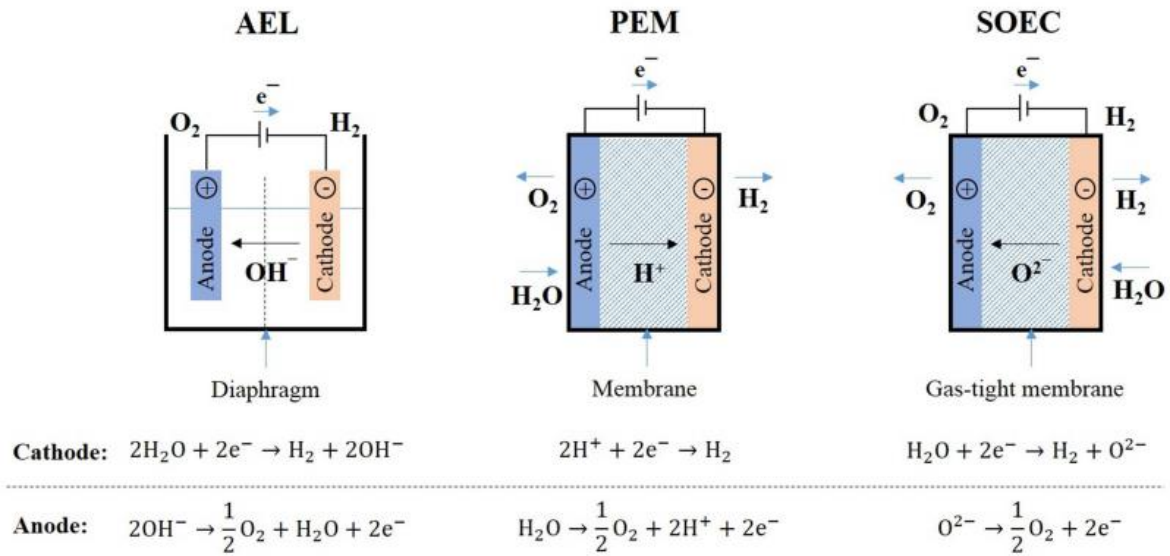|	**AEL**	**PEM**	**SOEC**
Cathode:	$2H_2O + 2e^- \rightarrow H_2 + 2OH^-$	$2H^+ + 2e^- \rightarrow H_2$	$H_2O + 2e^- \rightarrow H_2 + O^{2-}$
Anode:	$2OH^- \rightarrow \frac{1}{2}O_2 + H_2O + 2e^-$	$H_2O \rightarrow \frac{1}{2}O_2 + 2H^+ + 2e^-$	$O^{2-} \rightarrow \frac{1}{2}O_2 + 2e^-$

Figure 8. Water electrolysis technologies [64].

In AEL technique, two electrodes are immersed into an electrolyte e.g., KOH or NaOH with the concentration around 25 – 30 wt%; the process is operated at 60 – 100 ℃ and 1 – 30 bar [64,66,67]. This technique can achieve 99.9 % and 99 – 99.8 % of H_2 and O_2 purity respectively with 3.8 – 8.2 kWh/m^3 H_2 power requirement. The main advantages of AEL are low investment and capital costs, at 800 – 1500 €/kW, and high durability, 55 000 – 120 000 hours. In fact, AEL has been widely applied at the industrial scale, with examples including 3 AELs with 6 MW capacity operated at the Audi e-gas plant or the 1 MW AEL system of the BioCatProject [64]. Despite wide application, there are still some drawbacks of AEL such as low current density, corrosion issue of electrolytes and most importantly, the low dynamic flexibility (20 – 100 %) compared to PEM (0 – 100 %) and SOEC (-100 % to 100 %) [68] leading to the difficulty of co-operation with electricity generation [64,67].

In the case of PEM, a membrane is used to separate the anode and cathode. Produced H^+ is transferred to cathode by the membrane; meanwhile, electrons move from anode to cathode

via external load and H_2 is generated at cathode via the combination of H^+ and electrons [64]. The process can be operated at up to 150 ℃ in the range of $20 - 50$ bar with high purity of H_2 generation due to the prevention of gas crossover by the membrane. One of the most important advantages of PEM is the high flexibility with the intermittency of RES-based electricity because of the quick response of membranes, compared to liquid electrolytes. The major disadvantage of PEM comes from the high investment costs and the short lifetime of the membrane [64,67]. Because of this potential, PEM technique has been invested in by companies such as Siemens, AREVA H_2 Gen, Hydrogenics, etc. Air Liquide has planned to build a 20 MW PEM system in Canada and can be seen as the largest PEM electrolyser in the world [64].

SOEC electrolyser works based on the reverse process of a fuel cell, in which H_2 is generated at cathode from steam and electrons at anode; meanwhile, oxygen ions move through a membrane and combine, releasing electrons for the next cycle [64,67,68]. This system is operated at $700 - 1000$ ℃ resulting in the decrease of cell voltage leading to lower energy consumption [64]. The main advantages of this approach come from high flexibility with renewable electricity output, the ability of steam and CO_2 co-electrolysis, and the possibility of heat integration with other processes such as exothermic MeOH generation [64,68]. The major obstacle to commercialization of SOEC is the instability due to electrode corrosion in adverse conditions [64,68].
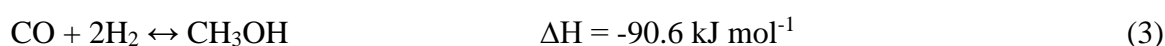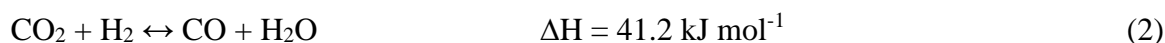
3.1 Methanol synthesis

Among the many "X" in PtX technologies, methanol is selected to be considered in detail in this thesis. Firstly, it can be used to regenerate electricity following end-users demand directly via the combustion process in a gas turbine or indirectly via electrochemical reactions in fuel cells. In addition, as mentioned in section 1, methanol is an essential C_1 block for valuable chemical synthesis e.g., DME, MBTE, formaldehyde, and hydrocarbons. It also shows potential as a fuel compared to fossil fuels or fuel additives. Finally, the green route for methanol production can integrate renewable electricity for H_2 production and the utilization of captured CO_2, possibly leading to a more environmental and sustainable approach in the future.

3.1.1 Theory for methanol synthesis

Nowadays, the most common feedstock for methanol production is syngas from natural gas reforming or coal gasification. However, the ever-increasing notices about climate change and sustainable development goals (SDGs) regulation have increased the interest in captured CO_2/biomass and electrolytic H_2 or novel technologies such as co-electrolysis of CO_2 and H_2O; biological oxidation of methane [9,69].

The first industrial methanol synthesis process was suggested by BASF in 1923 with the presence of catalyst - ZnO/Cr_2O_3 at high pressure (250 – 350 bar) and high temperature (320 – 450 ℃). However, in 1960, a new synthesis process published by ICI (now Johnson Matthey) replaced the BASF technique and has since been widely applied. The new process is operated at a lower temperature (200 – 300 ℃) and lower pressure (50 – 100 bar). The reactions related to low-pressure technology are shown in the following equilibrium reactions (1), (2) and (3) [9,69-72]:

$$CO_2 + 3H_2 \leftrightarrow CH_3OH + H_2O \qquad \Delta H = -49.4 \text{ kJ mol}^{-1} \qquad (1)$$

$$CO_2 + H_2 \leftrightarrow CO + H_2O \qquad \Delta H = 41.2 \text{ kJ mol}^{-1} \qquad (2)$$

$$CO + 2H_2 \leftrightarrow CH_3OH \qquad \Delta H = -90.6 \text{ kJ mol}^{-1} \qquad (3)$$
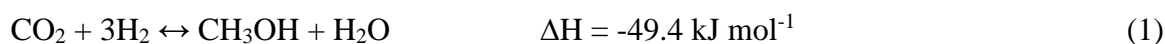
According to Le Chatelier's principle, methanol synthesis reactions (1) and (3) are favoured by decreasing temperature due to the high exothermicity and increasing pressure. Interestingly, there have been arguments about the mechanism of methanol formation as to whether it proceeds via CO_2 hydrogenation or CO hydrogenation. Today, it is widely accepted that methanol is generated via the hydrogenation of CO_2 [9,71]. In terms of the equilibrium aspect, methanol yield with different feedstocks at different conditions are reported by Dieterich et al. [70]. To be specific, pure CO_2 feedstock for hydrogenation shows a lower methanol yield (22 – 58 % at 60 – 100 bar and 200 – 250 ℃) compared to that of pure CO feedstock (58 – 89 % at the same operating conditions). The reason for the low methanol yield with the presence of CO_2 can be explained by the formation of H_2O leading to the shift towards the reactants side. The presence of CO can reduce H_2O content via the reverse water-gas-shift reaction [9,70,71]. In the application of commercial catalyst Cu-

ZnO-Al_2O_3, the main by-product of the CO_2 hydrogenation process is water (around 30 – 40 wt%); the content of other by-products such as C^{2+} alcohols, DME, esters, hydrocarbons, and ketones are below 500 ppm [73]. By-product formation might stem from the contamination of the catalyst with iron, cobalt, or nickel favouring FT reactions, or from the dehydration of methanol on the carrier Al_2O_3 [71].

There is an important parameter related to feedstocks, which is the stoichiometry number SN as shown in Equation (4) [9,70,71,74]. The optimal value should be 2, the value above and below 2 mean the excess and inadequacy of H_2 for methanol formation reactions, respectively. However, in practice, SN slightly above 2 (2.02 – 2.1) would be chosen due to the improvement of space-time yield (STY) and avoidance of by-products formed at a shortage of H_2 [70,74].

$$SN = \frac{H_2 - CO_2}{CO + CO_2} \qquad (4)$$

3.1.2 Catalysts

Following the first high-pressure methanol synthesis process is the application of catalyst of mixture ZnO and Cr_2O_3, which is stable to poison agents e.g., sulphurs and chlorine in feedstocks streams. However, the emergence of a new technique for catalyst preparation was partly attributed to the low-pressure methanol synthesis process [75]. In 1960s, the first commercial catalyst based on Cu-ZnO with carrier alumina was synthesized for the low-pressure technology by ICI [71,75]. Since then, the most common catalyst systems are all based on Cu-Zn-Al system synthesized via coprecipitation, with the ratio of Cu:Zn ranging around 2 – 3 and a small amount of Al [76] or other promising promoters such a Zr, Cr, Mg, and rare earth metals [70,71,75]. The main part of the catalyst comes from Cu centres, where the reactions take place; ZnO's objective is to improve the dispersion of Cu particles leading to the increase of catalytic surface and Al_2O_3's responsibility is to prevent undesired sintering of Cu particles and to enhance the dispersion of Cu centres [74]. More recent research in catalyst development has not significantly changed the performance of the process but has slightly increased the yield, catalyst stability, and lifetime [71].

Dieterich et al. [70] summarized the performance of methanol synthesis with different type of catalysts (variability of composition in Cu-ZnO-Al$_2$O$_3$) from several big licensors such as BASF, Shell, ICI, and Haldor Topsøe. The composition of BASF's catalyst is 38.5 wt% Cu, 48.8 wt% Zn and 12.9 wt% Al [77]. Meanwhile, MK-121 from Haldor Topsøe is composed of >55 wt% CuO, 21 – 55 wt% ZnO, and 8 – 10 wt% Al$_2$O$_3$ [78]. The comparison shows that the space-time yield (STY) varies in the range between 0.27 – 2.3 kg$_{Me}$ l$_{cat}^{-1}$ h^{-1} with low content of by-products (<1.3 wt%), at the operating conditions of 200 – 310 ℃, 39 – 122 bar and gas hourly space velocity (GHSV) around 10 000 h^{-1}. Catalysts are commonly produced as tablet shapes with the bulk density of around 1000 – 1300 kg m^{-3} [70,74,78].

Normally, the average lifespan of the catalyst is 5 years; a shorter time would result in an increase in capital cost of methanol plants [9,70,71] There are several key properties, e.g., metal surface area, defects, and metal-support interfaces, deciding the activity of the catalysts and these properties are significantly affected by the change of operating conditions. High temperature, presence of impurities, or high flow rate of feed streams can negatively affect the performance of the catalyst [71,75]. Besides the catalyst's degradation by process conditions, catalyst poisons should be also considered, especially by sulphur and halide agents. H$_2$S and COS can cover the active sites of Cu leading to a decrease of reaction yield; therefore, ZnO addition in catalyst structure protects Cu centres from poisoning. When Cu an Zn contact with halides, there is a formation of corresponding halides with lower melting points than that of the original form leading to sintering process [70,71].

3.1.3 Methanol process

In the methanol synthesis process, there are two main parts namely methanol synthesis and methanol separation and purification. One of the main challenges in the methanol synthesis part is the design of reactors with effective heat removal to avoid by-product generation and the ability to reach a high rate of conversion [70]. Reactors for the process can be classified into three different categories: fixed-bed reactors (FBRs), fluidised-bed reactors, and liquid-phase reactors.

Adiabatic FBR, polytropic reactor, and steam raising converter (SRC) are the common types of FBRs [9,70]. Adiabatic reactors are composed of series reactors with intercooling system

to remain the temperature of system. This design is quite simple to scale up, with no difficulty in catalyst maintenance and defined residence time. However, low heat transfer, hotspots presence, and large equipment size are the main drawbacks of this concept.

In SRC concept, catalysts are filled into the shell or tube side and the cooling water would flow in another side. Basically, this reactor has the same working principle as a shell-tube heat exchanger; to be specific, feed streams flow in the catalyst side and the heat released from reactions would be cooled down by water evaporation to medium-pressure steam on the opposite side. This design leads to a very good heat transfer and excellent heat recovery as well as temperature control. The high cost due to a large number of tubes is the main disadvantage of this reactor [9,70].

Fluidised-bed reactors and liquid-phase reactors are innovative approaches. Both are isothermal and possess improved heat transfer performance compared to FBRs; however, nonuniform residence time due to the generation of bubbles, mechanical degradation of catalysts, corrosion inside reactors, and the difficulty of scaling up are the obstacles preventing commercialization of fluidised reactors. Meanwhile, high stress on the catalyst is the drawback of liquid-phase reactors. In fact, only one industrial plant was built based on liquid-phase technology, which is the Liquid Phase Methanol concept designed by Air Products and Chemicals [9,70].

Nowadays, quasi-isothermal SRC is the most common reactor used for methanol synthesis. In this type of reactor, temperature profile varies in a narrow range, normally only one blunt peak of temperature is formed near the inlet of the reactor and the temperature slowly reduces along the length of the reactor. Several commercial reactor types are listed in Figure 9 by Dieterich et al. [70]:

- In Lurgi tubular reactor (a), feed gases flow inside catalytic packed tubes, meanwhile, cooling water is in the shell side generating medium-pressure steam.

- In Linde Variobar (b), cooling water flows inside a coiled tube, while catalysts are packed outside.

- In Toyo Multistage Radial flow (c), gases are radially distributed from the outside and the products are collected in the central channel after flowing through a catalytic bed, whereas cooling water is supplied inside coaxial tubes and generated steam is extracted in the external annular.

- In Mitsubishi Superconverter (d), gases are distributed into internal tubes and flow through outside catalysts, meanwhile, cooling water is supplied in the shell side as same as that of the Lurgi system.

- In Methanol Casale isothermal methanol converter (IMC) (e), hollow plates are put inside a catalytic bed and the bed is cooled down by the circulation of cooling water inside the plates.

- Haldor Topsøe adiabatic reactor (f) can be seen as a multistage adiabatic reactor with intercooling.

- Lurgi MegaMethanol (g) is composed of two reactors: the first reactor is cooled down by the cooling water as same as Lurgi tubular reactor case, meanwhile, the second reactor acts as a shell-tube preheater, in which the feed gases are preheated by the outlet stream of the first reactor.
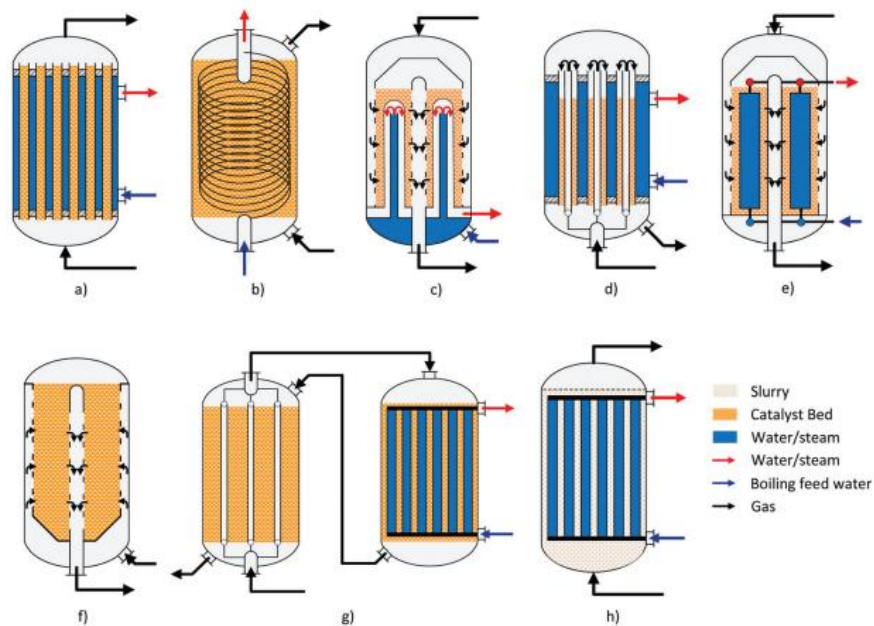

Figure 9. Simple reactor layouts [70].

According to above designs, the gas flow direction is a crucial factor having a significant effect on pressure drop. The pressure drop of radial flow reactors is below 0.5 bar compared to a significant higher value (over 3 bars) in the case of axial flow reactors. This feature is noticeably important in dynamic reactor modeling and affects the required energy for

recycled gas compression [9,70]. The main characteristics and operating parameters of mentioned reactors are shown in Table 5.

Table 5. Operating condition of several commercial reactors for MeOH synthesis [70].

	Lurgi	Variobar	MRF-Z	Super-converter	IMC	Haldor Topsøe	Mega Methanol
Vendor	Lurgi	Linde	Toyo (TEC)	MGC & MHI	Methanol Casale	Haldor Topsøe	Lurgi
Type	SRC	SRC	SRC	SRC	SRC	SRC	Adiabatic
Catalyst	Tube side	Shell side	Shell side	Double pipes	Shell side	Fixed bed	Shell side
Heat exchanger	Tubular	Tubular	Bayonet	Tubular	Plate	Intercooler	Tubular
T_{out}/T_{peak} (ºC)	255/270	N.A	240/280	190/270	225/280	290-N.A	220/270
P (bar)	50-100	50-150	80-100	55-100	65-80	50-100	75
Pressure drop (bar)	3	N.A	0.3-.05	2.4-7.5	1.1 (aixal) 0.3 (radial)	N.A	2-2.7
Reycle ratio	3-4	N.A	N.A	2-3	3	3-5	N.A
Per-pass conversion (%)	36	N.A	60	55-67	N.A	N.A	>80
MeOH yield (%) per pass	6-7	N.A	10	10-15	10.1-13.3	7	11
Max capacity (t d^{-1})*	1500-2200	4000	5000	N.A	7000-10,000	10,000	5000-10,000
Steam pressure bar	29-43	40	N.A	19-45	25-32	N.A	50-60

In terms of maximum capacity, Haldor Topsøe and Mega Methanol reactor technologies can achieve the highest value with a series of adiabatic fixed bed reactors and dual stages model respectively; meanwhile, other categories can be operated with maximum capacity with a single unit.

There are two crucial parameters affecting reactor size, which are recycle ratio (f_r) and gas hourly space velocity (GHSV), calculated by Equations (5) and (6):

$$f_r = \frac{\dot{V_{rg}}}{\dot{V_{fg}}} \tag{5}$$

$$GHSV = \frac{\dot{V_{fg,in}}}{V_R} \tag{6}$$

Where: $\dot{V_{rg}}$ and $\dot{V_{fg}}$ are the volumetric flow of recycled and feed stream, $\dot{V_{fg,in}}$ is the volumetric flow in standard conditions, V_R is the volume of the catalyst bed.

In terms of reactor design, there are some key parameters that need to be focused on. The operating temperature should be based on the range of the catalyst; high temperature would

increase the rate of reactions, whereas low-temperature choice can increase the overall conversion and reduce the formation of by-products. Recycling of gas for syngas feeding should be applied to improve the overall conversion of the process and f_R value should be designed at 3-5 [70,74]. However, the specified value must be assessed based on the size of the reactor and the required energy for recycled stream compression. GHSV directly affects the operation of a reactor. To be specific, higher GHSV, which means a higher feeding flow rate/ low residence time, might leads to a lower conversion level and higher pressure drop. Some commercial methanol synthesis reactors can be operated with GHSV in the range of 4000 - 30,000 h^{-1} [74]. Pressure drop is affected by the gas flow direction (<0.5 for radial flow and around 3 for axial flow). The percentage of purge stream depends on the accumulation of inert gas in system. Normally, this value varies from 2-6 v/v% with syngas feeding [9,70,74] and it could be lower in the case of CO_2 hydrogenation.

The crude methanol in methanol synthesis part would enter the downstream upgradation to meet the commercial standard: methanol for fuels corresponding to a purity over 99 wt%, methanol for chemicals production corresponding to the purity over 99.85 wt% [9,74]. The crude methanol would be fed into a low-pressure flash for light gas removal. Subsequently, the further downstream process determines distillation structure: a single column for fuels usage or two/three columns for chemical synthesis.

Based on mentioned ideas, a typical flowsheet for methanol production with a recycled stream and two-columns system is shown in Figure 10.
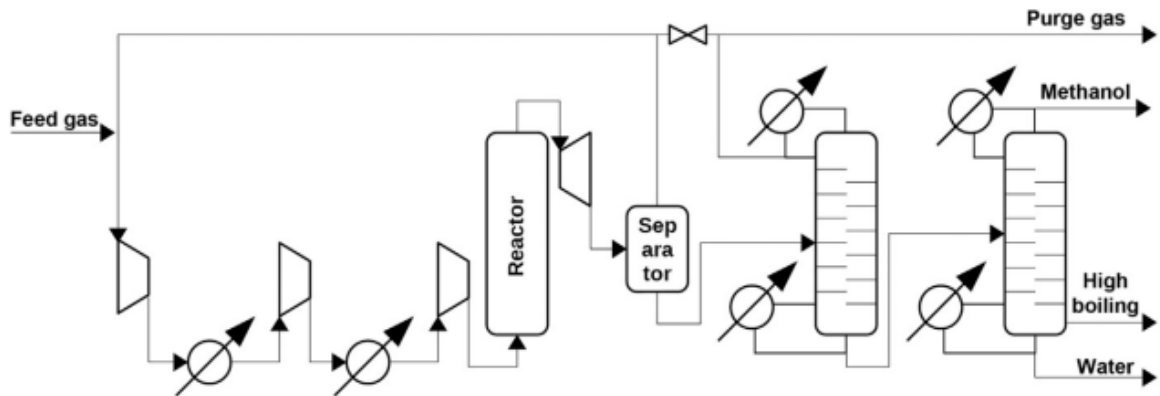
Figure 10. Flowsheet of methanol synthesis system [14].

4 Process control

The first theories and industrial applications of process control have been developed over a century ago and it has played a more and more important role in the rapid development of industries due to the difficult performance requirements for plants in recent years. For example, the stricter environmental rules and fossil fuel depletion have promoted the development of PtX technologies, which are more complex and highly integrated compared to conventional processes leading to high difficulty in terms of process control due to the intermittency of the RES power. Therefore, a deep understanding of controlling and the ability to design a well-performing control structure to remain the demanding quality and quantity with smooth operation and production rate is a must for the further commercialization of PtX technologies.

Figure 11 illustrates the integration of methanol synthesis with intermittent electricity networks based on solar and, wind power coupled with dynamic characteristic of water electrolyser, consequently leading to dynamic operations of the methanol synthesis process [79].
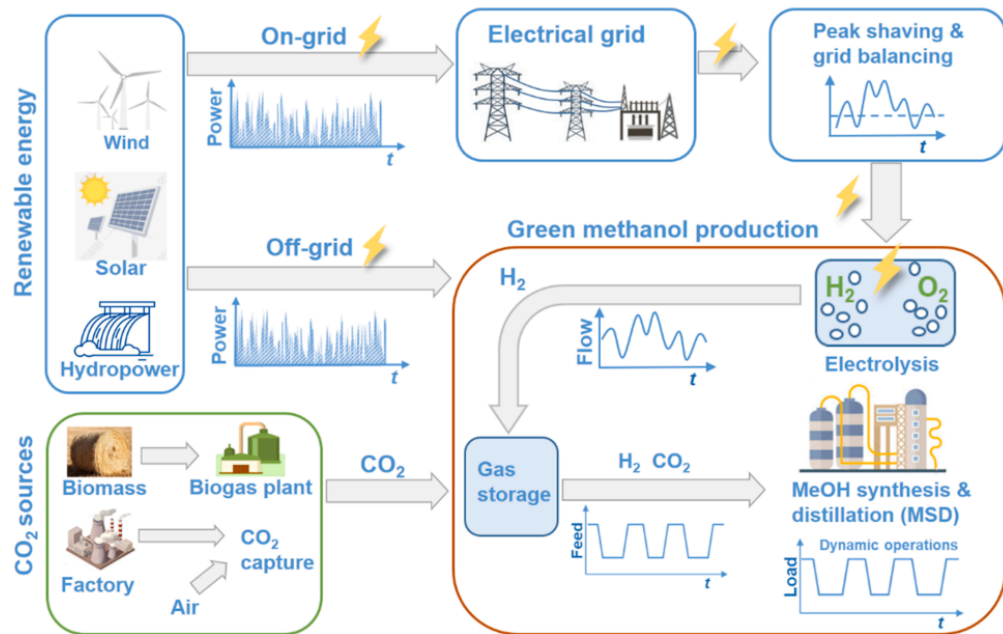
Figure 11. Scheme of power-to-methanol process [79].

There are several main control strategies namely feedback control, feedforward control, and the combination of these two methods [80]. In the feedback control method, the controlled variables (outputs) are measured, and that value is used to modify the manipulated variables (inputs). Normally, negative feedback is the common application of this method, in which adjustment is made to lower the error between setpoint and controlled variable. However, in some cases, controller sends wrong signal to manipulated variables leading to big error between the control variables and the setpoint. The main advantage of this method is that it can improve the stability of the process via error measurement, difference between the process variables and the desired values, and suitable adjustment regardless of the disturbance. In addition, feedback control application can reduce the dependence of process variables from disturbances. However, this method introduces noise measurement into the system, and thus no action is taken until the disturbance affects the system [80,81]. To overcome this issue, the second method – feedforward control should be applied. This approach allows noise measurement followed by action to cancel the noise before the process variables deviate from set points which results in a more stable operation. Unfortunately, this strategy does not take any action corresponding to unmeasured noises; in fact, not all potential noise variables are measured in practice due to economic aspects. Therefore, the combination of these two strategies is an efficient strategy widely applied in industries.

Feedback control takes action related to unmeasured disturbances, meanwhile, feedforward control considers measured disturbances before affecting the process [80].

4.1 Feedback control

Nowadays, there are two common methods of feedback control, namely on-off control and PID control. The latter has been widely used for 97 % of controllers in refining, chemicals, and other industries [82]. In the case of on-off control method, controller often offers overreactions due to the change of full action when there is an error between process variable (PV) and set point (SP) leading to increase of oscillations, consequently to the instability of the system. PID control with specified characteristics can overcome this issue.

4.1.1 Proportional-only control (P control)

In proportional control, which is the simplest control mode, the controller output is proportional to the error measurement between SP and PV following Equation (7)

$$p(t) = \bar{p} + K_C e(t) \qquad (7)$$

Where: $p(t)$ is the output of the controller, $\bar{p}$ is the steady-state value, K_C is the controller gain and $e(t)$ is the function of error over time.

The main theme of proportional control is that K_C can be modified with a positive or negative value to make controller output change, the bigger the absolute value of K_C, the bigger the controller output. The main drawback of P control is that there is always an offset (the difference between new SP and new PV after changing SP or sustained disturbance) regardless of the value of K_C, the increase of K_C results in a smaller offset [80].

4.1.2 Proportional-Integral control (PI control)

In the system requiring zero error in SP and PV, the addition of integral control can effectively eliminate the offset. In the integral control, the output is performed by following Equation (8):

$$p(t) = \bar{p} + \frac{1}{\tau_I} \int_0^t e(t^*)dt^* \tag{8}$$

In which τ_I is the integral time.

Equation (8) states that the output of the control is only constant when e(t*) is equal to zero, which means that at that state, the controlled process is at a steady state. When integral control is applied, the output controller will change until the error between PV and SP is zero unless the physical limit of manipulated elements is reached. In practice, integral control is conjugated with proportional control for effective control as a PI controller. The main disadvantage of integral control is the production of oscillatory output leading to instability of the process. In addition, an integral control action can result in an integral windup, which means the further accumulation of integral term when the controller reaches its limitation. This phenomenon usually occurs when there is a large SP change during the start-up of plant procedure or when there is an abnormal change in upstream/downstream process. Freezing integral term when the output reaches the limit can be used to avoid this situation [80]. The integral control is usually integrated with proportional control as presented in Equation (9) as the proportional-integral (PI) control action.

$$p(t) = \bar{p} + K_C \left(e(t) + \frac{1}{\tau_I} \int_0^t e(t^*)dt^* \right) \tag{9}$$

4.1.3 Proportional-Integral-Derivative control (PID control)

The application of derivative control can reduce the oscillation caused by the integral term via anticipation of future behaviour of the error by assessing the output rate of change. This is especially useful for sudden changes in the PV value. In these cases, P-only control is ineffective because it only reacts based on the error in PV, and SP, and there is no difference in the output regardless of the pace of the error increases or decreases. At the same time,

sudden change leads to large integral term and consequently saturates the controller. Making the output proportional to the rate of change of the error can deal with these limitations. However, when there are many noisy measurements such as high-frequency, random disturbances, derivative control would change violently resulting in noise amplification without a noise filter [80]. The controller output for derivative control action is shown in Equation (10).

$$p(t) = \bar{p} + \tau_D \frac{de(t)}{dt} \tag{10}$$

The general form of the proportional-integral-derivative PID controller is mathematically expressed in Equation (11). The actions of a PID controller are illustrated in Figure 12. To be specific, the error value at the time t determines the proportional term; the integral term is based on the integral of the error from the starting point to the time t. Finally, the derivative term states anticipation of the error trend based on the rate of change [81].

$$p(t) = \bar{p} + K_C \left[e(t) + \frac{1}{\tau_I} \int_0^t e(t^*) dt^* + \tau_D \frac{de(t)}{dt} \right] \tag{11}$$
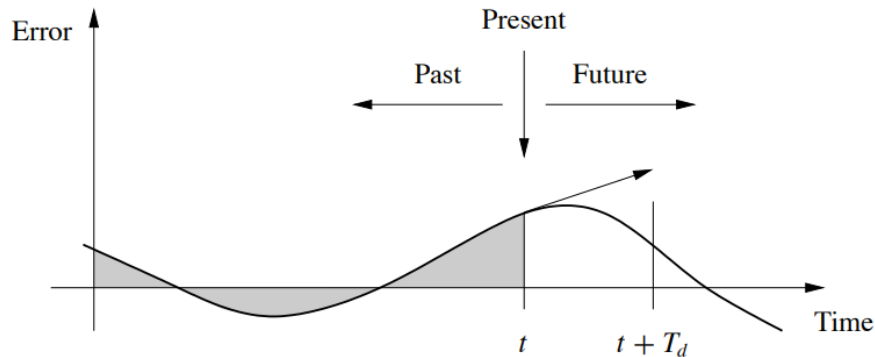

Figure 12. PID controller actions [81].

4.2 PID tuning methods

In practice, PID tuning, which is the modification of the parameters controller gain (K_C), integral gain (τ_I) and derivative gain (τ_D) to optimize process performance, is a crucial part of process design. Normally, tuning of a PID controller would be carried out during the start-up procedure, or when there is oscillation of controlled variables due to internal conditions of equipment (e.g., heat exchanger fouling), decrease in sensor measurements, or inaccuracy

in control valves, or other reasons. Tuning is a time-consuming activity based on the trial-and-error principle; however, results from tuning can offer effective controller settings leading to stable process operations. In fact, there is a trade-off between control performance and stability of processes, which means that high accuracy of tracking set points and elimination of disturbances should be considered in terms of process flexibility and stability at wide range of operating conditions [80]. There are three common types of tuning methods, namely continuous cycling method (Ziegler and Nichols method), relay auto-tuning (relay-feedback test), and step test method [80,81,83].

In continuous cycling method, after achieving a steady state, the PID controller is set to proportional-only control by setting integral term to zero and derivative term to a large value (10,000). Subsequently, output oscillations are made by changing set point followed by a gradual increase of K_C until stable fluctuation occurs. The value of K_C in that state is defined as the ultimate gain, K_{CU} and the period of output PV curve is the ultimate period P_U. Controller configuration for different type of controller is shown in Table 6. However, this technique is not suitable in slow-dynamic response processes and any disturbance during the test can lead to unstable operation [80,81].

Table 6. Controller setting related to continuous cycling method [83].

Controller		K_C	τ_I	τ_D
P		0.5 K_{CU}	-	-
PI	Ziegler-Nichols method	0.45 K_{CU}	P_U/1.2	-
	*Tyreus-Luyben method	0.31 K_{CU}	2.2 P_U	-
PID		0.6 K_{CU}	P_U/2	P_U/8

*According to Luyben [83], K_{CU} and P_U based on Ziegler-Nichols' method are too aggressive for most chemical process control, therefore, he suggested the Tyreus-Luyben method which is more robust and conservative.

In the relay-feedback test, the PID controller is replaced by an on-off controller. The only specified parameter is the height of relay (d), which is typically 5-10% of the output scale. The ultimate period P_U is defined as the period of oscillation of the PV (measured variable). Meanwhile, the ultimate gain K_{CU} is calculated following Equation (12).

$$K_{CU} = \frac{4d}{\pi a} \tag{12}$$

In which a is the maximum amplitude of measured variable signal

The PV starts to oscillate around set point and the controller output switches to opposite mode when the PV reaches set point. In this testing, a dead zone is applied to prevent frequent, random switch by noise measurement [80,83]. The major benefits of this method are: (1) simplicity (only relay of height needs to be specified) and short testing time, (2) the amplitude of the output can be limited by modifying the height of relay, (3) the effect of disturbance during testing period can be determined by different shapes of oscillations, (4) the process does not need to operate at a limitation as in the continuous cycling method. However, this method is also not suitable for slow dynamic-response processes [80,83].

4.3 Typical control structure

Designing a well-performing control structure is an essential requirement for an effective and smooth plant operation. In a typical control structure of a plant, there are several types of controls namely (1) flow rate control, (2) liquid level control, (3) gas pressure control, (4) temperature control, and (5) composition control.

The main components of a flow rate control structure are usually composed of an orifice-plate sensor, a transmitter, a controller, and a control valve. The dynamic response of this loop is fast and the time for valve adjustment is small. There is also noise generation causing flow turbulence, valve action, or pump vibration. Therefore, derivative action is hardly possible. In addition, the response of the control loop is fast, hence, it is not essential to get a faster action by derivative action. In practice, the recommended settings for controller are $0.5 < K_C < 0.7$ and $0.2 < \tau_I < 0.3$ mins [80,83].

In liquid-level control loops, P-only and PI control are commercially applied. In fact, if the tank acts as a surge tank, whose main objective is to reduce the fluctuation of downstream process, then P-only control is highly recommended for the sake of simplicity because maintaining the level of the tank at an exact value is not necessary. In this case, little or no control action would be taken when PV varies within limitations, and stronger actions only occur when the PV is close to the high or low limit. An interesting characteristic of this loop is that the higher the gain of the controller, the stabler the process is. Luyben suggested initial $K_C = 2$ for the P-only controller, while K_C should be increased to 10 when controlling the

level of important equipment such as reactors [83]. In that case, PI controller is the most desired, and subsequently, the gains can be calculated following St. Clair's suggestion [80] in Equations (13), (14), (15). Some cases require an accurate level control (offset elimination is desired) that if related to reactor level control and distillation column base or reflux drum level controls [83].

$$K_C = \frac{100\%}{\Delta h} \tag{13}$$

$$\tau_I = \frac{4V}{K_C Q_{max}} \tag{14}$$

$$\Delta h = \min{(h_{max} - h_{sp}, h_{sp} - h_{min})} \tag{15}$$

In which, h_{max} and h_{min} are the limit values of the liquid level, V is the volume of tank, Q_{max} is the maximum flow rate of control valve.

Pressure control is somehow similar to level control, as it depends on the objectives whether a tight or an average control is desired. However, in the case of gas systems, pressure should be more carefully controlled due to safety concerns. Normally, a PI controller is recommended in this case [80]. The process time constant can be calculated by the ratio of gas volume of system and the volumetric flow rate of the stream through the system. The integral time is set from 2 to 4 times the process time constant. The initial setting can be K_c = 2 and τ_I = 10 minutes. Due to the small response times compared to other processes, derivative action is often omitted from the controller.

In temperature control, the control structure and related components vary corresponding to different units such as heat exchanger, reactors, or distillation columns. For instance, temperature can be controlled by the flow rate of heating/cooling medium or by the temperature of medium in the case of reactors/heat exchangers [84]; or by temperature control can be coupled with reflux/feed ratio control in distillation columns [85,86]. PI and PID controllers are both applied for temperature control. The latter option would provide faster responses leading to more accurate control in certain cases. One of the dynamic characteristics of temperature control loops is the presence of deadtimes and system lags. This means that excluding these factors and simulating a tight control is unrealistic and can lead to adverse effects when applying the model in practice. Therefore, aggressive tuning is required in simulation to have a safety factor for further practical development. According

to Luyben, system lags and deadtimes are different for each type of control, with typical ranges recommended in Table 7 [83].

Table 7. System lags and deadtimes in simulation [83].

		Number	Time constant (minutes)	Type
Temperature	Liquid	2	0.5	First-order lag
	Gas	3	1	First-order lag
Composition	Chromatograph	1	3 to 10	Deadtime

Composition control loops are somehow similar to the temperature control loops. However, the measurement noise from instruments can cause serious instability in the control structure, and apparently, a PID controller should not be used in this case [80,83].

4.4 Reactor and distillation control structure

In a common chemical process, synthesis and product separation are the most important parts, which are typically represented by reactors and distillation columns. Therefore, building a well-performing control structure for these process stages is clearly required.

In this thesis, a plug flow reactor (PFR) is applied for gas-phase reactions, hence the general control scheme only focuses on this reactor category. Flow rate control, temperature control, pressure control, level control, and composition control (in some cases) are the main loops in reactor control. A typical flowsheet for a PFR with controllers and system lags is shown in Figure 13 [83]. The flow rate of the feed stream and reactor pressure are controlled in direct action mode via control valves (V7, V8), flow rate controller (FC4), and pressure controller (PC4), respectively. The temperature of the reactor is controlled by the flow rate of cooling medium. To be specific, the temperature of reactor (stream 14) is controlled by the controller (TC4). When there the temperature of stream 14 is higher than the set point of the controller TC4, TC4 will send a signal to open control valve V9 and V10 larger and vice versa. Notably, in a real system, only one valve should be used (normally valve V9) to satisfy the rule: only one valve is installed in a pipe containing liquid [83]. However, there is a bug in Aspen plus dynamics that requires two valves installation on one liquid-filled pipe (in the mode reactor with co-current/counter-current thermal fluid of plug flow reactor in Aspen

plus) and both valves will receive the same signal from TC4 at the same time [83]. A series of lag blocks (lag41, lag42, lag43) are applied to simulate more realistically the thermal lag, which is the required time for the heat transfer between cooling medium and process fluid, and from the process to temperature sensors.
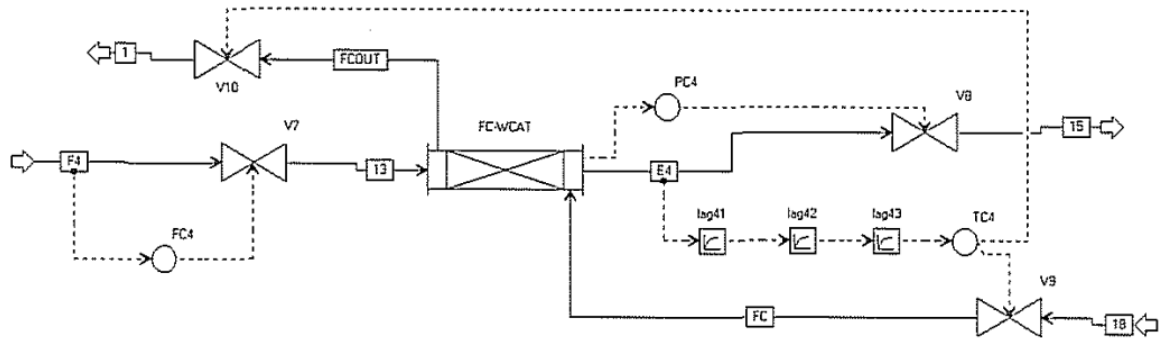

Figure 13. Control scheme for a catalytic tubular reactor with coolant flow [83].

However, the location for the temperature measurement for the control needs to be carefully considered. Normally, the outlet temperature is the most convenient choice because thermal sensor does not need to be inserted in catalyst tubes. However, in exothermic reactions, a good control should avoid hot spots during the operation. A control structure as shown in Figure 14 is a simple way for temperature control with exothermic reactions. A series of thermal sensors (TT) are assembled at different axial locations in the reactor. A high selector (HS) is used to receive the signal from sensors and the highest temperature signal of the reactor is sent to the temperature controller (TC). Subsequently, the temperature controller (TC) will send a signal to manipulate the flow rate of coolant via a control valve. When the temperature value from TT is higher than the setpoint of the controller (TC), then the valve of coolant would open wider and vice versa. This control setup can ensure there is no hot spot presence alongside the reactor.
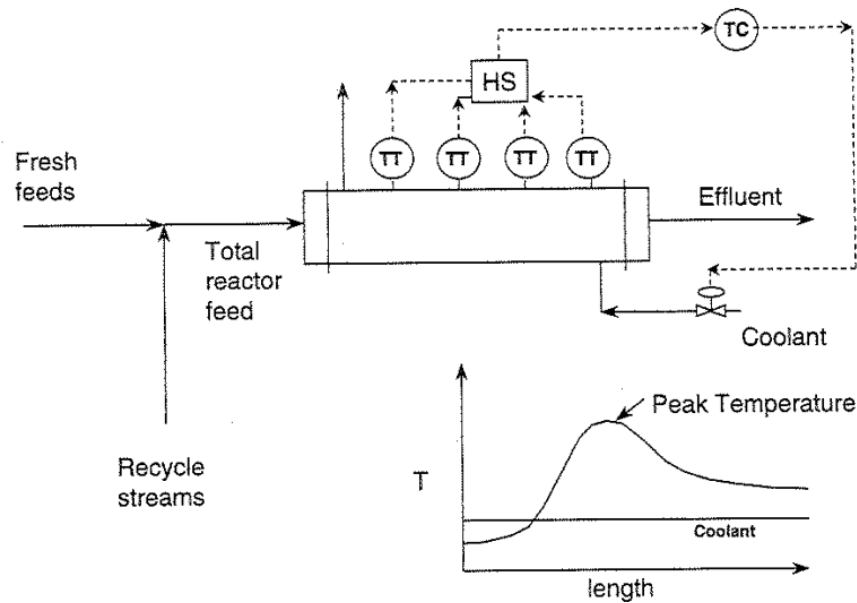
Figure 14. Peak temperature control scheme in a plug flow reactor [87].

In practice, multiple feed streams with specified stochiometric ratio and heat integration between inlet and outlet of reactor are usually applied (in Figure 15). The pressure of system is manipulated by the flow rate of one feed stream (F_{0A}). A combination of concentration controller (CC) and ratio control is introduced to control the ratio of inlets (F_{0A}/F_{0B}) by manipulating another feed stream flow rate (F_{0B}). The temperature outlet of the shell-tube heat exchanger (T_{mix}) is controlled by manipulating its bypass stream flow rate (F_{by}); the furnace (another heat exchanger) heat input (Q_F) is used to manipulate the inlet temperature of the reactor (T_{in}). In the temperature control structure of the reactor, a high selector (HS) will send the highest reactor temperature signal to the temperature controller (TC) and the reactor temperature is controlled by the pressure of generated steam via a pressure controller (PC). When the temperature of the reactor (TT) is higher than the setpoint of the controller (TC), the pressure of generated steam increases leading to a wider opening of control valve in pressure control structure and vice versa.
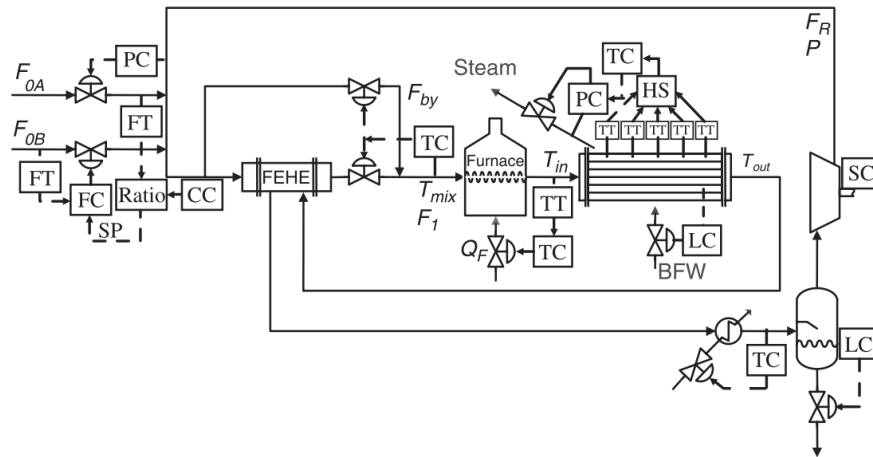
Figure 15. PFR with coolant medium control structure [84].

In the case of distillation column control, there are typically six control valves corresponding to six control degrees of freedom as illustrated in Figure 16, if feed conditions, column pressure, tray number, and feed location are fixed [87,88]. Normally, the valve in feed stream is used to control the throughput of the column (in some specified cases, the product valves, valves of cooling water stream, or valve of steam to reboiler can be applied). Two other degrees should typically come from the reflux tank and the base column level control by distillate and bottom product flow rate manipulation, respectively. The fourth degree is consumed for column pressure control via the cooling water flowrate. Finally, there are two remaining degrees of freedom that need to be set [87,89].
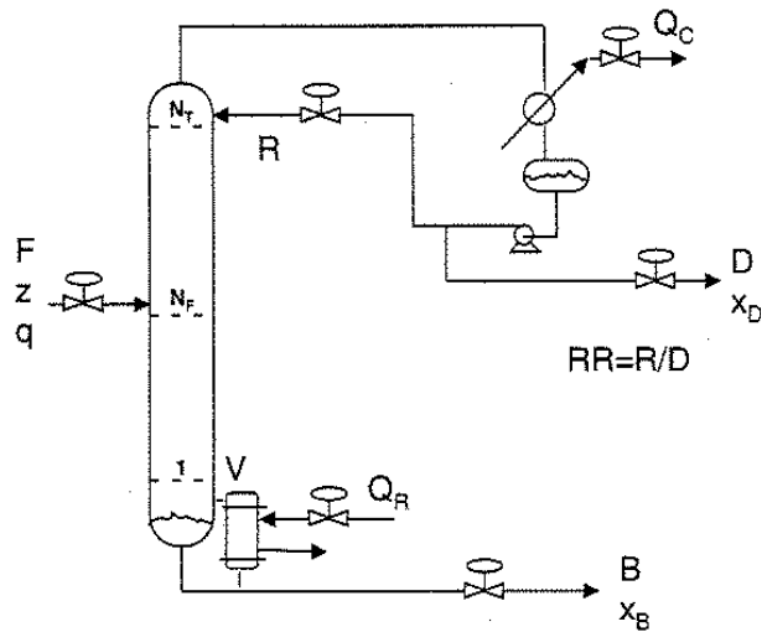
Figure 16. A basic control valves setup of a distillation column [87].

In an ideal case, two-composition (temperature) controllers are introduced to manipulate the impurity of a heavy-key component in the distillate and that of a light-key component in the bottom stream known as dual-composition control. However, composition measurement requires expensive equipment and high maintenance costs. In addition, there is a significant deadtime and system lag during the measurement coupled with potentially inaccurate results from online measurement. This results in the wide application of single-end control structures, in which one composition (temperature) is manipulated and another degree is chosen to limit the product purity variability via controlling reflux ratio or reflux/feed ratio (R/F) [85,87] The scheme with reflux/feed ratio control is illustrated in Figure 17 [85].
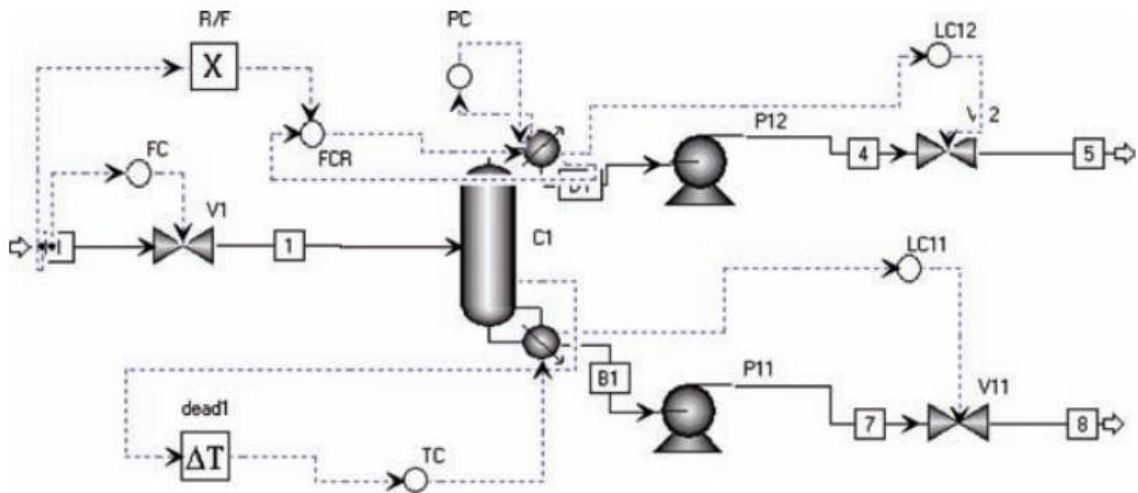
Figure 17. Control structure for distillation column with fixed R/F ratio [85].

In this flowsheet, level control for reflux tank (LC12) and column base (LC11), pressure control (PC), and feed flow rate control (FC) are as similar to the mentioned methodology in Figure 16. Temperature at selected tray is used to control the bottom quality via steam boiler manipulation (TC) with the application of deadtime (dead1). Meanwhile, a multiplier block (R/F) is introduced for the R/F ratio control, in which the feed flow rate and the R/F ratio are the input of the reflux flow control (FCR) and the output will set the reflux flow rate [85].

5 Dynamic modelling of methanol synthesis process

Compared to steady-state models, dynamic models are much more complex and are usually built based on existing steady-state models. In practice, it is impossible to operate a process at a steady state even with a tight control structure as there will be always disturbances affecting the process, leading to dynamic responses. Therefore, building a dynamic model plays a crucial role in terms of process dynamics and control. Dynamic model can help to gain a deep understanding of the process behaviour. Some commercial dynamic simulators provide valuable data for both states during the design phase of plants. Applying dynamic

modelling, different process operating conditions and process control strategies can be evaluated to determine optimal conditions and designs. Nowadays, the dynamic responses of variable outputs as a function of time can be solved via numerical integration techniques in common software integrating ordinary and partial differential equations. Examples of these software are MATLAB, POLYMATH, and Matcad. For the sake of simplicity, modular dynamic simulation tools have been developed, examples including ASPEN PLUS, HYSYS, ChemCAD, UniSim, and PRO/II, from which model parameters and initial conditions can be easily introduced into simulators by users [80].

As mentioned in the previous chapters, PtX processes have significant potential for long-term energy storage and further development for chemicals production. However, these processes are inherently dynamic in nature due to variations of electricity input and, hence, hydrogen production. Therefore, creating a well-performed dynamic model for PtX process is a must before building pilot plant and further, industrial plant. In this section, several dynamic modelling case studies about Power-to-methanol process is discussed.

Dynamic simulation of green methanol production was assessed by Cui et al. [79] by co-simulation between Simulink/Matlab and Aspen plus. The control structure of the methanol synthesis process is shown in Figure 18. In the report, dynamic behaviour was recorded during load changes, and evaluation of KPIs (key performance indicators), such as energy efficiency, and several important dynamic responses was made. Energy efficiency is the ratio of the energy output (such as the heat value of the fuels in stream outlets and waste heat/cooling/electricity sources as the utilities) to the energy input (such as the heat value of the fuels in stream inlets and the required energy from heating/cooling/electricity sources). The dynamic modelling is based on a steady-state model, in which methanol synthesis was carried out in the recycle PFR loop from pure H_2 and CO_2 with the stochiometric value $H_2/CO_2 = 3$, coupled with heat integration between the hot outlet and the cold feed stream of reactor (HX1). A single distillation column is used for methanol purification. The ramping time for load change (LC) between 100 % and 50 % is one hour and the total assessed operating time is 15 hours.
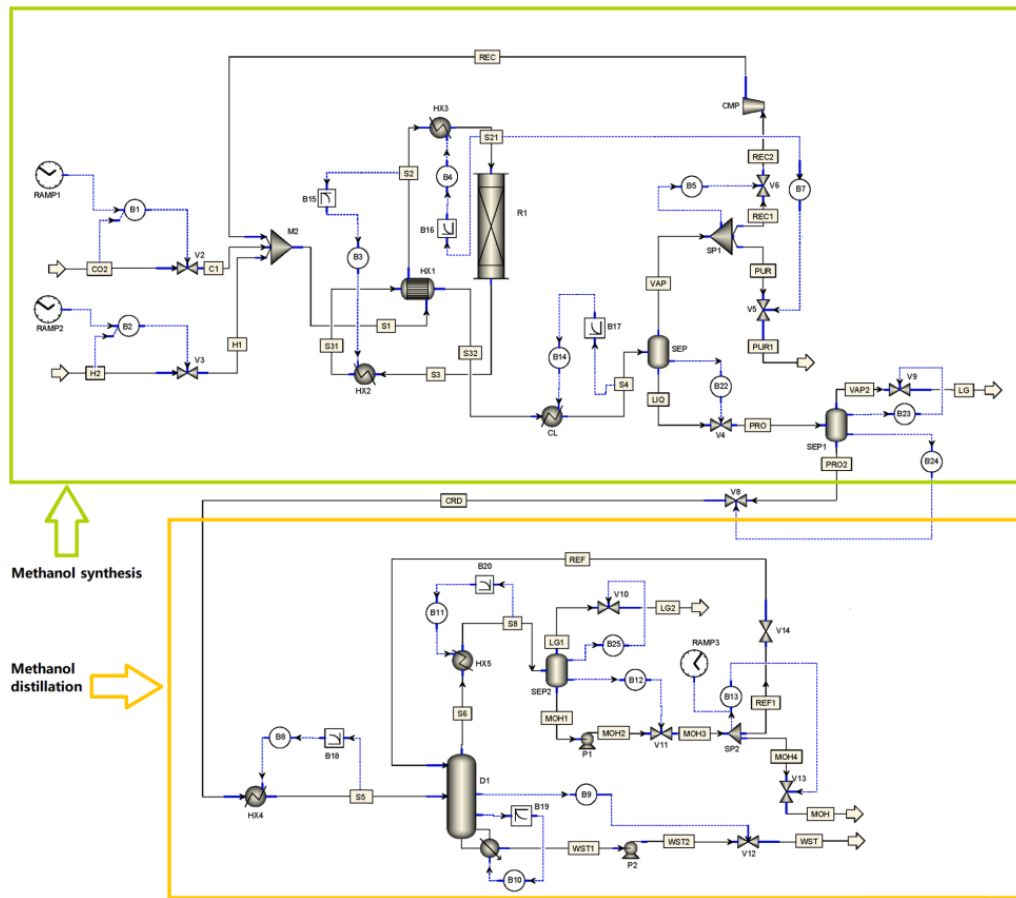
Figure 18. Control structure of methanol production via CO_2 hydrogenation [79].

Notably, all stream names in the following summary are based on Figure 18 following the reference [79]. A 50 % capacity decrease starting from 100 % loading during the time (t = 1 − 2 h) and a 50 % capacity increase back during the t = 8 − 9 h were carried out and the results are shown in Figure 19 (a), (b), (c). As shown in Figure 19 (a), the results pointed out that the flow rate trends of the crude methanol (CRD) and the purging gas (PUR1) agreed with the changes in CO_2 and H_2 feed. During the disturbance, a slow change rate in H_2, CO, and CO_2 composition in the reactor inlet (stream S21) was observed in Figure 19 (b). Notably, there is a slight difference in terms of per pass conversion of carbon between half-load (16.5%) and full-load mode (15.7%), which can be explained by favourable methanol synthesis reactions at slightly higher operating pressure enabled by the lower pressure drop at the half-load mode compared to the full-load. In Figure 19 (c), the duties of the heat exchangers, cooler, and compressor react linearly following the disturbance. To be specific, the heat duty of the heat exchanger HX1 is 6.21 MW and 3.1 MW at full-load mode and

half-load mode respectively. Meanwhile, the duty for cooling activity (block CL) of the full-load mode is also higher than that of the half-load mode at 3.29 MW and 1.4 MW respectively due to the higher temperature and flowrate of the inlet stream (S32). In Figure 19 (d), the energy efficiency at different ramping rates (ramping time T = 0.25 – 2 h) was also assessed starting from the decrease (100 % to 50 % loading) at t = 1 h and the increase back again (50 % to 100 % loading) at t = 8 h. At the ramping rate T = 1 h, the energy efficiency for methanol synthesis part slightly increased with a decrease in the load (from 87.7 % at 100 % loading to 90.2 % at 50 % loading). The results at different ramping times were also investigated and it can be concluded that the shorter the time, the more fluctuations are observed. For example, energy efficiency fluctuates in the range of ~88 % - 90 % with the ramping rate T = 2 h compared to more violent fluctuation (~ 79 % - 94 %) at T = 0.25 h.
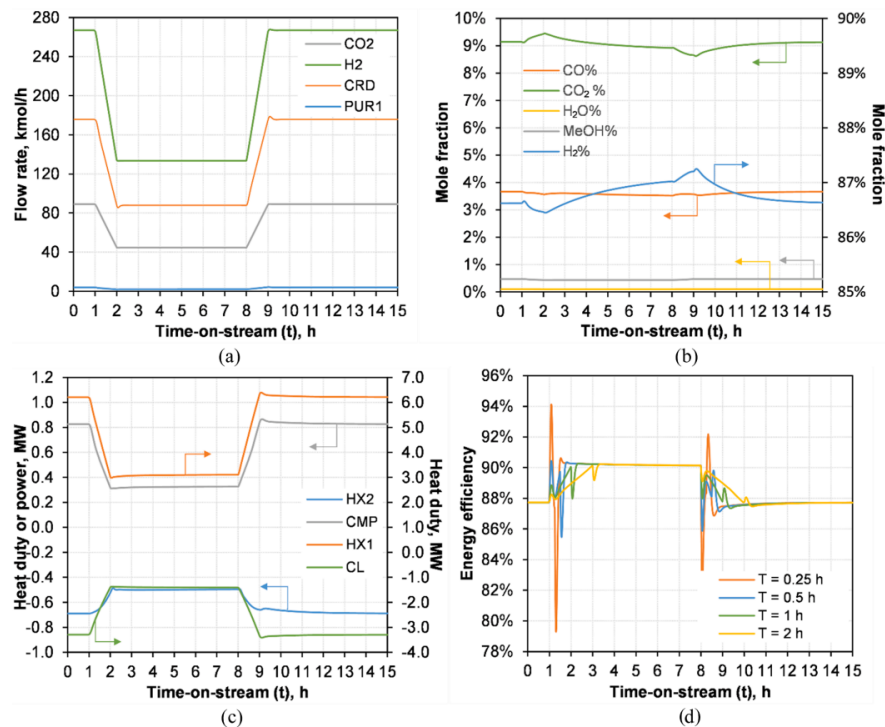

Figure 19. Dynamic behaviour of key parameters during load change in methanol synthesis part [79].

At the same ramping testing procedure in the methanol synthesis part, several important dynamic characteristics of the methanol purification part are shown in Figure 20. As illustrated in Figure 20 (a), in methanol distillation part, during load change conditions, the change of methanol (MOH) and water (WST) flow rate products are close to that of feed

stream (CO2) fluctuation with small undershoot at t = 2 h and overshoot at t = 9 h. In Figure 20 (b), the mass fraction of methanol (in stream MOH) and water (in stream WST) is almost consistently kept during the loading change. On the other hand, the reflux ratio (Reflux) of column (D1) linearly increases from 1.2 to 2.2 when loading changes from 50 % to 100 % capacity leading to higher reboiler duty, which is 1.4 MW and 1.91 MW respectively (Figure 20 (c)). At half-load mode, the vapor and liquid flow rates in the column are apparently small; however, there are limits to these flow rates to maintain efficient heat and mass transfer in the column. In Figure 20 (d), during 50 % capacity operation, the energy efficiency of the distillation part is lower than that of the synthesis part ~82 % compared to ~90 % (Figure 19 (d)) due to the mentioned higher reboiler duty.
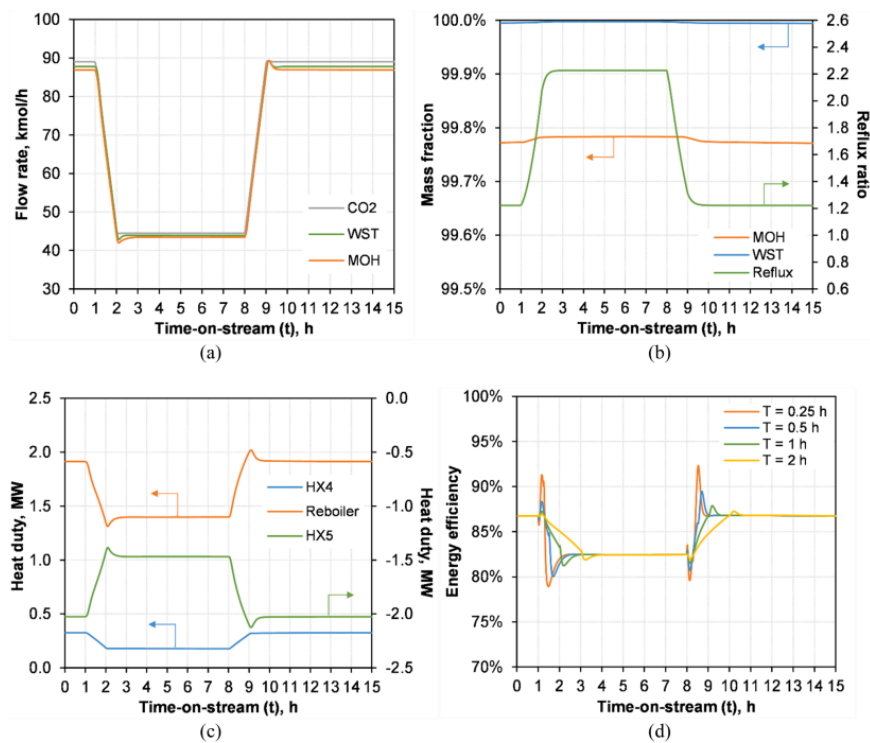

Figure 20. Dynamic behaviour of key parameters during load change in crude methanol purification part [79].

The trends of total energy efficiency for both parts in Figure 21 are somehow similar to that of the distillation part due to the big fluctuation of distillation part during disturbance conditions. The total energy efficiency is ~77 % and ~75 % at 100 % and 50 % capacities, corresponding to ~20 MW and ~10 MW power input. Cui et al. [79] suggested that there should be a methanol buffer tank between synthesis and distillation part to improve the total

efficiency of the process. In the reference, 50 % loading is the minimum operating capacity. However, in practice, due to the fluctuation of RES-based electricity, the minimum capacity could reach 20 % or even lower. Therefore, more research about the flexibility of methanol production should be carried out, especially for the control structure of the distillation part based on the constraint of minimum vapor flow rate.
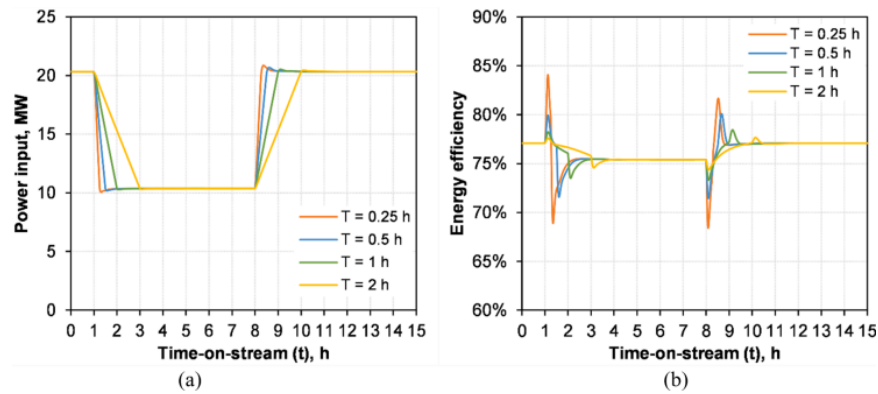

Figure 21. Power input and energy efficiency for the whole process during load change [79].

In the case described by Gonzalez et al. [90], dynamic modelling of methanol synthesis via CO_2 hydrogenation from electrolytic H_2 from wind and solar power was investigated to find out the general behaviour and dynamic limitations of a fixed-bed reactor. To be specific, fixed-bed reactor design could be carried out and data about catalyst deactivation obtained during dynamic operation would be achieved using the combination of experimental data and data from mathematical models, as shown in Figure 22. Based on collected experimental data and the balance equations from steady state and dynamic conditions, Gonzalez et al. reported the possibility to design a multitubular fixed-bed reactor in industrial scale for flexible loading operations. In the article, the released heat from reactions and the catalytic deactivation limitation based on the ratio of partial pressure of H_2O and H_2 (p_{H2O}/p_{H2}) are the key factors for reactor design. According to the article, the high ratio of p_{H2O}/p_{H2} translates into high oxidation ability of the gases leading to the deactivation of the catalyst. Increasing H_2/CO_2 ratio at the reactor inlet is a good approach for oxidation reduction, consequently resulting in high CO_2 conversion. In fact, with H_2/CO_2 = 8 and 4, there is catalyst activation when CO_2 conversion only reaches ~42 % and ~22 % respectively. With the ratio H_2/CO_2 = 22, CO_2 conversion can achieve values over 80 % without catalyst degradation. It means that high H_2/CO_2 condition leads to higher CO_2 conversion without

catalyst damage. The operating temperature should be between 250 – 300 ℃ to prevent poor kinetic characteristics at low temperature and catalyst deactivation at too high temperature. A series of conditions for the reactor recycling loop was set up such that the desired overall CO_2 conversion is 90 %, maximum value for p_{H2O}/p_{H2} is below 0.1 at the reactor outlet and the average flow rate of gases is 500 m^3 h^{-1} for the process variability in the range of 70 and 100 % loading.
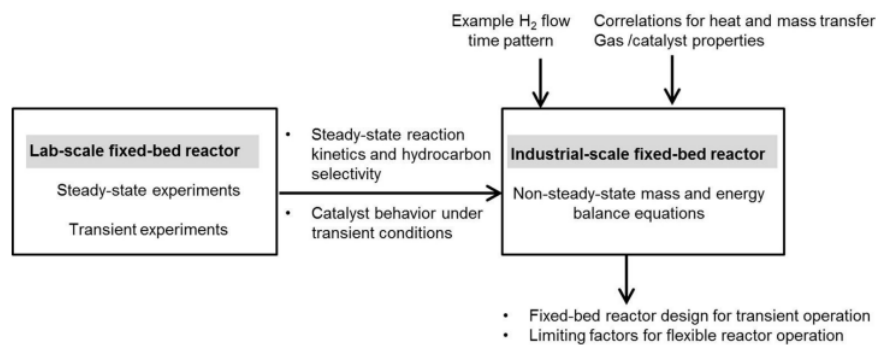

Figure 22. Methodology to assess the flexible operation of a multitubular fixed-bed reactor [90].

The molar flows of CO and H_2O at 70 % loading are definitely lower than the values at 100 % capacity due to the lower flow rate of the feed stream as illustrated in Figure 23. At minimum loading, per-pass conversion is 15 % consequently leading to a recycle ratio of 5.55, an overall CO_2 conversion of 93 % and a p_{H2O}/p_{H2} ratio that does not pass over 0.1. To satisfy the over 90 % CO_2 conversion, the average reaction rate needs to be higher by 40% in comparison to that of the minimum loading. However, the per-pass conversion reduces from 15 % to 11 % and the recycling ratio increases to 7.56 due to decrease in residence time. The pressure drop is three times higher compared to operation at 70 % capacity because of the higher gas velocity and because the power input for the recycle compressor rises to over sixfold to 23.83 kW from 3.68 kW as a consequence of high recycled flow rate and pressure drop.
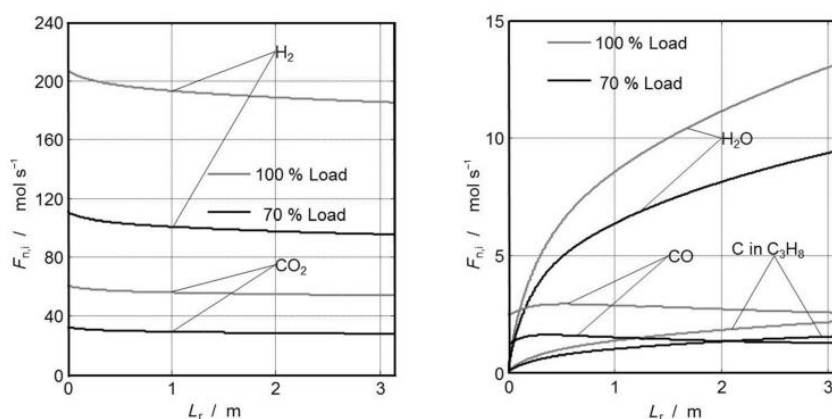
Figure 23. Flow rate of compounds along reactor length at different loading [90].

In the article of Gonzalez, a load change from 100 % to 70 % capacity with the rate of 5 % min^{-1} was evaluated (Figure 24). To be specific, the transition does not significantly affect the reactor and the variables are always kept within the specifications (maximum temperature 300 ℃ and p_{H2O}/p_{H2} ratio below 0.1). During the disturbance, temperature hot spot does not excess 300 ℃, but reaches 297 ℃ and 300 ℃ at maximum and minimum loading respectively. At the start, the amount of pure feed stream, which is mixed with stable recycled stream, decreases, leading to gradual increase in per-pass conversion and consequently in lower recycled and reactor inlet flow rates. The recycled stream achieves stable condition after 420 s. Meanwhile the pure feed stream comes back to a constant value after 366 s. In fact, no-dead-time condition was assumed in this modelling, which means that the residence time of the gas stream in separation units at downstream process is assumably zero. In other words, the gas at the reactor outlet is immediately mixed with the reactor feed stream. This might lead to optimistic modelling result; therefore, an adjusted factor should be added to the modelling equations for further research. The decrease in the load results in increase in per-pass conversion due to the lower flow rate of the recycled stream stemming from lower feed stream. The overall conversion stays always at a level over 90 % during the loading change.
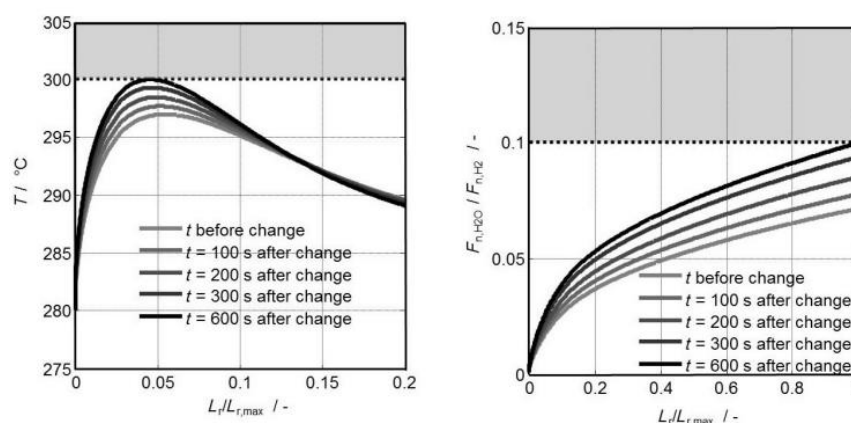
Figure 24. Dynamic behaviour of temperature reactor and H_2O content at the reactor outlet [90].

In the article of Chen and Yang [91], the flexibilities of two methanol production processes from electrolytic H_2 and captured CO_2 were assessed. In the first case, H_2 comes from solar power in Kranmer Junction, USA and in the second case from wind power in Norderney, Germany. In dynamic modelling, the load of the CO_2 capturing system and the methanol distillation system are kept at constant. Meanwhile, the load of the electrolysers and the methanol synthesis part were varied in a wide range. The surplus electricity from RES can be used for H_2 production and/or raw methanol synthesis and stored in a corresponding storage system for power regeneration during the shortage of RES power. Mass and energy balance data of the process were built using Aspen plus. Additional mathematical models about the flows and storages, renewable energy, and economic aspects were created, and the model was applied to assess the benefits of integrating RES electricity network with a flexible MeOH synthesis process at various sharing levels of renewable electricity or renewable penetration (f_L^{RE}) and dispatchable electricity price. Notably, renewable penetration is defined as the ratio of the used renewable electricity to the total power used in the methanol production process.

In the Chen and Yang's article, carbon capture system was modelled based on rate-based MEA absorption process case study [92]. An isothermal PFR for CO_2 hydrogenation was modelled in Aspen plus with the kinetic model adopted from Bussche and Froment [93]. In this part, the reactor was designed with high adaptability to excess loading and wide operating range corresponding to high intermittency of RES-based electricity. Meanwhile, the distillation column was modelled by RADFRAC model in Aspen plus to achieve 99.8

wt % methanol purity. The storage systems are composed of a H_2 storage system and liquified CO_2 and methanol tanks. The main objective of the article is to minimize the levelized cost of methanol (LCOMeOH) by a model that is based on the annualised cost of RES-based power, annual utility costs, and annualised costs for subsystems. For the sake of simplicity, several linear modifications were made, and the new linear model was introduced into GAMS (General Algebraic Modelling System) for solving by CPLEX solver [91]. Several assumptions were made in this work such as the capacity of electrolysers can immediately change from 0 to 100 % and the storage systems are unlimited in charging and discharging.

In base case scenario, methanol synthesis process was operated at two loadings: 10 % (flexible operation) and 100 % (non-flexible) capacity. Notably, in this article, besides non-dispatchable power: renewable electricity (wind- and solar-based ones), dispatchable electricity is a backup source when there is inadequate power for methanol production including electrolysis, methanol synthesis and purification. Related to electrified methanol production plant from wind energy in Nordeney, flexible application leads to significant renewable penetration (90.1 % compared to 48.3 %); meanwhile the LCOMeOH slightly reduces by 8 % compared to non-flexible design. This shows the high potential of flexible operation in terms of environmental aspects at lower production cost. However, it is not the case for solar-based electrified methanol production in Kramer Junction, because of the excess solar power or in other words, the low price of solar electricity leads to insignificant difference of LCOMeOH with flexible operation. Further investigation leads to the conclusion that the benefits from flexible operation could be prevented by the too high share of renewable electricity (f_L^{RE}) as shown in Figure 25. Note that, "flexible" term in Figure 25 means that the process can be operated at minimum load (in this case is 10 % loading). At non-flexible operation (100 % load), LCOMeOH achieves the most economical value with f_L^{RE} = 48.3 % (Nordeney) and 73 % (Kramer Junction); whereas f_L^{RE} = 90.1 % (Nordeney) and 81.3 % (Kramer Junction) in flexible operation show a slightly lower value of LCOMeOH compared to that value with 100 % of f_L^{RE} application. At both locations, the model with f_L^{RE} = 100 % shows significant profit of flexible conditions compared to that of non-flexible counterpart, in which LCMeOH in wind power case (Nordeney) is ~1300 $/ton at non-flexible operation compared to ~1000 $/ton at flexible operation. Meanwhile, the cost

of flexible case is lower by ~33 % in comparison with fixed operation in the solar power case (Kramer Junction).
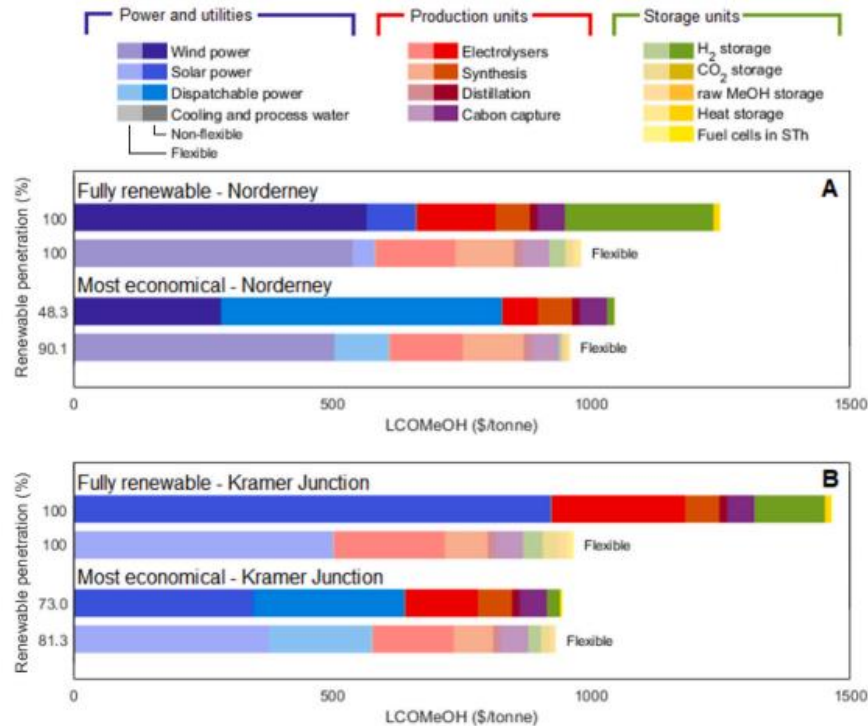

Figure 25. Distribution of cost components of LCOMeOH in the most economical case and full RES operation case for both Nordeney (methanol production plant from wind electricity) and Kramer Junction (methanol production plant from solar electricity) [91].

Chen and Yang also assessed the LCOMeOH and the share of renewable electricity (f_L^{RE}) with the variability of dispatchable electricity price and process operation. According to data in Figure 26, LCOMeOH would decrease with the broader range of load change of methanol synthesis reactor. For wind power case (Nordeney), LCOMeOH is ~950 $, ~1050 $, ~1120 $ and ~1200 $ per tonne corresponding to the minimum loading (ϕ_{min}) 10 %, 40 %, 70 % and non-flexibility at the price of dispatchable energy is around 200 $/MWh. In terms of the share of renewable electricity (f_L^{RE}), it can be concluded that at the same dispatchable price, the more flexible the operation is (low ϕ_{min}), the higher penetration level is achieved. However, when the dispatchable energy price is too high, consequently, there is no difference between the penetration level of the different process flexibilities, which means that the environmental benefits from the flexibility of the RES-based process would be gradually eliminated with the increase of dispatchable energy price.
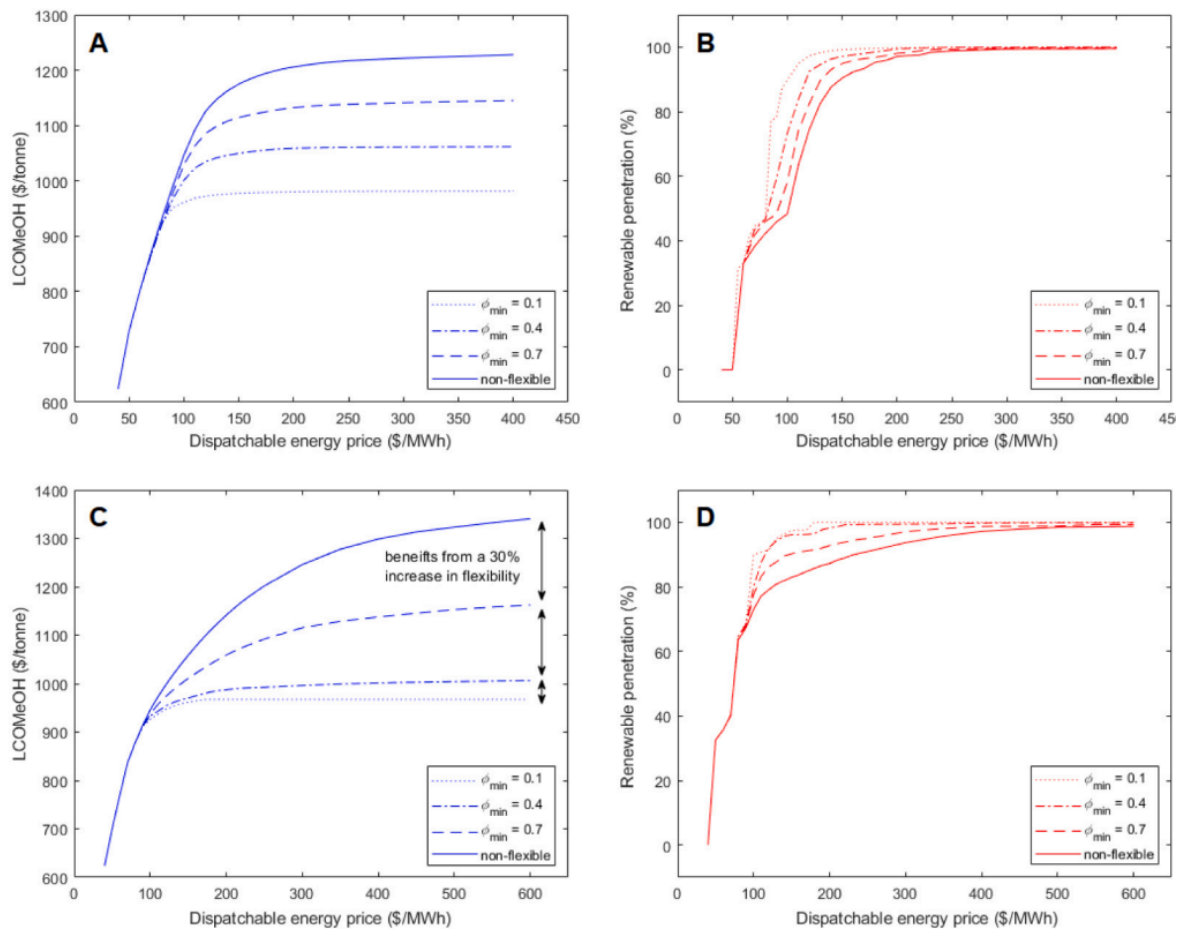
Figure 26. The relationship between LCOMeOH and dispatchable electricity price at different loading change [91]. (A) and (B) are presented for Nordeney, (C) and (D) are presented for Kramer Junction. ϕ_{min} is the minimum loading of methanol synthesis reactor, dispatchable energy is backup electricity when RES power is inadequate.

Abrol and Hilton [94] developed a dynamic model including a methanol reactor and a separator for recycled methanol synthesis loop based on a steady-state model to assess the flexibility of the process. Subsequently, the data from the model is applied to a linear model to create a linear model predictive controller (MPC). A low-pressure synthesis process was evaluated in this work. A gas-phase dynamic model for methanol reactor was built by a set of partial differential equations, which define the mass and energy balance in the reactor. The kinetics expression of reactions is illustrated based on the Langmuir-Hinshelwood-Hougen-Watson mechanism. Intra-particle diffusion limitations are also involved in the model. Modelling of a separator is used to anticipate the non-ideal behaviour of the polar gases in the process and Soave-Redlich-Kwong (SRK) equation of state is applied for flash modelling.

Dynamic behaviour of an open loop was investigated before introducing control structure. As shown in Figure 27, after starting point, a steady state of carbon conversion is achieved within 45 s without any disturbance from the initial value 96.75 % based on the optimal condition in steady-state model, to 96.63 %. Meanwhile, after a short certain period, gas compositions and temperature at the reactor outlet all reach a new steady state. In Figure 28, disturbances, in which the feed stream flow rate is decreased from 100 % to 50 % load and increased from 50 % to 100 % load, are applied at the starting point. The results pointed out that within 30 s, the process is able to reach a constant carbon conversion.

For a process based on solar power, there are some periods such as night, cloudy, or rainy periods, in which there is no syngas production. Then, the recycled stream would be operated with a minimum capacity (GHSV) to prevent condensation in the system, consequently leading to continuous operation without syngas make up feed. Methanol concentration and temperature at the outlet of reactor are dynamical assessed, and in less than 15 s, these values come back to the stable condition.
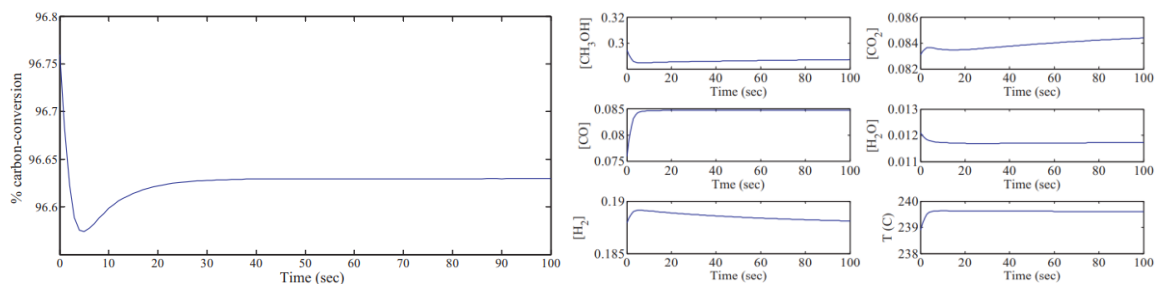

Figure 27. Dynamic behaviour of carbon conversion, gas compositions and temperature at reactor outlet without disturbances [94].
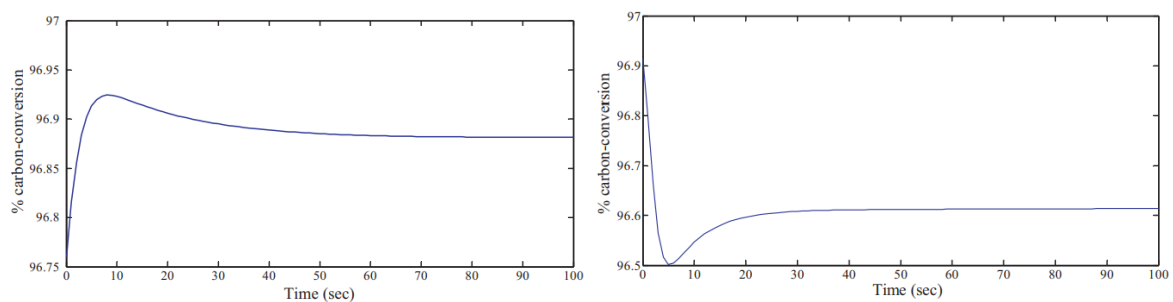

Figure 28. Dynamic response to loading change 100 % - 50 % (left side) and 50 % - 100 % (right side) at t = 0 [94].

After dynamic modelling, a linear model predictive controller (MPC) is designed to eliminate disturbance in the feed stream and to adjust the manipulated variables to shift the process towards stable state in quick response. In this work, the disturbance comes from the change of the feed stream flow rate. The reactor inlet flow rate, H_2O content in the liquid phase of the flask tank and the outlet temperature of the reactor are set to desired values by variating the shell-side temperature of the reactor, the flow rate of the purge stream and the by-pass stream. A test was carried out to assess the dynamic responses of the process with MPC application. At t = 10 s, feed stream flow rate is reduced two times and the set points of reactor inlet flow rate, H_2O content in liquid phase of the flash are also modified corresponding to the disturbance. The result of the closed loop with the MPC control structure shows high ability to follow up the change in set points without any offset and after 180-200 s, the new steady state is established without oscillation of the output.

National Energy Technology Laboratory built and tested dynamic operation of the LPMEOH^{TM} process [95]. In this concept, a part of syngas from coal gasifier is sent to methanol synthesis section during the excess syngas production or methanol from storage tank can be combusted to operate gas turbines for electricity regeneration leading to a stable operation of coal gasifier regardless of variability of the electric power demand for the gasifier. After testing during the project, it was concluded that the LPMEOH^{TM} process can be operated with wide range of H_2/CO ratio, the process can shut down or run with 100 % load and ramping rates in gas feed rates. The minimum ramping rate of the process is 5 % per minute showing that the process can be operated in a flexible and stable manner.

In Table 8, a short summary about dynamic modelling of methanol synthesis is presented.

Table 8. Summarized data about dynamic modelling of methanol synthesis.

Topic [Ref]	Methods	Results
Dynamic characteristics and energy analysis evaluation for methanol production process (MSD) [79].	A dynamic model consisting of methanol synthesis (MS) and purification (MD) was built in Aspen plus dynamics to assess dynamic responses during loading changes (100 % loading ↔ 50 % loading).	During ramping time of T = 1 h (between 100 % and 50 % loading), outputs flow rate, heat duties and required power for main equipment showed a good agreement corresponding to the input disturbances. Energy efficiency of MS, MD and MSD at (full-load and half-load mode) are 87.7 %/ 90.2 %, 86.8 %/82.4 % and 77.1 %/75.4 %
Dynamic modelling of fixed – bed reactors for methanol synthesis via CO_2 hydrogenation [90].	Dynamic characteristics and limitation of fixed-bed reactors during flexible operation were assessed based on the combination between experimental data of lab-scale reactor and mathematical model of industrial-scale reactor.	Increasing H_2/CO_2 ratio at reactor inlet can reduce the oxidation effect of H_2O to catalyst and CO_2 conversion can reach over 80%. Recommended operating temperature for catalyst protection is 250 ℃ – 300 ℃. At 70 % loading, per-pass conversion of CO_2 is higher leading to lower recycle ratio (15 % and ratio of 5.55) compared to 11 % and ratio of 7.56 at full loading. Both cases satisfy over 90 % CO_2 conversion and no catalyst damage. During capacity decrease from 100 % to 70 %, highest temperature of bed reactor does not excess limit (catalyst safety).

Table 8. Summarized data about dynamic modelling of methanol synthesis (continued).

Topic [Ref]	Methods	Results
The potential approach of renewable electricity integration to methanol synthesis [91].	Flexible operating electrified methanol process (including electrolysis (ELY), carbon capture (CC), methanol synthesis (SYN) and purification (DT)) from captured CO_2 and electrolytic H_2 based on wind (Nordeney) and solar (Kramer Junction) electricity data was modelled. Subsequently, mathematical model about levelized cost of methanol (LCOMeOH) consisting of costs of renewable electricity, utilities, and ELY + CC + SYN + DT was built to evaluate the benefit of the integration RES electricity and flexible MeOH production process at various sharing levels of renewable electricity (f_L^{RE}) and price of dispatchable electricity.	With wind electricity as input, the flexible operating leads to significant share of renewable electricity (f_L^{RE}) (90.1 % compared to 48.3 %); meanwhile LCOMeOH slightly decrease 8 % compared to non-flexible system. It is not the case of solar power case. However, 100 % f_L^{RE} can also lead to higher LCOMeOH, the most economical operating for wind-based electricity is achieved at f_L^{RE} 48.3 % and 90.1 % for non-flexible and flexible operating respectively. LCOMeOH for both f_L^{RE} operating modes is lower than that of 100 % f_L^{RE} mode. It is also the same case for solar-based electricity input, the most economical f_L^{RE} are 73 % (non-flexible) and 81.3 % (flexible). Notably, there is not a big difference of LCOMeOH between 100 % and 81.3 % f_L^{RE}. A combination between flexible operating (different ϕ_{min}) and variability of dispatchable electricity price was applied. The results pointed out that LCOMeOH decreases with a broader range of load changes. When the price of dispatchable electricity is too high, there is almost no difference of f_L^{RE} at various loading

Table 8. Summarized data about dynamic modelling of methanol synthesis (continued).

Topic [Ref]	Methods	Results
Modelling and simulation of methanol synthesis from syngas [94].	A mathematical model of methanol production consisting of a reactor and a separator as main equipment with recycled stream was built to evaluate the dynamic characteristics of the process.	After 45 s from starting point, carbon conversion is stable at 96.63 % compared to 96.75 % in steady-state model. A short certain time is also needed for gas composition and reactor outlet temperature to achieve a new constant value Feed stream flow rate variations (100 % loading $\leftrightarrow$ 50 % loading) at starting point was applied for dynamic responses assessment. After 30 s, carbon conversion reach to a new constant. A linear model predictive controller (MPC) was applied into the process and the results pointed out that the closed loop MPC can follow up feed rate variation without any offset and the process reach steady state after 180-200 s.
Dynamic operation of methanol synthesis from syngas in LPMEOH^{TM} process [95].	N/A	Excess syngas from coal gasifier can used to synthesize methanol and it was concluded that the process can be operated with wide range of H_2/CO, on/off mode, and ramping rates. The model is flexible and stable with the minimum ramping rate 5 % per minute.

APPLIED PART

6 Background

Design and operation of methanol synthesis with variating H_2 feed rate is challenging due to the process complexity. Therefore, it is probably beneficial to divide the process into two parts: crude methanol synthesis and methanol purification. Normally, a more comprehensive concept, which is power-to-pure methanol would be built and assessed. However, building a dynamic model for the power-to-crude methanol scheme has some advantages: (1) the absence of distillation columns in purification part leads to easier dynamic operation and control, (2) crude methanol at different wind farms can be stored and transported to a bigger plant for methanol purification potentially leading to cost reduction.

In this thesis, a dynamic model of crude methanol synthesis, which is the 1:1 mixture of methanol and water, from electrolytic H_2 and captured CO_2 (corresponding to ~25000 tons methanol/year) was built in Aspen plus dynamics environment based on publications that have been utilized in construction simulation model. Subsequently, the model was verified by comparison with a similar reference model [79] in terms of dynamic characteristics and energy analysis during flexible operation. In addition, the minimum process capacity and functional range of ramping rates were also investigated. Finally, real-time data of H_2 production from renewable electricity was applied in the model and the same procedure was carried out to evaluate the stability and validity of the model in practical conditions.

7 Dynamic modelling of power-to-methanol

7.1 Steady-state model

The dynamic model was built based on a previous steady-state model [96] with modified capacity corresponding to ~25000 tons methanol/year (in stream P-6-1) in Figure 29.
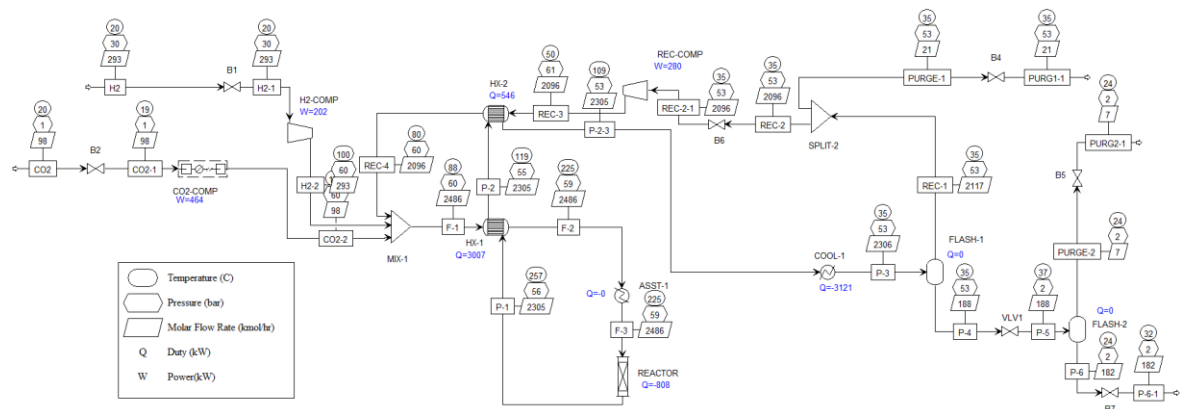

Figure 29. A schematic of steady - state model of crude methanol synthesis part [96].

In the steady-state model, electrolytic H_2 is compressed from 30 bar to 60 bar by a single-state compressor (H2-COMP); meanwhile, captured CO_2 is compressed from 1 bar to 60 bar by a multi-stage compressor (CO2-COMP). According to Walas' recommendation about maximum temperature of compressors outlet [97], the temperature should be in the range 177 – 204 ℃; therefore, a multi-stage compressor with intercooling stages is implemented to satisfy the limitation. Subsequently, compressed feeding gases are mixed with the H_2:CO_2 molar ratio of 3:1, and further mixed with recycled stream (REC-4) before heated up to 225 ℃ by utilizing the heat of reactor outlet (P-1) in a shell-tube heat exchanger (HX1). Another heater (ASSIT-1) is introduced between HX1 and methanol synthesis reactor to ensure the consistent temperature of the reactor feed (F-3) at 225 ℃ (ASSIT-1 is only used in the abnormal operating of HX1 and/or start-up process and would be ignored in dynamic modelling). The mixture (F-3) at 225 ℃ and 58.8 bar is fed into a multi-tubular fixed bed reactor (REACTOR) for methanol generation. Due to the high exothermicity of the process, the high-temperature outlet (P-1) is further applied to heat the feed stream (F-1) and recycled stream (REC-3) by heat exchangers HX1 and HX2, respectively. Then this stream would be

cooled down in a shell-tube cooler (COOL-1) to 35 ℃ before entering a flash (FLASH-1) for unreacted gas removal. After FLASH-1, unconverted gases (H_2, CO_2) are compressed back to 60 bar (REC-4) by a single-stage compressor (REC-COMP) before being mixed with feed gases and recycled to REACTOR. 1 mol% of stream REC-1 is split and purged out as stream PURGE-1 to prevent the accumulation of inert gases in the process. A depressurization valve VLV1 is used to decrease the pressure of liquid phase (stream P-4) at 53.4 bar to 2 bar for further light gases (PURGE2-1) removal from crude methanol (stream P-6).

Notably, for the sake of accuracy of dynamic model in terms of pressure drops and flows, there are the introduction of several valves in steady-state model with specified pressure drop (0.5 bar) and the pressure drop setting in HX1 and HX2 (1.2 bar for both sides) leading to the lower reactor feed pressure (58.8 bar) compared to "normal" condition – 60 bar. A plug flow reactor with constant thermal fluid temperature (230 ℃) was applied. Langmuir-Hinshelwood-Hougen-Watson kinetic model for CO_2 hydrogenation and water gas-shift reactions published by Vanden Bussche and Froment [98] with modified parameters based on the reference [99] (in Equations 16 and 17) was used to simulate methanol synthesis process. The unit of reactions rates are kmol kgcat^{-1} s^{-1}.

$$r_{MeOH} = \frac{1.07 \times 10^{-13} \times e^{\frac{4811.2}{T}} \times P_{CO2} \times P_{H2} - 4.182 \times 10^{7} \times e^{\frac{-2249.8}{T}} \times \frac{P_{MeOH} \times P_{H2O}}{P_{H2}^2}}{(1 + 3453.4 \times \frac{P_{H2O}}{P_{H2}} + 1.578 \times 10^{-3} \times e^{\frac{2068.4}{T}} \times P_{H2}^{0.5} + 6.62 \times 10^{-16} \times e^{\frac{14928.9}{T}} \times P_{H2O})^3} \tag{16}$$

$$r_{CO} = \frac{122 \times e^{\frac{-11797.5}{T}} \times P_{CO2} - 1.1412 \times e^{\frac{-7023.5}{T}} \times \frac{P_{CO} \times P_{H2O}}{P_{H2}}}{(1 + 3453.4 \times \frac{P_{H2O}}{P_{H2}} + 1.578 \times 10^{-3} \times e^{\frac{2068.4}{T}} \times P_{H2}^{0.5} + 6.62 \times 10^{-16} \times e^{\frac{14928.9}{T}} \times P_{H2O})^1} \tag{17}$$

The key operating conditions and parameters are shown in Table 9.

Table 9. Operating conditions and key parameters of steady-state model.

	Parameters	Value
Operating conditions	H_2 flow rate (stream H2), kmol/h	292.5
	CO_2 flow rate (stream CO2), kmol/h	97.5
	Temperature of feed gases (CO_2, H_2), ℃	20
	Pressure of feed gases (H_2/CO_2), ℃	30/1
	Reactor inlet temperature (stream F-3), ℃	225
	Reactor inlet pressure (stream F-3), bar	58.8
	FLASH-1 temperature, ℃	35
	FLASH-1 pressure, bar	53.4
	FLASH-2 temperature, ℃	37
	FLASH-2 pressure, bar	2
	Ratio for purging gas (SPLIT-2) mol%	1
REACTOR	Number of tubes	450
	Tube length, m	5
	Diameter of tube, m	0.0365
	Thermal fluid temperature, ℃	230
	Heat transfer coefficient (thermal fluid – process stream), $W\ m^{-2}\ K^{-1}$	118.44
	Gas hourly space velocity (GHSV), h^{-1}	25745
	Pressure drop (process stream side), bar	3
	Catalyst bed voidage	0.285
	Particle density, $kg\ m^{-3}$	1190
Single-stage compressors	Polytropic efficiency	0.85
	Mechanical efficiency	0.95
Muli-stage compressors	Polytropic efficiency	0.87
	Mechanical efficiency	0.98
Heat exchangers	Heat transfer coefficient ($W\ m^{-2}\ K^{-1}$)	850
	Pressure drop on both sides, (bar)	1.2
Valves	Pressure drop, (bar)	0.5

7.2 Transition from steady state to dynamic model

Besides many key parameters for the successful convergence of a steady-state model, other additional data such as size of flashes, heat capacity of catalyst, plumbing configuration (introduction of valves, compressors, and pumps) etc, which do not affect the steady-state

results, must be set up in steady-state environment before converting to dynamic model [83]. In Aspen plus dynamics, there are two options of dynamic simulation modes namely flow-driven mode and pressure-driven mode. In the former mode, Aspen only takes into consideration the mass balance of the process; meanwhile, the latter mode, which requires more setting of pressure and pressure drops to ensure all streams would flow from high pressure to low pressure region. In this thesis, the dynamic model, which is mainly in vapor phase, was built in pressure-driven mode leading to accurate and realistic model comparable to a real process.

In addition, there is a difference in terms of thermodynamic model application. To be specific, in Aspen plus, based on the specified properties of components, a suitable property package can be selected for an accurate simulation. However, in Aspen plus dynamic, there are 2 property modes namely Local and Rigorous mode, which means that users can allow dynamic simulator using approximate property relationships rather than rigorous methods in steady-state model. In fact, this is a trade-off: simpler relationships (local mode) selection probably leads to different results in dynamic environment compared to results in steady-state mode. However, this selection results in faster simulations and computing burden reduction, especially in complicated processes. The default setting – Local mode with approximate properties [83] would be chosen in this thesis for the sake of acceptable computer time (the real time that integrator in Aspen uses to solve the model).

As discussed, sizing equipment is a crucial step before the transition from steady state to dynamic simulation because the size of equipment directly affects the disturbance propagation of that unit. The bigger the size, the smaller the changes in process variables. Theoretically, heat exchangers, reactors and flash need to be sized and further configured before changing to dynamic mode. However, due to the lack of information about the setup procedure of mass and volume in heat exchangers in Aspen plus as shown in Figure 30, only flash and catalyst part were sized and specified in this thesis. Notably, the heat exchanger area and overall heat transfer coefficient for shell-tube heat exchangers as well as dimensions and specifications of REACTOR (multi-tubular fixed-bed reactor) are automatically updated in Aspen plus dynamics based on the same value in Aspen plus model.
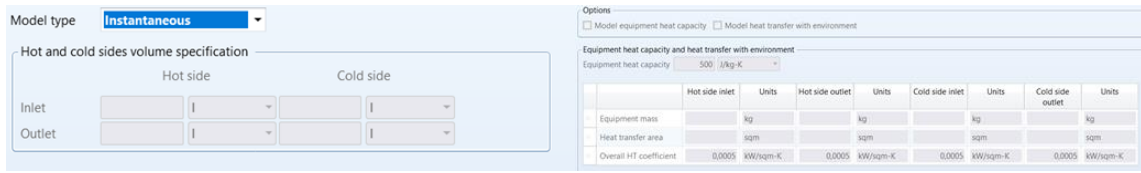
Figure 30. Configuration windows for shell-tube heat exchangers sizing in Aspen plus.

At this conceptual design level, a rough estimation was used to calculate the size of equipment following Luyben's recommendation [83]. To be specific, there are several assumptions that need to be set for flash tanks: (1) the liquid holdup of tanks is 5 minutes at 50 % level and (2) all flash tanks are vertical cylindrical vessel with the ratio of height to diameter at 2:1. Subsequently, the diameters based on maximum vapor velocity and volumetric flowrate of liquid are calculated and the larger value would be selected for dimension calculation. Diameter (D_g) based on maximum vapor velocity is calculated following Equation 18 and 19. A more conservative F – Factor 0.61 compared to 1.22 was applied for the effective separation in flash tanks [83].

$$V_{max} = \frac{F-Factor}{\sqrt{\rho_V}} = \frac{0.61}{\sqrt{\rho_V}} \frac{m}{s} \tag{18}$$

$$D_g = \sqrt{\frac{\frac{V_g}{V_{max}} \times 4}{\pi}} \ (m) \tag{19}$$

Where: V_{max} is the maximum vapor velocity (m s^{-1})

ρ_V is vapor density (kg m^{-3})

V_g is volumetric flow rate of vapor (m^3 s^{-1})

The diameter (D_l) based on volumetric flow rate of liquid is calculated following Equation (20)

$$D_l = \sqrt[3]{\frac{V_l \times 60 \times 5 \times 2 \times 2}{\pi}} \ (m) \tag{20}$$

Where:

V_l is volumetric flow rate of liquid (m^3 s^{-1})

The volumetric flow rate of liquid V_l is multiplied by 60 to convert from $m^3 \, s^{-1}$ to $m^3 \, min^{-1}$, subsequently V_l $m^3 \, min^{-1}$ is multiplied by 5×2 according to the assumption 5 minutes holdup with 50 % level of the tank to calculate the volume of tank.

Dimension estimation of equipment in Figure 29 is shown in Table 10 and the more detailed calculation of equipment is shown in Appendix 1.

Table 10. Equipment sizing and specification.

Equipment	Parameters	Value [Ref]
REACTOR (catalyst)	Heat capacity, $(J \, kg^{-1} \, K^{-1})$	1000 [79]
FLASH-1	Diameter, m	1.95
	Height, m	3.9
FLASH-2	Diameter, m	0.9
	Height, m	1.8
HX1 *	Heat exchanger area, m^2	117.2
	Heat transfer coefficient $(W \, m^{-2} \, K^{-1})$	850
HX2 *	Heat exchanger area, m^2	13.3
	Heat transfer coefficient $(W \, m^{-2} \, K^{-1})$	850

(*) All parameters are automatically specified in Aspen plus dynamics based on the values in Aspen plus.

Besides equipment sizing, valve sizing is also a crucial step for the transition to dynamic model. The normal pressure drops following Luyben's experience is in the range of 2 to 4 bar. However, in the case of gas system, there should be a consideration about the cost of compressing gas (lower pressure drops maybe better). In the model, the pressure drops for each valve is 0.5 bar at OP 50 % in design stage.

There are some notable points during the transition. To be specific, shell-tube cooler with cooling water as utility is not supported in Aspen plus dynamics leading to reconfiguration to thermal and phase state changer block. Normally, depressurization valve VLV1 (Figure 29) would be set at vapor-liquid phases due to the presence of small amount of light gases; however, Aspen plus dynamics does not allow multi-phase flow through a valve. Therefore, only liquid phase was set to exist VLV1 and this might be the reason leading to the remaining CO_2 in liquid phase of FLASH-2 (Figure 29). After the transition, there are differences of

several key parameters that need to be modified before controllers setting up, which is shown in Table 11.

Table 11. Differences between steady-state and dynamic model, and modifications (name of equipment in table is referred to Figure 29).

	Steady-state model	Initial dynamic model	Modifications
H_2 flow rate, kmol/h	292.5	290.3	Decrease temperature of H_2 from 20 to 17 ℃
CO_2 flow rate, kmol/h	97.5	97.4	Decrease temperature of H_2 from 20 to 19.5 ℃
Temperature of REACTOR inlet (F-3), ℃	225	226.6	Decrease overall heat transfer coefficient of HX1 (kW m^{-2} K^{-1}) from 0.85 to 0.815
Temperature of FLASH-1/FLASH-2, ℃	35/37	33/34.7	No modification due to the insignificant effect
Ratio of SPLIT-2, %	1	1.36	Cannot modify [a]
CO_2 content in crude methanol (P-6-1), mol%	0.4	2.3	Cannot modify [b]

(a) 1.36 mol% of purging gas does not significantly affect the process in terms of technological aspect.

(b) As discussed, due to VLV1 configuration (liquid-only), ~ 2 mol% CO_2 still remains in crude methanol. However, CO_2 can be easily removed in further purification process, or it is not a big concern when combustion turbine is applied in the next step.

7.3 Control structure

All coefficients in steady-state mode (full load) were applied into dynamic model during disturbances. The 100 % loading parameters and conditions are shown in Appendix 3. The detailed control structures with controllers and necessary blocks are shown in Figure 31 and Table 12. Notably, all controllers in the dynamic model are feedback controllers.
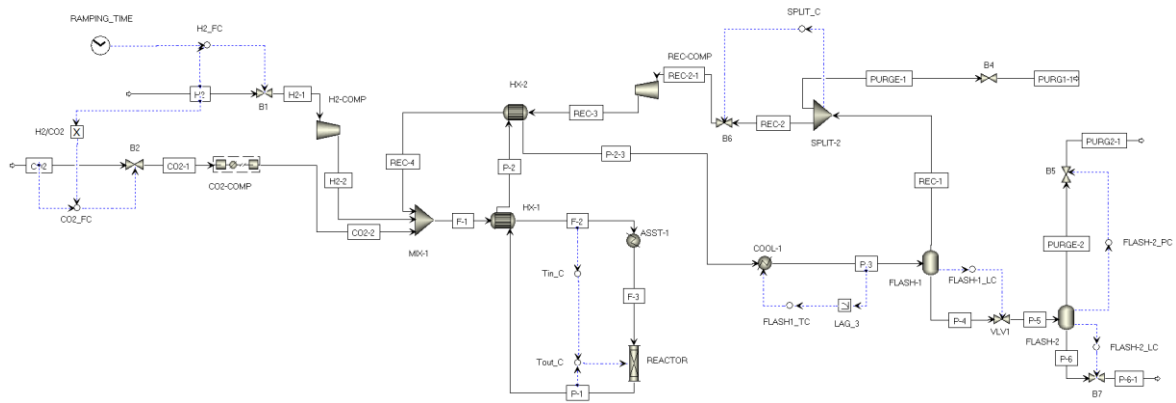
Figure 31. A control structure of crude methanol synthesis process.

Table 12. The description of controllers in dynamic model (in Figure 31).

Controller	Measured variable	Set point	Actuator	Range of change	P %/%	I (min)	Control action	Type of control
H2_FC	H$_2$ flow rate	292.5 kmol/h	Valve B1	0 – 100 %	23.6	1.32	Reverse	Auto
CO2_FC	CO2 flow rate	97.5 kmol/h	Valve B2	0 – 100 %	4.4	1.32	Reverse	Cascade
Tin_C	Reactor inlet temperature	225 ºC	Reactor outlet temperature	200 – 300 ºC	10.3	2.64	Direct	Auto
Tout_C	Reactor outlet temperature	Output of Tin_C controller	Temperature of generated steam	180 – 280 ºC	36.4	1.32	Reverse	Cascade
SPLIT_C	Ratio of REC-2/ REC-1	0.987	Valve B6	0 – 100 %	20	1.32	Reverse	Auto
FLASH1_TC	Inlet temperature of flash 1	33.2 ºC	Duty of cooler 1	-15 – (-5) GJ/h	9.9	1.32	Reverse	Auto
FLASH-1_LC	Level of flash 1	49 % height	Valve VLV1	0 – 100 %	30	1.32	Direct	Auto
FLASH-2_PC	Pressure of flash 2	2 bar	Valve B5	0 – 100 %	14.9	1.32	Direct	Auto
FLASH-2_LC	Level of flash 2	58 % height	Valve B7	0 – 100 %	30	1.32	Direct	Auto

There are two types of control action namely direct and reverse. Direct action means that when the value of the measured variable increases, that of manipulated variables also increases. Meanwhile, in reverse action mode, the value of measured variables decreases resulting in the increase of manipulated value. Auto-mode controllers are straightforward, which means that when there is a difference between manipulated variable and set point, actuator would act to compensate the difference corresponding to the specified control action. All auto controllers (from Figure 32 to Figure 36) in the present model would be described in detail in the next content.
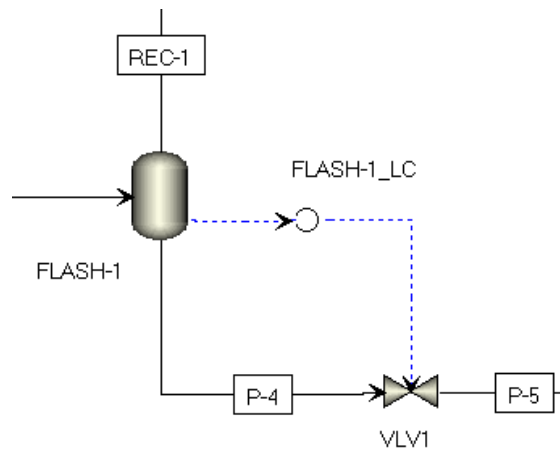
Figure 32. Level control structure of high-pressure separator (FLASH-1) with a controller FLASH-1_LC and a control valve VLV1.

The level of high-pressure separator (FLASH-1) is controlled by a setup including an auto controller (FLASH-1_LC) and a control valve VLV1 as shown in Figure 32. When the level of FLASH-1 (PV – measured variable) is lower than the setpoint of FLASH-1_LC controller, the controller will send a signal to reduce the opening of VLV1 and vice versa to maintain the level of FLASH-1 at desired value (setpoint). The level control structure of low-pressure separator (FLASH-2), which is presented in Figure 33, has the same setup and working principle compared to that of FLASH-1.
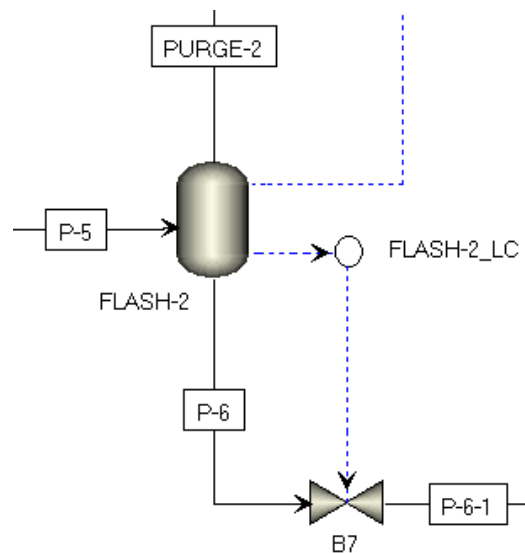

Figure 33. Level control structure of low-pressure separator (FLASH-2) with a controller FLASH-2_LC and a control valve B7.
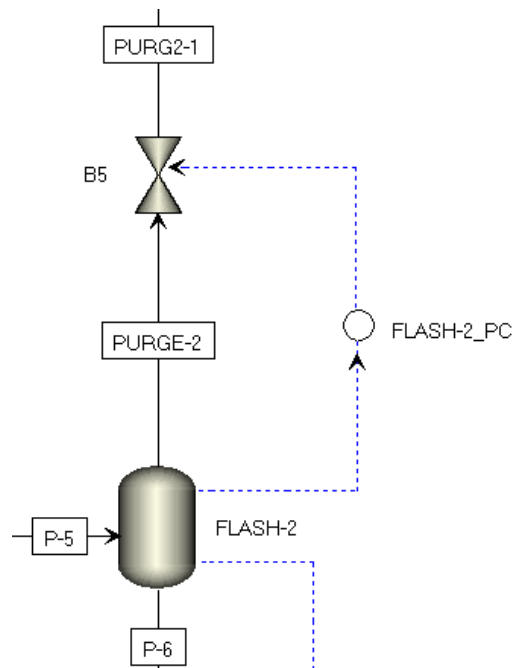
Figure 34. Pressure control structure of low-pressure separator (FLASH-2) with a controller FLASH-2_PC and a control valve B5.

Figure 34 illustrated the control structure for low-pressure separator (FLASH-2) including a controller FLASH-2_PC and a control valve B5. When the pressure of FLASH-2 (PV – measured variable) is higher than the setpoint of FLASH-2_PC controller, the controller will send a signal to increase the opening of B5 and vice versa to maintain the pressure of FLASH-2 at desired value (setpoint).
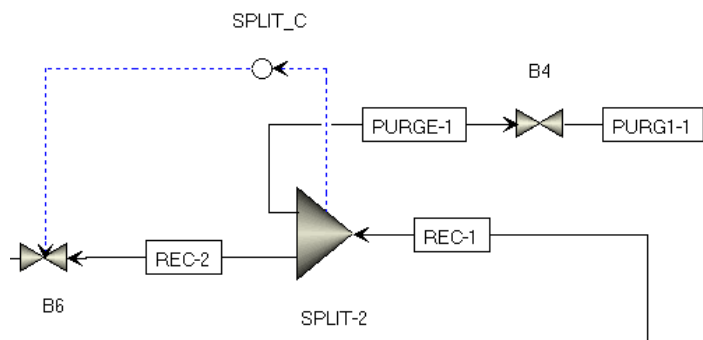

Figure 35. Purging gas (PURGE-1)/recycle gas (REC-1) ratio control structure with a controller SPLIT_C and a control valve B6.

The ratio of purging gas (PURGE-1) to split gas from FLASH-1 (REC-1) is indirectly controlled by the ratio of recycle gas (REC-2) to REC-1 manipulation (Figure 35).

Theoretically, the ratio PURGE-1/REC-1 can be directly controlled by SPLIT_C and valve B4. However, for unknown reason, this setup led to error in Aspen plus dynamics. Therefore, the setup consisting of SPLIT_C and valve B6 was alternatively selected; meanwhile the opening of valve B4 was set at 50 % during process capacity changes. When the ratio REC-2/REC-1 (PV – measured variable) is lower than the setpoint of SPLIT_C controller, the controller will send a signal to increase the opening of valve B6 (reverse action) and vice versa to maintain the ratio at desired value (setpoint).
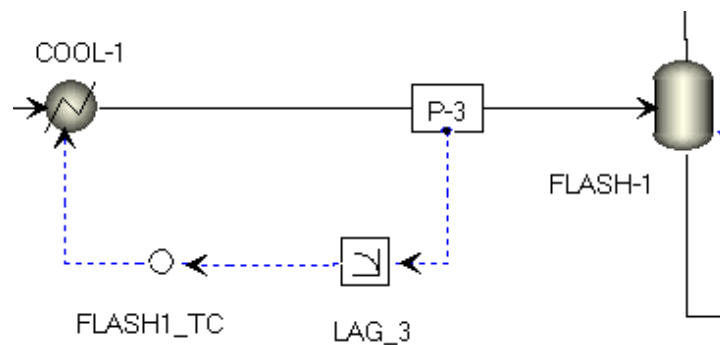

Figure 36. Temperature control structure of inlet FLASH-1 (stream P-3) with a controller FLASH1_TC, a lag block LAG_3 and heat duty of a cooler COOL-1.

The temperature of inlet high-pressure separator (stream P-3) is manipulated by a setup including a controller FLASH1_TC, a lag block LAG_3 and heat duty of a cooler COOL-1 (Figure 36). To be specific, temperature signal of the inlet FLASH-1 is sent to a lag block with time constant = 1 min before being send to FLASH1_TC. When the temperature of stream P-3 (PV – measured variable) is higher than the setpoint of the controller FLASH1_TC, the controller will send a signal to reduce the heat duty of COOL-1 (negative value), or in other words, more cooling medium needs to be supplied to remove the heat from the stream. The application of lag block in temperature control loop results in more unstable control loop (higher fluctuation of COOL-1 heat duty during load changes) but makes a more realistic control. Because it always takes time (thermal lag time) for the heat transfer from the hot stream to cooling medium.

Cascade control loop's working principle are different from auto control loop. In Figure 37, there are 3 control loops namely (1) CO_2 flow rate control with H2_FC controller and valve B1; (2) H_2 flow rate control with CO2_FC controller and valve B2; and (3) H_2/CO_2 ratio control with a multiply block H2/CO2. When the flow rate of H_2 (PV – measured variable)

is lower than the setpoint of H2_FC controller, the controller will send a signal to reduce the opening of valve B1 and vice versa. It is the same working principle for CO_2 flow rate control loop. In the case of ratio H_2/CO_2 control, CO2_FC controller's set point is not a fixed value. To be specific, the present value of H_2 flow rate (PV) would be measured and then be multiplied with a fixed ratio (1/3) between CO_2 and H_2 set in multiply block H2/CO2. This value is a setpoint for the CO2_FC controller and obviously, when the flow rate of H_2 changes, the control loop would calculate the new flow rate of CO_2 satisfying the ratio $H_2/CO_2 = 3/1$.
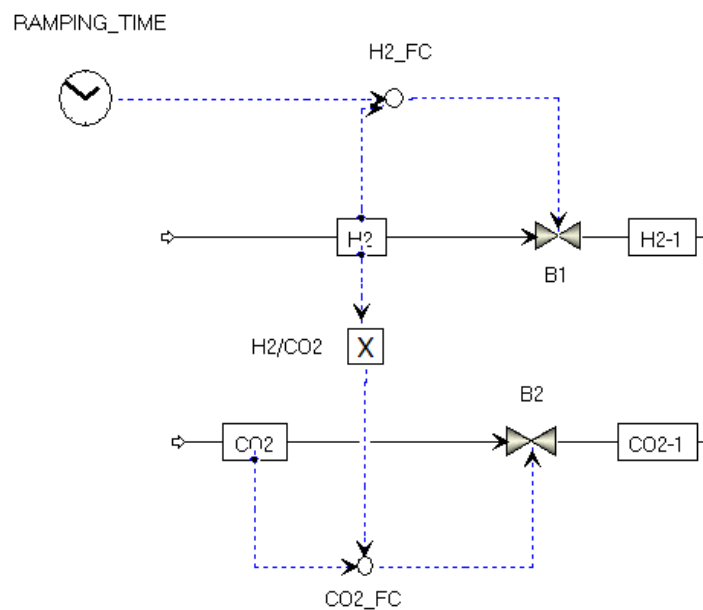

Figure 37. H_2 flow rate control with a H2_FC controller and valve B1(1); CO_2 flow rate control with CO_2_FC controller and valve B2 (2); H_2/CO_2 ratio control with multiply block H2/CO2 (3).

Figure 38 illustrates the cascade temperature control loop of REACTOR including two temperature controllers: primary controller Tin_C and secondary controller Tout_C. The reactor inlet (F-3) temperature (PV – measured variable of Tin_C) is kept at 225 ℃ by manipulating the setpoint of reactor outlet (P-1) temperature (the output of Tin_C) via controller Tin_C. In this control loop, the output of Tin_C is also the "remote" setpoint of Tout_C and the temperature of generated steam (output of Tout_C) is manipulated corresponding to the reactor outlet temperature (PV – measured variable of Tout_C) changes via controller Tout_C. In other words, the reactor inlet temperature is kept at 225 ℃ during load changes by the manipulation of the temperature of generated steam. Notably, with this

configuration, the inlet temperature of the reactor is remained at 225 ℃ and heater ASSIT-1 almost does not need to operate. In practice, there should be a more comprehensive reactor loop, in which liquid water at saturated state enters the shell side of REACTOR and absorbs the released heat to generate saturated steam. However, for the sake of simplicity, only temperature of generated steam is manipulated in the thesis rather than other parameters of real steam streams.
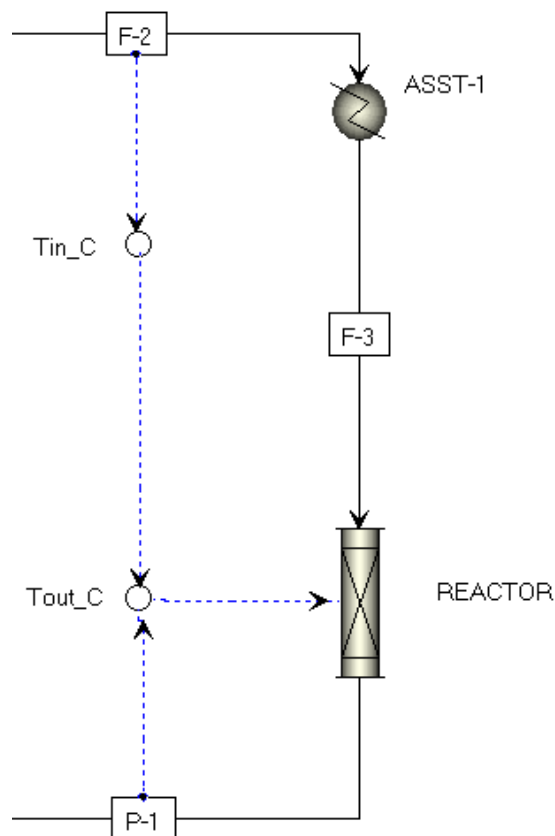

Figure 38. Reactor temperature cascade control loop with primary controllerTin_C and secondary controller Tout_C.

In terms of pressure control, the floating pressure was applied in this model, which means that there is no controller to manipulate the system's pressure. The reason is that when decreasing capacity, the pressure of REACTOR (Figure 31) decreases and the pressure drop in REACTOR, HX1 and HX2 (Figure 31) also decrease leading to the almost unchanged pressure of FLASH-1 (Figure 31) and consequently there is no significant effect on the downstream process. Furthermore, the implementation of pressure control at low loading can result in higher required power of compressors due to pressure decrease and this can

lower the energy efficiency of the process at low loading. Therefore, no pressure control was set into this model.

All controllers in the model are proportional – integral (PI) type and were tuned based on the rule of Tyreus – Luyben (TL) by automatic relay feedback test in Aspen plus dynamics. To be specific, in tune window of each controller, closed loop autotune variation (ATV) mode was selected. Then the output of controller starts to variate within the range of $\pm$ 5 % of the output scale to determine the ultimate gain (K_{CU}) and the ultimate period (P_U) based on discussion and Equation (12) in section 4.2. Finally, tunning parameters (K_C and τ_I) are calculated based on the equations in Table 6 and applied into controllers. However, in the case of SPLIT_C, FLASH-1_LC and FLASH-2_LC (Figure 31) the test following TL rule gives too high gain parameters (P %/%) and the implementation of these parameters in the model can lead to the aggressive controller responses and consequently result in the instability of the model during loading change. Therefore, gain P was achieved by trial-error method, which means that several loading changes are introduced and based on the dynamic responses and the consistency of the model, a reasonable gain P would be selected.

As discussed, the ratio of H_2 to CO_2 is 3/1 and to satisfy this constraint, a multiply block (H2/CO2) (Figure 31) was used to control the flow rate of CO_2 following the change of H_2 flow rate during loading change. On the other hand, in the case of FLASH-1 temperature control (FLASH-1_TC) (Figure 31), there is an implementation of a lag block (LAG_3) (Figure 31) with time constant = 1 minute, whose function is to simulate the lag time of measurement and manipulated variables; thus makes a more realistic dynamic simulation. In fact, lag blocks were applied for Tin_C and Tout_C controllers (Figure 31); however, when variating H_2 feed rate, the model became extremely unstable attributed to the violence fluctuation of SP and PV of both controllers. Therefore, lag blocks were not introduced into temperature control loop of REACTOR (Figure 31). The H_2 data can be imported into RAMPING_TIME block (Figure 31) for ramping time testing.

8 Results and discussions

8.1 Dynamic model verification

In this part, the dynamic model was operated with the same disturbances as presented for the Cui et al. [79] model, which was discussed in section 5. Then, comparison in terms of several parameters such as energy efficiency, ramping rate, and operating conditions at different load changes, etc. was made to assess the validity of the model. Finally, the limits of the model: minimum loading and maximum ramping rate were determined.

There are some notes in this part: (1) The task function in Aspen plus dynamic was used to set ramping time for H_2 flow rate, and the control mode of H2_FC controller (Figure 31) needs to be changed to cascade mode and (2) energy efficiency (η) is calculated following Equation (21)

$$\eta = \frac{\dot{m}_{CRD} \times LHV_{CRD} + \dot{m}_{PURGE1} \times LHV_{PURGE1} + \dot{m}_{PURGE2} \times LHV_{PURGE2} - E_{steam}}{\dot{m}_{H2} \times LHV_{H2} + P_{H2comp} + P_{CO2comp} + P_{REC\ comp}} \quad (21)$$

Where: $\dot{m}$ is the mass flow rate of streams (kg/h)

LHV_i is the lower heating value of gases (MJ/kg)

P_i is the power input for compressors (MJ/h)

E_{steam} is the power of released heat from methanol synthesis reactor (MJ/h)

In the energy efficiency expression in Equation (21), the energy inputs are mainly from H_2 feeding and required energy of compressors. On the other hand, the majority of the energy outputs come from crude methanol, released heat from methanol synthesis reactor for steam generation, and purging gas streams containing H_2 and small amount of CO and methanol, used to generate heat by combustion.

In this section, load changes from 100 to 50 % at the time-on-stream (t) = 1 h with the ramping rate (R) of 50 %/ hour and the loading operation from 50 to 100 % at t = 4 h with the same R were carried out.

The results of the dynamic model during load changes are shown from Figure 39 to Figure 42. In the left side of Figure 39, the flow rate of the outputs: crude methanol (CRD), purging gas 1 (PURGE1) and purging gas 2 (PURGE2) (in Figure 31) agree with the trend of load change (CO_2 and H_2 inputs). There are small undershoots and overshoots at t = 2 and t = 5 for all outputs, which is somehow as similar as Cui et al. [79] data in the right side of Figure 39. In fact, when the capacity decreases, the ratio of purging gas (PURGE1) to recycled stream (REC1) (in Figure 31) decreases and it takes a while for controller SPLIT_C (in Figure 31) to close the valve B6 smaller to maintain the split ratio during the capacity change. That is the reason why there is also a small drop at t = 1 in PURGE1 stream (in Figure 31).

As shown in Figure 40 (left side), when the loading decreases at t = 1, the H_2 concentration in the REACTOR feed (in Figure 31) first increases and then gradually decreases during 50 % loading operation before turning back to normal steady state; meanwhile, the concentration of CO_2 drops at t =1 and grows again during half-loading operation and finally returns to normal value at 100 % loading. However, it is the opposite case in the Cui et al. report, as illustrated in Figure 40 (right side). The reasons may come from the different control setup and parameters, and operating conditions of the two models. At 50 % loading, in the present model, pressure of REACTOR (in Figure 31) decreases ~5 bar from full load mode, whereas there is no pressure decline in the reference model. In addition, temperature of REACTOR inlet (in Figure 31) is maintained at 225 ℃ during loading change by varying the temperature of REACTOR outlet (in Figure 31) (258 ℃ at 100 % loading and 238 ℃ at 50 % loading); meanwhile, the inlet temperature of reactor in the Cui et al. model declines from 240 ℃ at full load mode to 232 ℃ at half-load operation, and the outlet temperature is not controlled. CO concentration in Figure 40 (left side) at 50 % loading is lower than that at full load. This might be attributed to the lower temperature of REACTOR (in Figure 31) at half-load operation (238 ℃), compared to 258 ℃ at full load, and the resulting effect on the water gas-shift reaction. Notably, the temperature of generated steam (the manipulated variable to control the temperature of REACTOR outlet (in Figure 31)) drops from 230 ℃ at 100 % loading to ~222 ℃ at 50 % load, which means that at the lower operating point, the enthalpy of generated steam is lower than that of steam at 100 % loading. The composition at REACTOR inlet (in Figure 31) (especially H_2) needs 8 hours to return to normal steady state starting at t = 5 h. In general, the small changes of component contents in REACTOR

inlet (in Figure 31) do not have a significant impact on the composition of crude methanol (stream P-6-1 in Figure 31) (~48.4 mol-% at 100 % load and ~48.6 mol-% at 50 % load).

Figure 41 presents the change of heat exchanger heat duties and the required power for compressors, in which the left side presents the values for the present model and the right side presents the value for Cui et al. model. Generally, the dynamic responses of HX1 (left side in Figure 31, right side in Figure 18) and COOL1 (in Figure 31) / CL1 (in Figure 18) behave in the same way. Note that the function of the unit HX2 in the two models are different. As illustrated in Figure 41 (left side), when the capacity decreases to 50 % load, the heat duties of HX1, HX2 and COOL1 (in Figure 31) consequently decrease (the duty for COOL1 is a negative value). Due to the floating pressure setup, the required power for compressors is constant as in steady-state model and not shown in Figure 41.

In Figure 42, the energy efficiencies of the process in Figure 31 at ramping rate 50 % /h (left side) in the present model and 50 % per 0.25 h, 0.5 h, 1 h and 2 h in the reference model are presented. On the left side, the efficiency drops from 88.5 % at full-load operation to ~86.75 % at half-load condition. In contrary to the energy efficiency of methanol synthesis part (in Figure 18) in Cui et al. model, the efficiency in the present model drops during capacity decrease, which is mainly attributed to the unchanged power of compressors at the low operating point. However, in general, the energy efficiency of methanol synthesis process in two models during the 50 % load change remains over 85 %. On the other hand, during the ramping period, both models show fluctuation at different levels corresponding to different ramping rates. The higher the ramping rate, the more fluctuation is found in the energy efficiency.
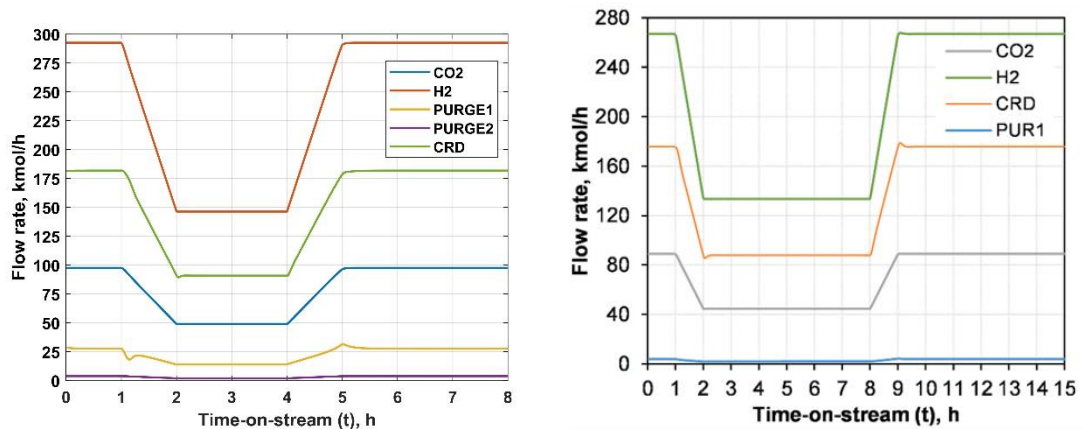
Figure 39. The comparison between the flow rate of inputs and outputs in thesis: flow rate of CO2 (stream CO2), H2 (stream H2), PURGE1 (stream PURGE-1-1), PURGE2 (stream PURGE-2-1), CRD (stream P-6-1) referring to Figure 31 (left) and flow rate of stream CO2, H2, CRD and PUR1 referring to Figure 18 in Cui et al. article [79] (right).
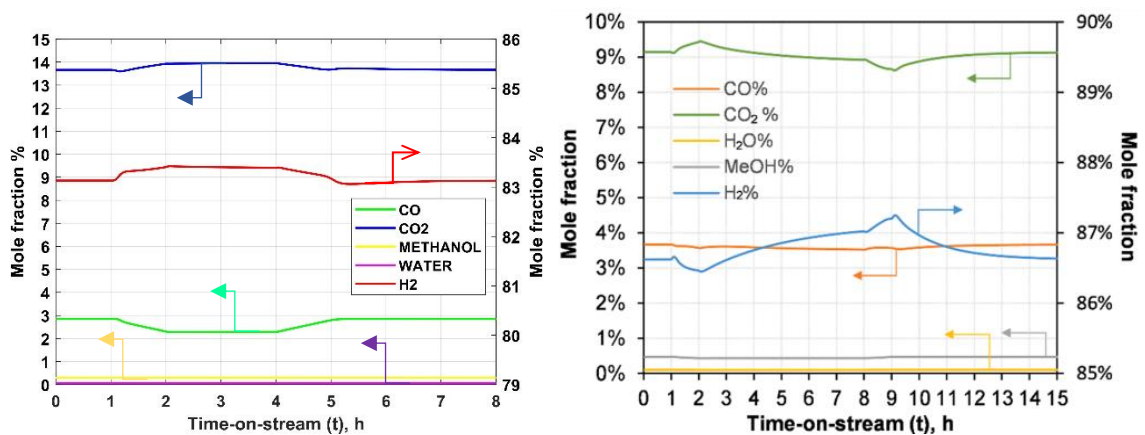

Figure 40. The comparison between the inlet composition of methanol synthesis reactor (REACTOR in Figure 31) in thesis (left) and methanol synthesis reactor (R1 in Figure 18) in Cui et al. article [79] (right).
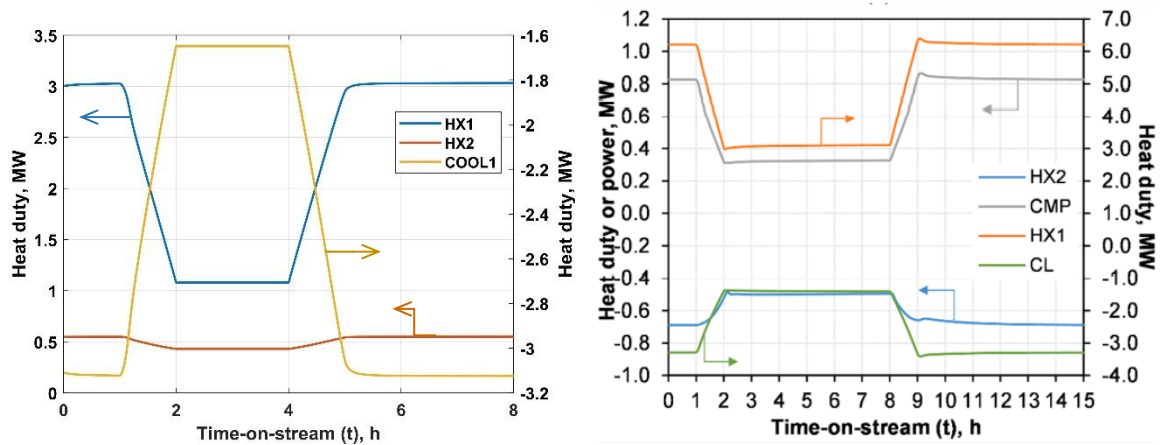
Figure 41. The comparison between the heat duties of heat exchangers (HX1, HX2 in Figure 31), cooler (COOL-1 in Figure 31) in thesis (left) and the heat duties of (HX1, HX2 in Figure 18), cooler (CL in Figure 18) in Cui et al. article [79] (right).
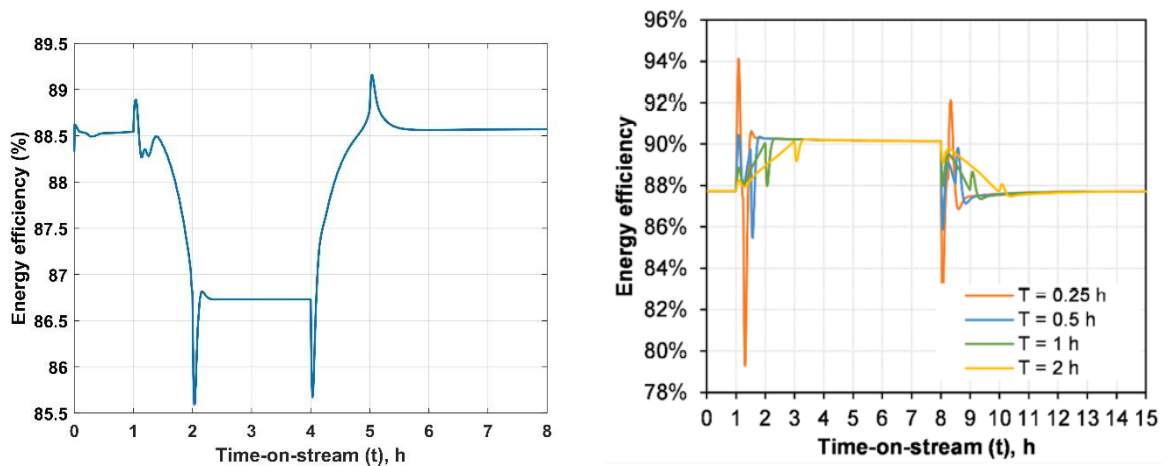

Figure 42. The comparison between the energy efficiency of methanol synthesis process in Figure 31 during disturbance with R = 50 %/h in thesis (left) and the energy efficiency of the same process in Figure 18 with R = 50 % per 0.25 h, 0.5 h, 1 h and 2 h in Cui et al. article [79] (right).

8.2 Model limits

The continuing part is related to determination of minimum and maximum ramping rates. At low-load operation, the model is more sensitive: the computer time to run the simulation is longer and too high a ramping rate can lead to an error in the integrator. Therefore, manual testing was used to determine the minimum loading. To be specific, the flow rate of H_2 was gradually decreased and during the modification (at low load), the response of the model

was monitored. For example, if the computation time is found to increase, then the ramping rate for next step would be decreased. Finally, as shown in Figure 44 (a), the model can handle the H_2 flow rate of 55 kmol/h, corresponding to 18.8% load. Notably, when H_2 flow rate is lower than 55 kmol/h, there is a notification about in integrator fail, which means that the error can come either from a numerical limitation of Aspen plus dynamics, or from the hard limit of the process.

However, the heat duty of HX1 (in Figure 31) is below zero starting at t ~2.5 hours (corresponding to ~24.6 % load) without any error notification from Aspen plus dynamics, which means that the temperature of the cold outlet stream is higher than the temperature of hot inlet stream. Therefore, the flow rate of H_2 should be higher than 72 kmol/h (24.6 % load) to ensure logical operation. Even in that case, the size of HX1 (in Figure 31) is extremely large due to a small temperature approach (~0.46 ℃). At 50 % load, the temperature approach of HX1 (in Figure 31) is 12.5 ℃. Therefore, the minimum load selection depends on the selection of heat exchangers type, the cost of equipment or even modification of REACTOR (in Figure 31) temperature control loop. In future studies, a more comprehensive steam generator system from methanol synthesis reactor as shown in Figure 43 should be probably applied for more detailed and accurate assessment. In Figure 43, cooling water is fed into the shell side of multitubular fixed-bed reactor to generate steam by the released heat from methanol synthesis reactions. Generated steam then turns back into the top of the steam drum. The pressure of generated steam in shell side of the reactor is controlled by the steam drum pressure [100].
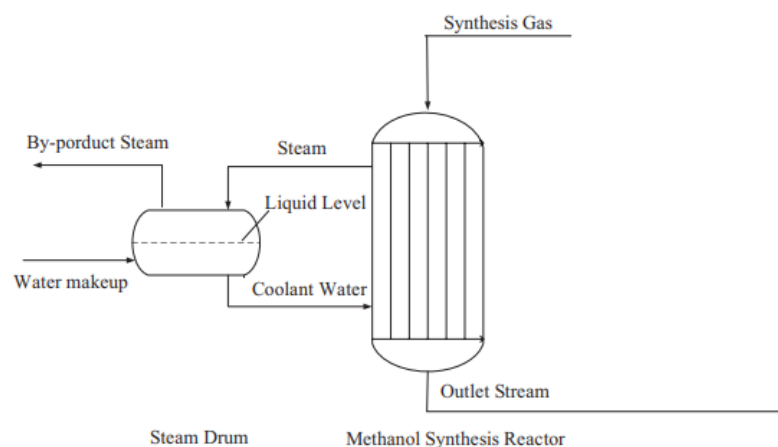

Figure 43. A schematic of Lurgi methanol synthesis reactor in industry [100].
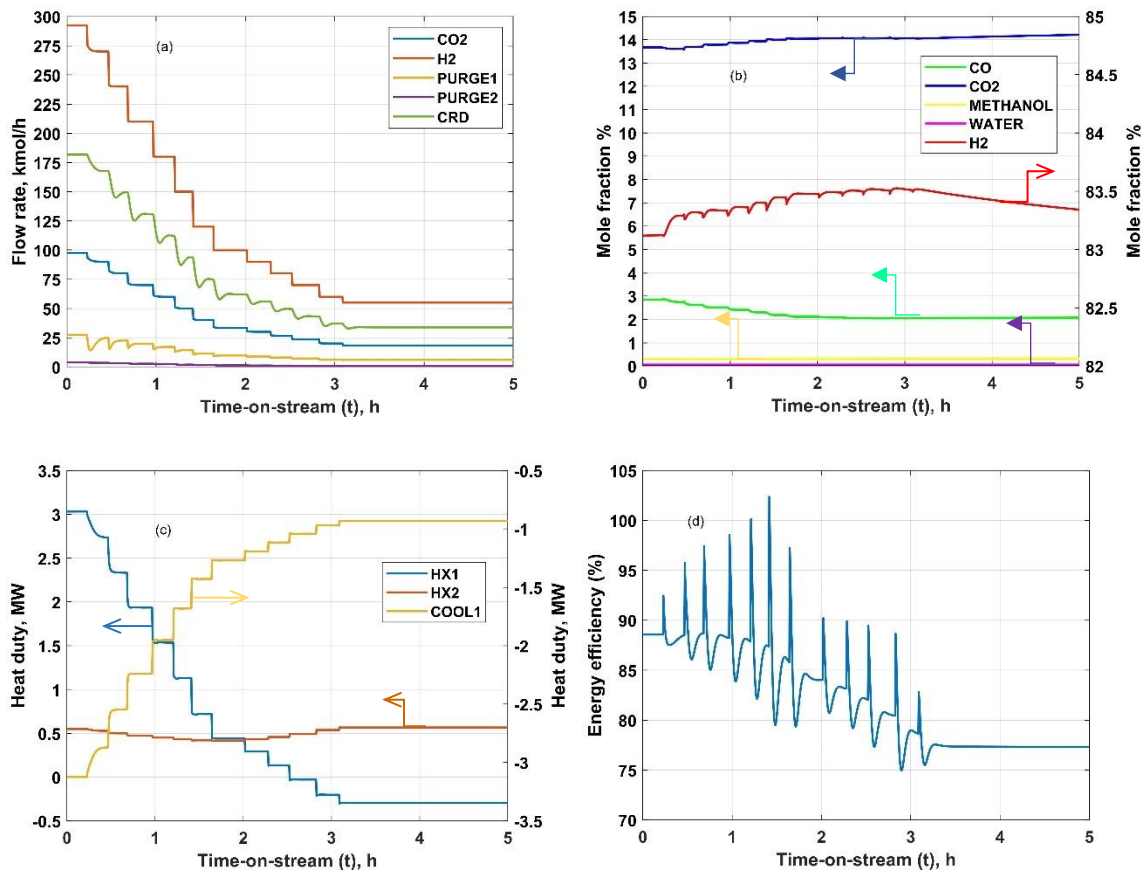
Figure 44. Flow rate of CO2 (stream CO2), H2 (stream H2), PURGE1 (stream PURGE-1-1), PURGE2 (stream PURGE-2-1), CRD (stream P-6-1) referring to Figure 31 (a), the inlet composition of methanol synthesis reactor (REACTOR in Figure 31) (b), the heat duties of heat exchangers (HX1, HX2) and cooler (COOL-1) in Figure 31 (c), and the energy efficiency of methanol synthesis process in Figure 31 (d) during manual load change from 100 % to minimum limit.

Finally, a series of disturbance tests (between 100 % and 50 % load) at different ramping rates: (1) 50 % change per 0.5 hours, (2) 50 % change per 0.25 hours and (between 100 % and 46.7 % load) at ramping rate (3) 53.3 % change per 0.125 hours were carried out to determine the highest possible ramping rate of the present model. As illustrated from Figure 45 to Figure 47, the model can handle the highest ramping rate R = 53.3 % change per 0.125 hours. A higher rate led to the model crash due to integrator fault. Similarly, to the previous part, further and more comprehensive research should be carried out to determine what the cause for the ramping rate limitation is. Based on the energy efficiency at different ramping rates (right side of Figure 45 to Figure 47), it can be concluded that the higher the rate, the more violent fluctuation of energy efficiency is generated. In the Cui et al. article [79], there is no data about the ramping rate R = 53.3 % change per 0.125 hours. However, even though

the model in the article cannot handle this high rate, it is understandable because the model in the article has realistic setup with more constraints with the specified of capacitance of heat exchangers and the reactor.

Figure 45. Flow rate of CO2 (stream CO2), H2 (stream H2), PURGE1 (stream PURGE-1-1), PURGE2 (stream PURGE-2-1), CRD (stream P-6-1) referring to Figure 31 (left) and the energy efficiency of methanol synthesis process in Figure 31 (right) at ramping rate R = 50 % change per 0.5 hours.

Figure 46. Flow rate of CO2 (stream CO2), H2 (stream H2), PURGE1 (stream PURGE-1-1), PURGE2 (stream PURGE-2-1), CRD (stream P-6-1) referring to Figure 31 (left) and the energy efficiency of methanol synthesis process in Figure 31 (right) at ramping rate R = 50 % change per 0.25 hours.
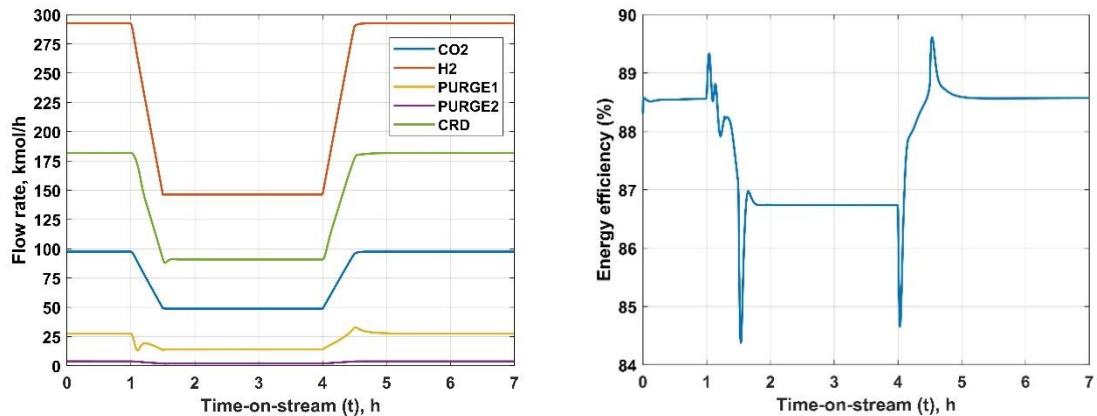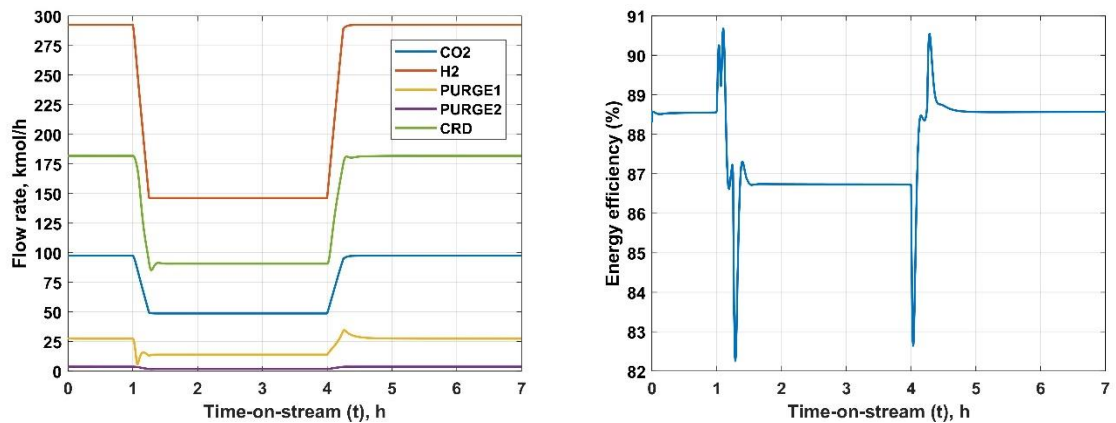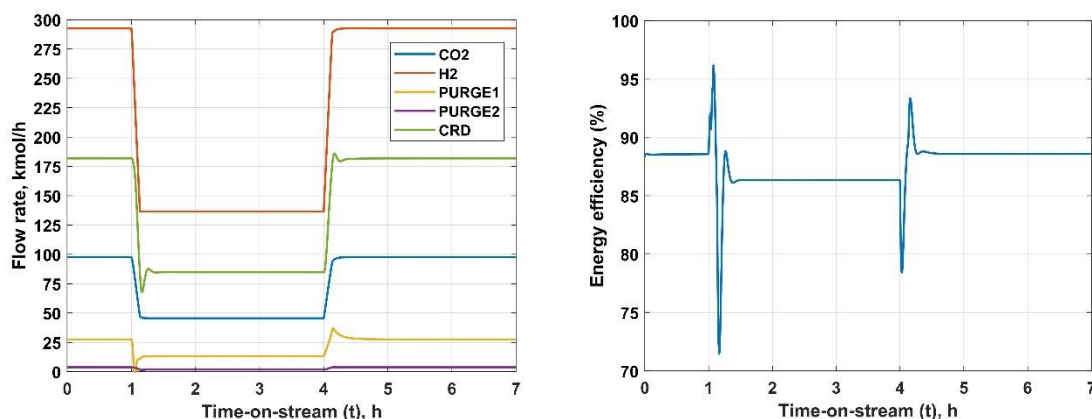
Figure 47. Flow rate of CO2 (stream CO2), H2 (stream H2), PURGE1 (stream PURGE-1-1), PURGE2 (stream PURGE-2-1), CRD (stream P-6-1) referring to Figure 31 (left) and the energy efficiency of methanol synthesis process in Figure 31 (right) at ramping rate R = 53.3 % change per 0.125 hours.

8.3 Real-time H_2 data application

As discussed in the literature part, the main characteristic of renewable electricity (wind-based, solar-based) is the intermittency. Therefore, application of real-time data of RES electricity into water electrolysis for H_2 production should be carried out to investigate a more realistic dynamic scenario. Due to lack information of H_2 generation from wind electricity, data of H_2 production from solar-based electricity based on the research of Sakas et al. [101], was alternatively selected in this thesis. In Figure 48, the molar flow of H_2, which was recalculated suitably with the present capacity (292.5 kmol h^{-1} at full-load mode) based on the mass of generated H_2 (kg) per 5 minutes over a year [101], is presented. According to Figure 48, 22.7 % load to full load condition is the main operational range. The transformation from mass to H_2 flow rate at a suitable scale for this thesis (full load at 292.5 kmol/h of H_2) is shown in Appendix 2. Notably, based on the mass of generated H_2 per 5 minutes from Sakas et al. [101] data, the flow rate of H_2 (kg min^{-1}) can be calculated and this value can be subsequently converted into molar flow rate of H_2 at suitable production scale.
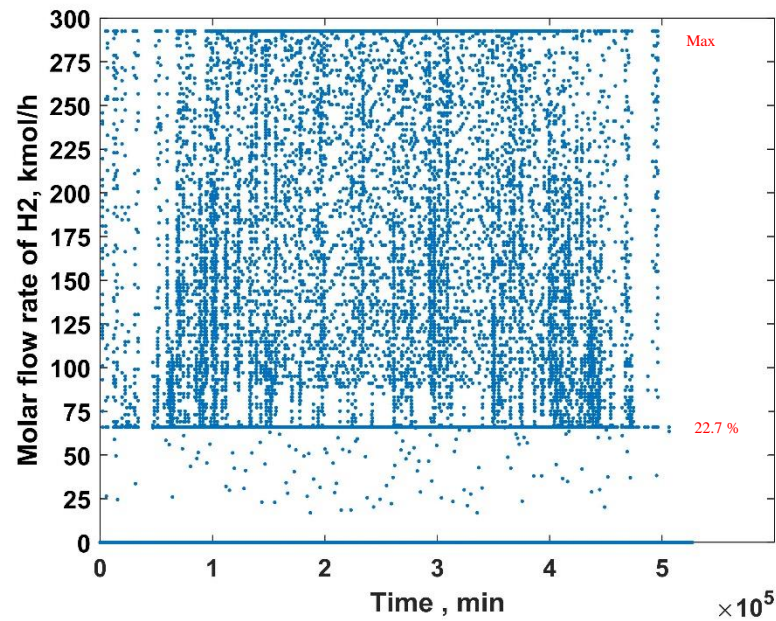
Figure 48. Molar flow rate of H₂ with modified capacity following the value of present model (292.5 kmol h-1 at 100 % load) based on the mass of H₂ production from solar-based electricity by alkaline electrolyzer [101].

As discussed in the previous section, H₂ flow rate should be above 72 kmol/h (~24.6 % load) for feasible operation of HX1 (in Figure 31) with positive value of temperature approach. Therefore, a part of the generated H₂ data from Figure 48 (within 3 operating hours) with the range from 91 kmol/h to 292.5 kmol/h was imported to RAMPING_TIME block (in Figure 31) from t = 1 to t = 4 to evaluate the dynamic responses in practical conditions.

As shown in Figure 49, the flow rate of outputs (CRD, PURGE1, PURGE2 in Figure 31) can follow up the load change of H₂ even in the severe condition (t = 1.5 h, decreasing 50 % within ~0.09 h) and the model can still handle the continuous fluctuation of H₂. Note that to simulate the model with the ramping rate of 50 % within ~0.09 h, which is higher than the highest ramping rate discussed in section 8.1, the model spent extremely long computer time (more than 30 minutes computer time to simulate 0.005 hours of process time) and there were several model faults during the trial. The composition of components at REACTOR inlet (in Figure 31), and heat duties of heat exchangers, cooler (HX1, HX2 and COOL-1 in Figure 31) also show a good agreement in terms of dynamic characteristics compared to the values in load change testing in the previous section. The efficiency shows a wide range of fluctuation (~69 % to ~100 %) at around t = 1.5 h. This is attributed to the lag time between

the flow rate of CRD (stream P-6-1) and H_2 in Figure 31. To decrease the lag time, higher gain parameter (P %/%) of FLASH-1_LC and FLASH-2_LC (in Figure 31) needs to be applied (P increases from 30 %/% to 40 %/% for both controllers). As clearly presented in Figure 50 (b), higher gain P (40 %/%) leads to a less fluctuation of energy efficiency (~73 % - 97 % compared to ~69 % - ~100 % with P = 30 %/%). In Figure 50, the energy efficiency is found to more closely follow the variation in the crude methanol and hydrogen flow rates. However, it is a trade-off between the intermittency energy efficiency and the speed of the integrator. To be specific, low intermittent efficiency translates into long computational times.
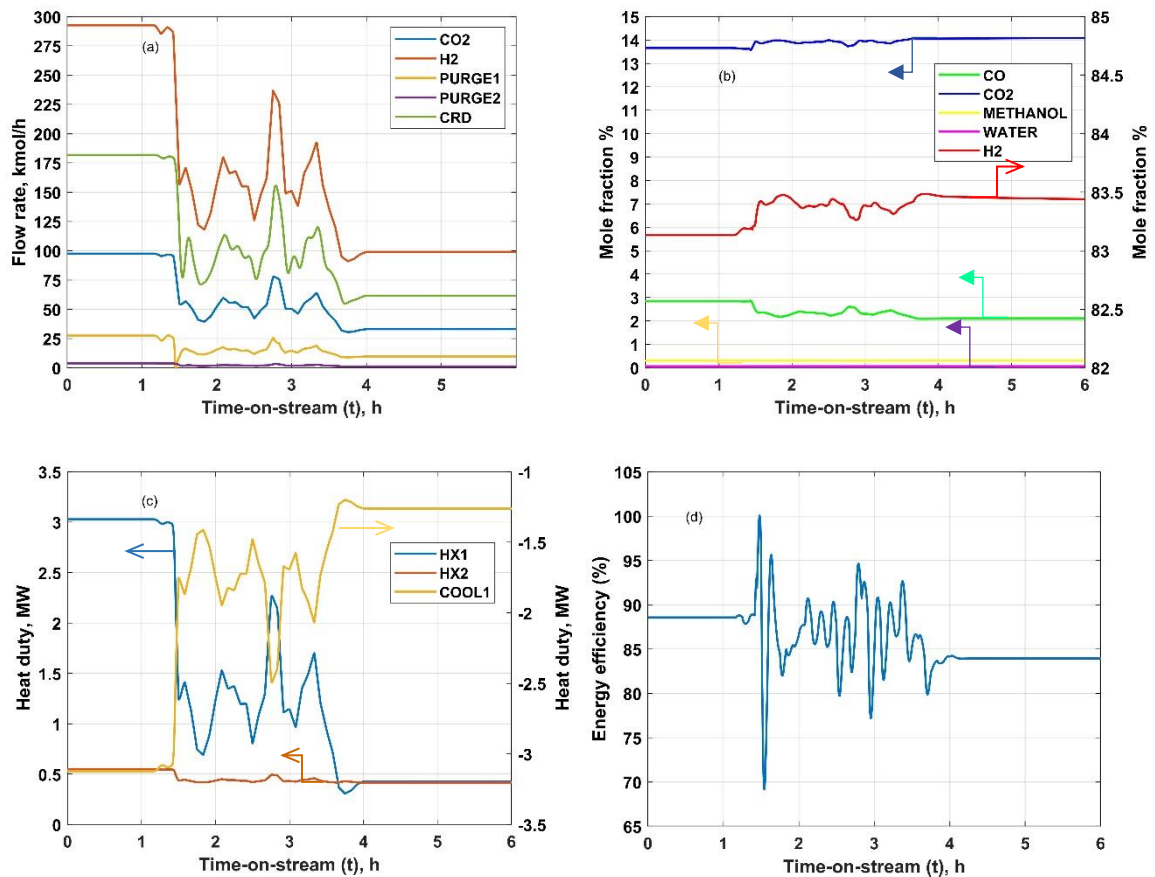

Figure 49. (a) Flow rate of CO2 (stream CO2), H2 (stream H2), PURGE1 (stream PURGE-1-1), PURGE2 (stream PURGE-2-1), CRD (stream P-6-1) referring to Figure 31, (b) composition of REACTOR inlet , (c) heat duties of HX1, HX2 and COOL-1 referring to Figure 31 and (d) energy efficiency with a part of H_2 data (in Figure 48) application.
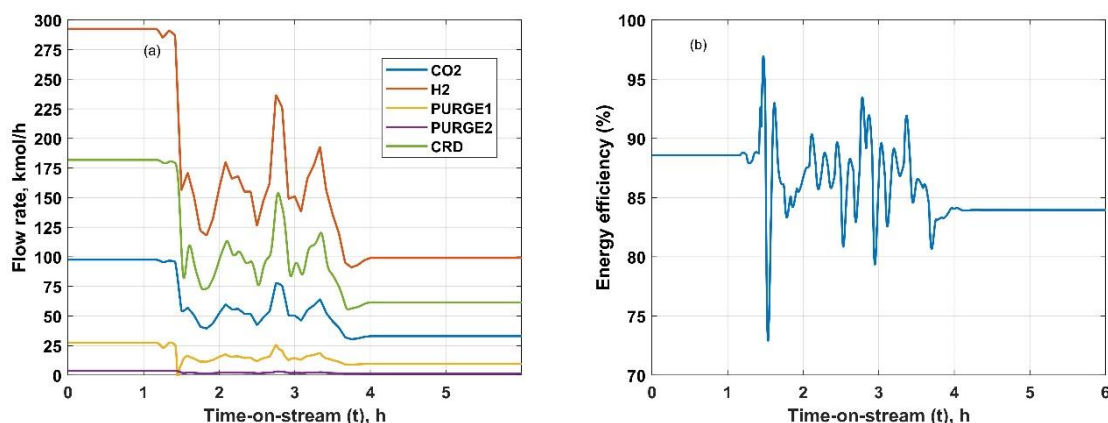
Figure 50. Flow rate of CO2 (stream CO2), H2 (stream H2), PURGE1 (stream PURGE-1-1), PURGE2 (stream PURGE-2-1), CRD (stream P-6-1) referring to Figure 31 (a) and energy efficiency (b) with higher gain parameters P 40%/% compared to 30 %/% of flash level controllers (FLASH-1_LC and FLASH-2_LC in Figure 31) with a part of H_2 data (in Figure 48) application.

On the other hand, there is another big concern about the operating ability of the model with full application of real-time electrolytic H_2 data. In fact, it is obvious that there are many periods that no H_2 is produced due to the running out of solar electricity (Figure 48), leading to the model invalidity. Besides the implementation of batteries or grid electricity to maintain the model operation at minimum loading, introduction of a H_2 buffer tank can be seen as a potential alternative. H_2 tank can act as a dampener helping to reduce the fluctuation of H_2 input into methanol synthesis process. When there is no H_2 production or the decrease rate of H_2 input is too high, the tank can supply a certain amount of H_2 to satisfy the minimum loading or the reasonable decreasing rate. Meanwhile, when the feeding rate of H_2 is too high, H_2 can be collected into the tank to reduce to suitable rate.

9 Conclusions

Power-to-methanol, in which green methanol is produced based on renewable electricity (wind- or solar-based,) and captured CO_2, can be seen as a potential technology in terms of CO_2 emission reduction and excess renewable power utilization. Deep understanding of the

dynamic characteristics of the power-to-methanol process is crucial due to the intermittency of renewable electricity. A dynamic model of crude methanol synthesis corresponding to a scale of ~25000 t methanol per year was built in Aspen plus dynamics to investigate: (1) dynamic responses of the process and energy analysis, (2) minimum load and ramping rate limitations and (3) the model performance with implementation of real-time H_2 production data.

A comparison between the present model and a reference model from Cui et al. [79] was made. The results show that during the load change from 100 % to 50 % capacity at the ramping rate of 50 %/hour, the flow rate of outputs and heat duties of heat exchangers and cooler in Figure 31 can follow up and agree with the trend of loading changes, similarly to the reference model in Figure 18. There are opposite CO_2 and H_2 trends in the case of components' composition of REACTOR inlet (in Figure 31) due to the different operating and control parameters and reactor configuration. According to the present model, the energy efficiency slightly decreases, from ~88.5 % at full load to ~86.75 % at half-load, which is contrary to the results of the reference model. This is attributed to the different pressure and temperature control structure of the two models.

According to the results from Aspen plus dynamics, the minimum load of the model is 18.8 % from the maximum capacity. However, this operation point leads to an unfeasible condition – negative duty of HX1 (reactor preheater) (in Figure 31). Therefore, the model should be operated at a capacity not lower than 24.6 % from maximum loading. A series of different ramping rates were investigated for load changes from 100 % to 50 % (0.5 hours, 0.25 hours) and from 100 % to 46.7 % (0.125 hours). The highest rate that the model can handle was found to be the change ~7.1 %/min.

A real-time dataset H_2 flow rate from solar electricity was used in simulations. Data of H_2 flow rate in the range from 91 kmol/h to 292.5 kmol/h during three hours of operation was extracted and implemented into the model. The results pointed out that the model can handle during the continuing disturbance even under severe ramping condition (50 % loading decrease within ~0.09 h). To achieve the validity for full implementation of real-time H_2 data including multiple periods with no H_2 production and severe ramping rates, a H_2 buffer tank should be sized and introduced into the model and probably actual process for "smoother" operating.

REFERENCES

[1] Our World in Data. Our World in Data. Atmospheric concentrations. 2022; Available at: https://ourworldindata.org/atmospheric-concentrations#how-have-global-co2-concentrations-changed-over-time.

[2] Adoption of the paris agreement. United Nations Framework Convention on Climate Change, Paris; 2015.

[3] IEA. IEA – International Energy Agency. 2022; Available at: https://www.iea.org/data-and-statistics/data-browser?country=WORLD&fuel=CO2%20emissions&indicator=CO2BySector.

[4] Zappa, Junginger, van den Broek. Is a 100% renewable European power system feasible by 2050? Applied energy 2019 Jan 01,;233-234:1027-50.

[5] Ince AC, Colpan CO, Hagen A, Serincan MF. Modeling and simulation of Power-to-X systems: A review. Fuel (Guildford) 2021 Nov 15,;304:121354.

[6] Stančin H, Mikulčić H, Wang X, Duić N. A review on alternative fuels in future energy system. Renewable & sustainable energy reviews 2020 Aug;128:109927.

[7] Chehade Z, Mansilla C, Lucchese P, Hilliard S, Proost J. Review and analysis of demonstration projects on power-to-X pathways in the world. International journal of hydrogen energy 2019 Oct 22,;44(51):27637-55.

[8] Hashimoto K. Metastable metals for "green" materials for global atmosphere conservation and abundant energy supply. Materials science & engineering. A, Structural materials : properties, microstructure and processing 1994;179:27-30.

[9] Candelaresi D, Spazzafumo G. 5 - Power to methanol. Power to Fuel: Elsevier Inc; 2021, p. 103-122.

[10] Hanif MA, Nadeem F, Tariq R, Rashid U. Chapter 10 - Hydrogen and fuel cells. In: Hanif MA, Nadeem F, Tariq R, Rashid U, editors. Renewable and Alternative Energy Resources: Academic Press; 2022, p. 605-657.

[11] Candelaresi D, Spazzafumo G. 1 - Introduction: the power-to-fuel concept. In: Spazzafumo G, editor. Power to Fuel: Academic Press; 2021, p. 1-15.

[12] Kober, Bauer, Bach, Beuse, Georges, Held, et al. Perspectives of Power-to-X technologies in Switzerland: A White Paper. 2019;.

[13] Daiyan, Macgill, Amal. Opportunities and Challenges for Renewable Power-to-X. ACS Energy Lett. 2020;5:3843.

[14] Candelaresi D, Spazzafumo G. 5 - Power to methanol. In: Spazzafumo G, editor. Power to Fuel: Academic Press; 2021, p. 103-122.

[15] Plass L, Bertau M, Linicus M, Heyde R, Weingart E. Methanol as a Hydrogen and Energy Carrier. Methanol: The Basic Chemical and Energy Feedstock of the FutureBerlin, Heidelberg: Springer Berlin Heidelberg; 2014, p. 619-655.

[16] Offermanns H, Schulz K, Brandes E, Schendler T. Substance Properties of Methanol. Methanol: The Basic Chemical and Energy Feedstock of the FutureBerlin, Heidelberg: Springer Berlin Heidelberg; 2014, p. 303-325.

[17] International Energy Agency. IEA-AMF. 2022; Available at: https://iea-amf.org/content/fuel_information/methanol.

[18] International Renewable Energy Agency AD. IRENA. 2022; Available at: https://www.irena.org/-/media/Files/IRENA/Agency/Publication/2021/Jan/IRENA_Innovation_Renewable_Methanol_2021.pdf.

[19] Turner JWG, Pearson RJ, McGregor MA, Ramsay JM, Dekker E, Iosefa B, et al. GEM Ternary Blends: Testing Iso-Stoichiometric Mixtures of Gasoline, Ethanol and Methanol in a Production Flex-Fuel Vehicle Fitted with a Physical Alcohol Sensor. 2012;.

[20] E. Bjorck, D. Dobson, Pandhal. Biotechnological conversion of methane to methanol: evaluation of progress and potential. AIMS Bioengineering 2018;5(1):1-38.

[21] Methanol market services Asia. Methanol institute. 2022; Available at: https://www.methanol.org/methanol-price-supply-demand/.

[22] Fiedler, Gronemann, Kersebohm, Weiss, Witte, Kersebohm, et al. Methanol. Weinheim, Germany: Wiley-VCH Verlag GmbH & Co. KGaA; 2000.

[23] Chakraborty JP, Singh S, Maity SK. Chapter 6 - Advances in the conversion of methanol to gasoline. In: Maity SK, Gayen K, Bhowmick TK, editors. Hydrocarbon Biorefinery: Elsevier; 2022, p. 177-200.

[24] ExxonMobil. ExxonMobil Chemical . 2022; Available at: https://www.exxonmobilchemical.com/en/catalysts-and-technology-licensing/synthetic-fuels.

[25] Nesterenko N, Aguilhon J, Bodart P, Minoux D, Dath J-. Chapter 5 - Methanol to Olefins: An Insight Into Reaction Pathways and Products Formation. In: Sels BF, Kustov LM, editors. Zeolites and Zeolite-Like MaterialsAmsterdam: Elsevier; 2016, p. 189-263.

[26] Gogate MR. Methanol-to-olefins process technology: current status and future prospects. Petroleum science and technology 2019 Mar 4,;37(5):559-65.

[27] Ei-Zeftawy AM. Focus on the Chemical Value of Methanol. Journal of King Saud University - Engineering Sciences 1995;7:209.

[28] Senatore, Gordano, Basile, Dalena, Marino, Basile. Methanol Production and Applications: An Overview. : Elsevier; 2018.

[29] U.S. EIA: International Energy Outlook 2021 With projections to 2050 – Summary: U.S. Energy Information Administration. VGB PowerTech (Essen, Germany : 2001) 2021 Jan 1,(11):1.

[30] Hannah Ritchie and Max Roser. Our World in Data. 2022; Available at: https://ourworldindata.org/electricity-mix.

[31] Luo Y, Shi Y, Cai N. Chapter 1 - Introduction. In: Luo Y, Shi Y, Cai N, editors. Hybrid Systems and Multi-energy Networks for the Future Energy Internet: Academic Press; 2021, p. 1-7.

[32] Luc Pelkmans, Lassi Similä, Elina Mäki. Implementation of bioenergy in Finland – 2021 update. 2021;.

[33] Sovacool. The intermittency of wind, solar, and renewable electricity generators: Technical barrier or rhetorical excuse? Utilities policy 2009;17(3):288-96.

[34] Asiaban, Kayedpour, Samani, Bozalakov, De Kooning, Crevecoeur, et al. Wind and Solar Intermittency and the Associated Integration Challenges: A Comprehensive Review Including the Status in the Belgian Power System. Energies (Basel) 2021 May 04,;14(9):2630.

[35] Kabir E, Kumar P, Kumar S, Adelodun AA, Kim K. Solar energy: Potential and future prospects. Renewable and Sustainable Energy Reviews 2018;82:894-900.

[36] Tester JW. Sustainable energy. 2. ed. ed. Cambridge, Mass. [u.a.]: MIT Press; 2012.

[37] Our World in Data. Our World in Data. 2022; Available at: https://ourworldindata.org/grapher/share-electricity-solar?tab=chart&time=2005..latest.

[38] Our World in Data. Our World in Data. 2022; Available at: https://ourworldindata.org/explorers/energy?tab=chart&time=2000..latest&facet=none&country=USA~GBR~CHN~OWID_WRL~IND&Total+or+Breakdown=Select+a+source&Select+a+source=Solar&Energy+or+Electricity=Electricity+only&Metric=Annual+generation.

[39] International Renewable Energy Agency. International Renewable Energy Agency. 2022; .

[40] National Renewable Energy Laboratory. SolarPACES . 2022; Available at: https://www.solarpaces.org/csp-technologies/csp-projects-around-the-world/.

[41] Our World in Data. Our World in Data. 2022; Available at: https://ourworldindata.org/grapher/solar-pv-cumulative-capacity?time=2005..latest&country=OWID_WRL~CHN~USA~IND~GBR.

[42] PV Magazine. PV Magazine. 2022; Available at: https://www.pv-magazine.com/2021/09/09/the-worlds-largest-solar-power-plants/.

[43] Aziz Nickleson. Solar Feeds. 2022; Available at: https://www.solarfeeds.com/mag/biggest-solar-projects-farms-in-finland/.

[44] Atria. Atria. 2022; Available at: https://www.atria.fi/en/group/company/history/years-of-atria/2018/atria-solar-power-park-completed/.

[45] yle. yle. 2022; Available at: https://yle.fi/news/3-12467303.

[46] Mika Laatikainen, Jyri Ruotsalainen. Fingrid. 2022; Available at: https://www.fingrid.fi/en/electricity-market-information/solar-power/.

[47] Belyakov. Wind energy. Sustainable Power Generation 2019;:397.

[48] Our World in Data. Our World in Data. 2022; Available at: https://ourworldindata.org/renewable-energy.

[49] International Renewable Energy Agency. IREA. 2022; Available at: https://www.irena.org/wind.

[50] JENN CRANNEY. NorthWest Renewable Energy Institute. 2022; Available at: https://www.nw-rei.com/2021/08/20/worlds-largest-wind-farms/.

[51] Finnish wind power association. Finnish wind power association (FWPA). 2022; Available at: https://tuulivoimayhdistys.fi/media/tuulivoima_vuositilastot_first_half_2022_in_english-1.pdf.

[52] Finnish Wind Power Association. Finnish Wind Power Association (FWPA). 2022; Available at: https://tuulivoimayhdistys.fi/en/wind-power-in-finland/wind-power-in-production-and-dismantled.

[53] yle. yle. 2022; Available at: https://yle.fi/news/3-12196240.

[54] Finnish Wind Power Association. Finnish Wind Power Association (FWPA). 2022; Available at: https://tuulivoimayhdistys.fi/en/wind-power-in-finland/projects-under-construction.

[55] Fingrid. Fingrid. 2022; Available at: https://www.fingrid.fi/en/electricity-market-information/wind-power-generation/.

[56] Shi J, Erdem E. Chapter 3 - Estimation of Wind Energy Potential and Prediction of Wind Power. In: Letcher TM, editor. Wind Energy Engineering: Academic Press; 2017, p. 25-49.

[57] Asiaban, Kayedpour, Samani, Bozalakov, De Kooning, Crevecoeur, et al. Wind and Solar Intermittency and the Associated Integration Challenges: A Comprehensive Review

Including the Status in the Belgian Power System. Energies (Basel) 2021 May 04,;14(9):2630.

[58] Rosas PAC. Dynamic Influences of Wind Power on The Power System. 2004;.

[59] Mills A. Implications of Wide-Area Geographic Diversity for Short- Term Variability of Solar Power. 2010 Aug 23,.

[60] Luo Y, Shi Y, Cai N. Chapter 2 - Distributed hybrid system and prospect of the future Energy Internet. In: Luo Y, Shi Y, Cai N, editors. Hybrid Systems and Multi-energy Networks for the Future Energy Internet: Academic Press; 2021, p. 9-39.

[61] Belyakov N. Chapter Twenty-Three - Sustainable electricity management beyond generation. In: Belyakov N, editor. Sustainable Power Generation: Academic Press; 2019, p. 539-563.

[62] Buffo, Marocco, Ferrero, Lanzini, Santarelli. Chapter 15 - Power-to-X and power-to-power routes. Solar Hydrogen Production: Elsevier Inc; 2019, p. 529-557.

[63] Tichler R, Bauer S. Chapter 18 - Power-to-Gas. In: Letcher TM, editor. Storing EnergyOxford: Elsevier; 2016, p. 373-389.

[64] Rego de Vasconcelos, Lavoie. Recent Advances in Power-to-X Technology for the Production of Fuels and Chemicals. Frontiers in Chemistry 2019;7:392.

[65] Burre J, Bongartz D, Brée L, Roh K, Mitsos A. Power-to-X: Between Electricity Storage, e-Production, and Demand Side Management. Chemie ingenieur technik 2020 Jan;92(1-2):74-84.

[66] Keçebaş, Kayfeci, Bayat. Chapter 9 - Electrochemical hydrogen generation. Solar Hydrogen Production: Elsevier Inc; 2019, p. 299-317.

[67] Obodo KO, Ouma CNM, Bessarabov D. 2 - Low-temperature water electrolysis. In: Spazzafumo G, editor. Power to Fuel: Academic Press; 2021, p. 17-50.

[68] Xu H, Ni M. 3 - High-temperature electrolysis and co-electrolysis. In: Spazzafumo G, editor. Power to Fuel: Academic Press; 2021, p. 51-73.

[69] Blug M, Leker J, Plass L, Günther A. Methanol Generation Economics. Methanol: The Basic Chemical and Energy Feedstock of the FutureBerlin, Heidelberg: Springer Berlin Heidelberg; 2014, p. 603-618.

[70] Dieterich, Buttler, Hanel, Spliethoff, Fendt. Power-to-liquid via synthesis of methanol, DME or Fischer–Tropsch-fuels: a review. Energy & environmental science 2020 Oct 14,;13(10):3207-52.

[71] Fiedler E, Gronemann V, Kersebohm DB, Weiss G, Witte C, Kersebohm DB, et al. Methanol. Weinheim, Germany: Wiley-VCH Verlag GmbH & Co. KGaA; 2000.

[72] Ruocco C, Ricca A, Meloni E, Palma V, Martino M. State of the Art of Conventional Reactors for Methanol Production. : Elsevier; 2018.

[73] Pontzen F, Liebner W, Gronemann V, Rothaemel M, Ahlers B. CO2-based methanol and DME – Efficient technologies for industrial scale production. Catalysis Today 2011;171(1):242-50.

[74] Wernicke H, Plass L, Schmidt F. Methanol Generation. Methanol: The Basic Chemical and Energy Feedstock of the FutureBerlin, Heidelberg: Springer Berlin Heidelberg; 2014, p. 51-301.

[75] Phongprueksathat N, Urakawa A. Heterogeneously Catalyzed CO 2 Hydrogenation to Alcohols. CO2 Hydrogenation CatalysisWeinheim, Germany: WILEY-VCH GmbH; 2021, p. 207-236.

[76] Ma L, Tran T, Wainwright MS. Methanol synthesis from CO 2 using skeletal copper catalysts containing co-precipitated Cr 2 O 3 and ZnO.

[77] TRIEBSKORN; BRUNO, ZIRKER; GUENTER, GRUENDLER; KARL-HEINZ, SCHWARZMANN; MATTHIAS, BROECKER; FRANZ J, MAROSI; LASZLO, inventors. AnonymousPreparation of methanol synthesis catalyst comprising zinc, copper and aluminum. US4436833A. 1984 Mar 13,.

[78] Topsoe. Topsoe. 2022; Available at: https://www.topsoe.com/products/catalysts/mk-121.

[79] Cui X, Kær SK, Nielsen MP. Energy analysis and surrogate modeling for the green methanol production under dynamic operating conditions. Fuel (Guildford) 2022 Jan 01,;307:121924.

[80] Dale E. Seborg. Process dynamics and control. 4th ed ed. : Wiley; 2017.

[81] Aström KJ, Murray RM. Feedback Systems. Princeton, NJ, USA: Princeton University Press; 2010.

[82] Desborough, Biomedical, Desborough, Miller. Increasing Customer Value of Industrial Control Performance Monitoring - Honeywell's Experience Increasing Customer Value of Industrial Control Performance Monitoring-Honeywell's Experience. 2016;.

[83] Luyben WL. Plantwide Dynamic Simulators in Chemical Processing and Control. : CRC Press; 2002.

[84] Luyben WL. Control of Tubular Reactor Systems. Chemical Reactor Design and ControlHoboken, NJ, USA: John Wiley & Sons; 2007, p. 1.

[85] Luyben WL. Converting from Steady-State to Dynamic Simulation. Distillation Design and Control Using Aspen™ Simulation. 2nd Edition ed. Hoboken, New Jersey: John Wiley & Sons; 2013, p. 1-2.

[86] Luyben WL. Distillation Turndown. Distillation Design and Control Using Aspen™ Simulation. 2nd Edition ed. Hoboken, New Jersey: John Wiley & Sons; 2013, p. 1.

[87] Luyben WL, Tyréus BD, Luyben ML. Plantwide process control. New York [u.a.]: McGraw-Hill; 1999.

[88] Luyben WL. Control of More Complex Columns. Distillation Design and Control Using Aspen™ Simulation. 2nd Edition ed. Hoboken, New Jersey: John Wiley & Sons; 2013, p. 1.

[89] Luyben WL. Steady-State Calculations for Control Structure Selection. Distillation Design and Control Using Aspen™ Simulation. 2nd Edition ed. Hoboken, New Jersey: John Wiley & Sons; 2013, p. 1.

[90] Glesias Gonzµlez, Ilers, Schaub. Flexible Operation of Fixed-Bed Reactors for aC atalytic Fuel Synthesis-CO 2 Hydrogenation as Example Reaction.

[91] Chen, Yang. Power-to-methanol: The role of process flexibility in the integration of variable renewable energy into chemical production. Energy conversion and management 2021 Jan 15,;228:113673.

[92] Li B, Zhang N, Smith R. Simulation and analysis of CO2 capture process with aqueous monoethanolamine solution. Applied energy 2016 Jan 1,;161:707-17.

[93] Bussche KMV, Froment GF. A steady-state kinetic model for methanol synthesis and the water gas shift reaction on a commercial Cu/ZnO/Al2O3 catalyst. Journal of catalysis 1996;161(1):1-10.

[94] Abrol, Hilton. Modeling, simulation and advanced control of methanol production from variable synthesis gas feed. Computers & chemical engineering 2012 May 11,;40:117-31.

[95] National Energy Technology Laboratory. Commercial-Scale Demonstration of the Liquid Phase methanol (LPMEOH) Process A DOE Assessment. 2003;.

[96] Harri Nieminen, LUT university. Methanol synthesis Aspen plus model. Unpublised;.

[97] Luyben WL. Chemical Process Engineering Principles of Combustion Turbines. Energy & fuels 2013 Oct 17,;27(10):6316-21.

[98] Bussche KMV, Froment GF. A Steady-State Kinetic Model for Methanol Synthesis and the Water Gas Shift Reaction on a Commercial Cu/ZnO/Al2O3Catalyst. Journal of Catalysis 1996;161(1):1-10.

[99] Mignard D, Pritchard C. On the use of electrolytic hydrogen from variable renewable energies for the enhanced conversion of biomass to fuels. Chem.Eng.Res.Design 2008;86(5):473-87.

[100] Chen, Jiang, Song, Posarac. Optimization of Methanol Yield from a Lurgi Reactor. Chemical engineering & technology 2011 May;34(5):817-22.

[101] Sakas G, Ibáñez-Rioja A, Ruuskanen V, Kosonen A, Ahola J, Bergmann O. Dynamic energy and mass balance model for an industrial alkaline water electrolyzer plant process. Int J Hydrogen Energy 2022;47(7):4328-45.

Appendix 1: Equipment sizing

Table A-I. Equipment sizing of FLASH-1 and FLASH-2 in Figure 31.

Parameters	FLASH-1	FLASH-2
Vapor density ρ_g, kg m^{-3} (from Aspen plus)	15.18	2.03
Maximum vapor velocity V_{max}, m s-1	0.16	0.43
Volumetric flow rate of vapor V_g, m^3 s^{-1} (from Aspen plus)	0.28	0.02
Diameter based on vapor phase D_g, m	1.51	0.26
Height H$_g$, m	3.02	0.53
Volumetric flow rate of liquid V_l, m^3 s^{-1} (from Aspen plus)	0.002	0.0019
Diameter based on liquid phase D_l, m	0.92	0.91
Height H$_l$, m	1.84	1.82

Appendix 2: Matlab code

Matlab code, which was used to transform the mass of solar-based electrolytic H$_2$ to molar flow rate at suitable scale (292.5 kmol h^{-1} at full-load mode) for the thesis, are shown below:

```
load('data.mat');
H2 = data.H2Prod; %kg
t = (0:5:527039)'; % minutes
H2_transform = H2/max(H2) * 292.5; %kmol/h
% plotting modified H2 production by alkaline electrolyzer around 1 year
Plot (t, H2_transform,'.')
xlabel ('Time, min')
ylabel ('Molar flow rate of H2, kmol/h')
set (gca,'Xtick',0:1e5:5.3e5)
```

Appendix 3: Streams tables

Table A-II. Stream table (1/3) of methanol synthesis process (full-load mode)

	CO2	CO2-1	CO2-2	F-1	F-2	F-3	H2	H2-1	H2-2	P-1
Temperature, ℃	20.00	19.44	189.96	88.12	225.00	225.00	20.00	20.02	99.77	256.92
Pressure, bar	1.00	0.50	60.00	60.00	58.80	58.80	30.00	29.50	60.00	55.80
Mole Flows, kmol/h	97.50	97.50	97.50	2486.10	2486.10	2485.97	292.50	292.50	292.50	2305.42
CO_2, mol %	1.00	1.00	1.00	0.13	0.13	0.13	0.00	0.00	0.00	0.10
CO mol %	0.00	0.00	0.00	0.03	0.03	0.03	0.00	0.00	0.00	0.03
Methanol, mol %	0.00	0.00	0.00	0.00	0.00	0.00	0.00	0.00	0.00	0.04
H_2, mol %	0.00	0.00	0.00	0.84	0.84	0.84	1.00	1.00	1.00	0.79
H_2O, mol %	0.00	0.00	0.00	0.00	0.00	0.00	0.00	0.00	0.00	0.04
Mass Flows, kg/h	4290.96	4290.96	4290.96	20286.59	20286.59	20287.36	589.64	589.64	589.64	20287.36

Table A-III. Stream table (2/3) of methanol synthesis process (full-load mode)

	P-2	P-2-3	P-3	P-4	P-5	P-6	P-6-1	PURG1-1	PURG2-1	PURGE-1
Temperature, ℃	118.90	109.47	35.00	35.00	36.55	23.57	31.99	34.97	23.71	35.00
Pressure, bar	54.60	53.40	53.40	53.40	2.00	2.00	1.50	52.90	1.50	53.40
Mole Flows, kmol/h	2305.42	2305.42	2305.53	188.28	188.28	181.69	181.69	21.17	6.59	21.17
CO_2, mol %	0.10	0.10	0.10	0.02	0.02	0.00	0.00	0.11	0.52	0.11
CO mol %	0.03	0.03	0.03	0.00	0.00	0.00	0.00	0.03	0.02	0.03
Methanol, mol %	0.04	0.04	0.04	0.48	0.48	0.49	0.49	0.00	0.04	0.00
H_2, mol %	0.79	0.79	0.79	0.01	0.01	0.00	0.00	0.86	0.41	0.86
H_2O, mol %	0.04	0.04	0.04	0.48	0.48	0.50	0.50	0.00	0.01	0.00
Mass Flows, kg/h	20287.36	20287.36	20286.65	4724.98	4724.98	4554.79	4554.79	155.62	170.19	155.62

Table A-IV. Stream table (3/3) of methanol synthesis process (full-load mode)

	PURGE-2	REC-1	REC-2	REC-2-1	REC-3	REC-4
Temperature, ℃	23.57	35.00	35.00	34.97	50.09	80.00
Pressure, bar	2.00	53.40	53.40	52.90	61.20	60.00
Mole Flows, kmol/h	6.59	2117.26	2096.08	2096.08	2096.08	2096.08
CO_2, mol %	0.52	0.11	0.11	0.11	0.11	0.11
CO mol %	0.02	0.03	0.03	0.03	0.03	0.03
Methanol, mol %	0.04	0.00	0.00	0.00	0.00	0.00
H_2, mol %	0.41	0.86	0.86	0.86	0.86	0.86
H_2O, mol %	0.01	0.00	0.00	0.00	0.00	0.00
Mass Flows, kg/h	170.19	15561.67	15406.05	15406.05	15406.05	15406.05